JSCSEN 73(1)1–129(2008)

UDC 54:66

ISSN 0352–5139

# Journal of the Serbian Chemical Society

Electronic Version

VOLUME 73

NO 1

BELGRADE 2008

Available on line at

www.shd.org.yu/JSCS/

The full search of JSCS is available through

DOAJ DIRECTORY OF OPEN ACCESS JOURNALS

www.doaj.org

Journal of the Serbian Chemical Society
JSCS@tmf.bg.ac.yu • www.shd.org.yu/JSCS
ISSN 0352–5139
*J. Serb. Chem. Soc.* Vol. 73, No. 1 (2008)

CONTENTS



Published by the Serbian Chemical Society
Karnegijeva 4/III, 11120 Belgrade, Serbia
Printed by the Faculty of Technology and Metallurgy
Karnegijeva 4, P.O. Box 35-03, 11120 Belgrade, Serbia

Journal of the Serbian Chemical Society
JSCS@tmf.bg.ac.yu • www.shd.org.yu/JSCS
*J. Serb. Chem. Soc.* *73* (1) 1–6 (2008) UDC 547.979.732+542.9+547.571+547.551:547.538:537.872
*JSCS–3682* *Original scientific paper*

# Synthesis and characterization of novel porphyrin Schiff bases

LEI WANG, YAQING FENG*, JINQIANG XUE and YUKUN LI

*School of Chemical Engineering and Technology, Tianjin University, Tianjin 300072, China*

(Received 14 June 2007, revised 9 August 2007)

*Abstract*: Novel porphyrin Schiff bases were synthesized by a simple Schiff base condensation in refluxing toluene between 5-(4-aminophenyl)-10,15,20-triphenylporphyrin (ATTP) **3** and styryl aldehydes **4**–**6** or *p*-halobenzaldehydes **7**–**9**. The newly synthesized porphyrin Schiff bases were characterized on the basis of their chemical properties and spectral data. A good intramolecular energy transfer from the styryl unit to the porphyrin moiety was found.

*Keywords*: porphyrin Schiff base; styryl; energy transfer.

## INTRODUCTION

Recently investigation of porphyrin has been of increasing interest.[1,2] In particular, focus was directed to the synthesis and study of well-designed porphyrin derivatives which could act as molecular switches,[3] as well as materials for non-linear optics[4] and solar cells.[5] In these fields, investigation of photo-induced electron and energy transfer of unsymmetrical porphyrin are essential for understanding the mechanism and evaluating the progress. Therefore, unsymmetrical porphyrin, especially tetraphenyl porphyrin derivatives substituted with an expanded π conjugated system at the meso-position, are of potential interest. There are a few reports about porphyrin Schiff bases, which are ligands produced by the reaction of porphyrin and aldehydes.[6,7] In the present study, a novel series of porphyrin Schiff bases was synthesized by a simple Schiff base condensation in refluxing toluene between 5-(4-aminophenyl)-10,15,20-triphenylporphyrin (ATTP) **3** and styryl aldehydes **4**–**6** or *p*-halobenzaldehydes. **7**–**9**. The styryl group was firstly used to expand the π system of porphyrin macrocycle at one of the *meso*-phenyl groups.

## RESULTS AND DISCUSSION

### *Chemistry*

The synthesis of porphyrin Schiff bases was performed following the steps shown in Scheme 1. Synthesis of all the new compounds **10**–**15** was accomplished, in moderate to good yields, by a simple Schiff base condensation in re-

* Corresponding author. E-mail: yqfeng@tju.edu.cn
doi: 10.2298/JSC0801001W

fluxing toluene between 5-(4-aminophenyl)-10,15,20-triphenylporphyrin (ATTP) **3** and styryl aldehydes **4**–**6** or *p*-halobenzaldehydes **7**–**9**. Spectral data (IR, $^1$H-NMR and MS) of all the newly synthesized compounds were in full agreement with the proposed structures. The reactions of ATTP with *p*-halobenzaldehydes **7**–**9** were easier than with those with aldehydes **4**–**6** due to the higher activities of the aldehyde group of the *p*-halobenzaldehydes **7**–**9** compared to those of aldehydes **4**–**6**. The styryl group is an electron donating group, hence the activities of the styryl aldehydes were lower and the Schiff base condensation reactions required a longer time. In this study, refluxing in various solvents, such as THF, $CHCl_3$, *etc*., resulted in the formation of the required products but the reactions did not go to completion even in the presence of excess aldehyde. Besides the solvent effect, higher reaction temperatures were beneficial for the condensation. The separation and purification of porphyrin usually requires column chromatography. Thus purification of the porphyrin Schiff bases **10**–**15** by silica gel column chromatography, using a mixture of $CH_2Cl_2$ and light petroleum as the eluent, was attempted. However, the compounds eluting from the column were found to be partly degraded. Hence, the products were recrystallized to remove the excess aldehydes.

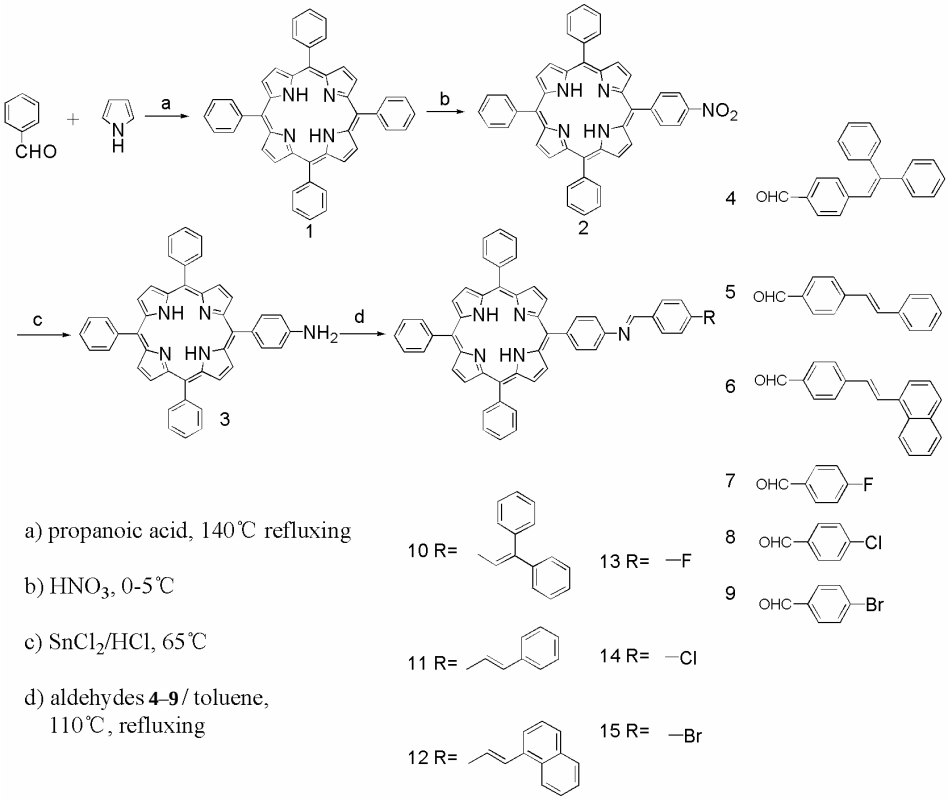


Scheme 1.

*Spectral analysis*

*$^1$H-NMR spectroscopy.* The $^1$H-NMR spectra confirmed the structures of all the compounds **10**–**15**. The chemical shifts of the characteristic internal NH of the porphyrin macrocycle was found from −2.67 to −2.77 ppm. In all porphyrin Schiff bases, the eight protons of *β*-pyrrole separated into two groups, which indicated the two *β*-pyrrolic protons near C=N groups were in a different chemical environment to the other six. The unsymmetrical chemical environment of these protons showed the influence of the expanded π structure or the strong electron withdrawing effect of the halogen atom. A single peak in the range 8.62–8.63 ppm, indicated the proton of the CH=N group. The chemical shift of the proton (protons) of the C=C group (not in phenyl) at 9.90 ppm in compound **10** and 8.07 ppm in compounds **11** and **1** were also evidence of the formation of the porphyrin Schiff bases.

*IR spectroscopy*. The infrared absorption spectra of all the porphyrin Schiff bases presented the stretching of the C=N bond at about 1580–1590 cm$^{-1}$. In the spectra of the porphyrin Schiff bases **13**–**15**, the presence of the C–X (X = F, Cl, Br) bond on the phenyl ring led to the appearance of a strong absorption band at 1000–1100 cm$^{-1}$.

*UV–Vis spectroscopy*. All the porphyrin Schiff bases **10**–**15** exhibited characteristically one Soret band and four weak Q bands. Compared to ATTP (416 nm), the Soret bands of the new compounds were slightly red shifted (by about 6 nm), which indicated that the introduction of the new groups to the *meso*-phenyl of the porphyrin moiety did not greatly change the energy of $S_1$. The absorptions of the porphyrin Schiff bases **10**–**12**, shown in Fig. 1, indicate that each had a new weak and broad band at about 370 nm, which was slightly red shifted compared to the maximum absorption of the corresponding styryl group, due to the styryl–aryl group π→π* region. Compound **10** had an obvious "split Soret" structure, indicating the interaction between the styryl group and the porphyrin moiety.

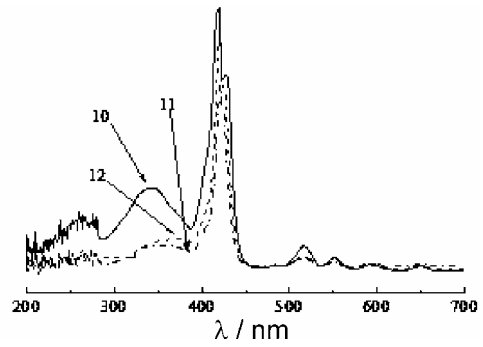


Fig. 1 The UV–Vis spectra of the porphyrin Schiff bases **10**–**12** in toluene ($5\times10^{-6}$ M).

*Fluorescence spectroscopy.* The fluorescence emission spectra of the porphyrin Schiff bases excited at their Soret bands are shown in Fig. 2. For compounds **13**–**15**, the fluorescence was not quenched. There are two possible reasons

for this, either no substantial amount of electron transfer from porphyrin moiety to halogenated phenyl ring occurred or the rate of the back transfer of the electron was much faster than the rate of electron separation.

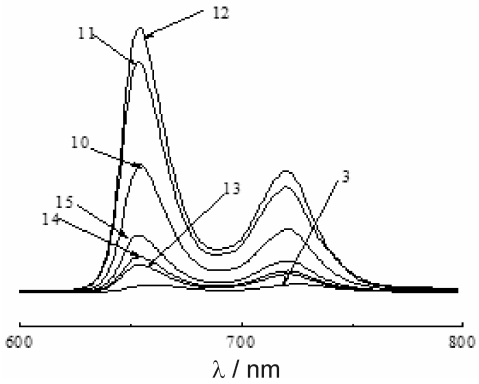


Fig. 2 The fluorescence emission spectra of the porphyrin Schiff bases **10**–**15** in toluene ($5\times10^{-6}$ M), excited at their Soret bands.

Direct excitation of compounds **10**–**15** (Soret bands) in degassed toluene gave strong fluorescence bands at about 650 and 730 nm due to the porphyrin units. Excitation of compounds **10**–**15** at the maximum absorption of the styryl aldehydes **4**–**6** (376–392 nm) resulted in the same fluorescence patterns as direct excitation (Fig. 3), while no emissions of the styryl aldehydes at 430–450 nm were observed. There is apparently good energy transfer between the styryl unit and the porphyrin moiety through the C=N bond.

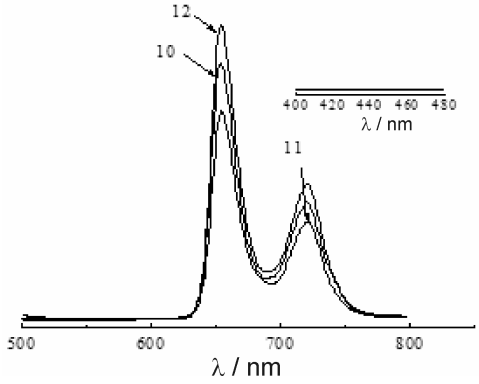


Fig. 3 The fluorescence emission spectra of porphyrin Schiff bases **10–12** in toluene ($5\times10^{-6}$ M), excited at the maxima of the styryl groups (at 392 nm for **10**, at 376 nm for **11** and at 380 nm for **12**).

## EXPERIMENTAL

*General synthesis procedure*

All reagents are commercially available. The toluene was refluxed with Na. The $CH_2Cl_2$ was washed with a saturated solution of $Na_2CO_3$ and distilled. All other reagents were used without further purification.

5-(4-Nitrophenyl)-10,15,20-triphenylporphyrin (NTTP) **2** was obtained by the regioselective nitration of 5,10,15,20-tetraphenylporhyrin **1**. Then the NTTP **2** was reduced with $SnCl_2$/HCl according to a literature procedure[8] to obtain ATTP **3**. The porphyrin Schiff bases **10**–**15** were synthesized as follows: ATTP **3** (0.1 mmol, 63 mg) and the required aldehyde (0.2 mmol, 56.8 mg

of **4**, 41.2 mg of **5**, 43.2 mg of **6**, 24 mg of **7**, 28 mg of **8**, 36.3 mg of **9**) were dissolved in 100 ml of dry toluene containing 4 Å molecular sieves. The resulting solution was refluxed until the disappearance of the ATTP **3,** monitored by TLC (18 h for **4**, 18 h for **5**, 15 h for **6**, 2 h for **7**, 6 h for **8**, 12 h for **9**). The solvent was removed under reduced pressure and the crude product was dissolved in $CH_2Cl_2$ and filtered. Evaporation of the solvent gave purple solids. All the products were recrystallized from $CH_2Cl_2$ and light petroleum.

*Characterization*

The melting points (uncorrected) were measured on a Yanagimoto MP-500 apparatus. The FT-IR spectra (KBr pellets) were measured on a Bio-Rad FTS3000 infrared spectrometer. The $^1$H-NMR spectra were recorded on a Varian INOVA-500 Hz spectrometer at 298 K in $CDCl_3$. The mass spectra were obtained using a LCQ Advantage MAX spectrometer. The UV–Vis spectra were measured on a Therma Helios Gamma spectrometer. The fluorescence spectra were obtained using a Varian Cary Eclipse spectrometer.

*Porphyrin Schiff base* **10**: Yield: 70 %; purple solid; m.p. >300 °C; $^1$H-NMR (500 MHz, $CDCl_3$, $\delta$, ppm): −2.77 (*s*, 2H, internal NH), 7.01 (*s*, 1H, terminal phenyl), 7.08 (*s*, 1H, terminal phenyl), 7.15–7.21 (*m*, 8H, terminal phenyl), 7.59 (*d*, 2H, N=C–phenyl, $J$ = 8.0 Hz), 7.64 (*d*, 2H, N=C–phenyl, $J$ = 8.0 Hz), 7.72–7.79 (*m*, 9H, *m,p*-triphenyl), 7.84(*d*, 2H, C=N–phenyl, $J$ = 8.5 Hz), 8.22–8.24 (*m*, 8H, *o*-tetraphenyl), 8.74 (*s*, 1H, –N=CH–), 8.85–8.87 (*m*, 6H, *β*-pyrrolic), 8.90 (*d*, 2H, *β*-pyrrolic, $J$ = 5.0 Hz), 9.90 (*s*, 1H, –C=CH–); MS (*m/z*): 896 (M + + H)$^+$; IR (KBr, cm$^{-1}$): 1597 (stretching of C=N); UV–Vis $\lambda_{max}$ (in toluene, nm): 342, 420 (Q band), 516, 551, 594, 645 (four Soret bands).

*Porphyrin Schiff base* **11**: purple solid; Yield: 68 %; m.p. >300 °C; $^1$H-NMR (500 MHz, $CDCl_3$, $\delta$, ppm): –2.74 (*s*, 2H, internal NH), 7.23 (*s*, 1H, terminal phenyl), 7.28 (*s*, 1H, terminal phenyl), 7.33 (*t*, 1H, terminal phenyl, $J$ = 7.5 Hz), 7.42 (*t*, 2H, terminal phenyl, $J$ = = 7.5 Hz), 7.60 (*d*, 2H, N=C–phenyl, $J$ = 7.5 Hz), 7.64 (*d*, 2H, N=C–phenyl, $J$ = 8.5 Hz), 7.71 (*d*, 2H, C=N–phenyl, $J$ = 8.5 Hz), 7.75–7.82 (*m*, 9H, *m,p*-triphenyl), 8.07 (*d*, 2H, –CH=CH–, $J$ = 8.5 Hz), 8.23–8.26 (*m*, 8H, *o*-tetraphenyl), 8.83 (*s*, 1H, –N=CH–), 8.87–8.89 (*m*, 6H, *β*-pyrrolic), 8.94 (*d*, 2H, *β*-pyrrolic, $J$ = 4.5 Hz); MS (*m/z*): 820 (M + H)$^+$; IR (KBr, cm$^{-1}$): 1595 (stretching of C=N); UV–Vis $\lambda_{max}$ (in toluene, nm): 350, 421 (Q band), 517, 552, 595, 649 (four Soret bands).

*Porphyrin Schiff base* **12**: purple solid; Yield: 80 %; m.p. >300 °C; $^1$H-NMR (500 MHz, $CDCl_3$, $\delta$, ppm): –2.74 (*s*, 2H, internal NH), 7.23 (*t*, 2H, naphthyl), 7.49–7.54 (*m*, 2H, N=C– –phenyl), 7.57 (*t*, 1H, naphthyl, $J$ = 7.0 Hz), 7.62 (*d*, 2H, N=C–phenyl, $J$ = 8.0 Hz), 7.72–7.77 (*m*, 9H, *m,p*-triphenyl), 7.80 (*d*, 2H, naphthyl, $J$ = 7.0 Hz), 7.82 (*d*, 2H, C=N–phenyl, $J$ = 8.0 Hz), 7.88 (*d*, 1H, $J$ = 8.0 Hz, naphthyl), 8.02(*s*, 1H, naphthyl), 8.06 (*d*, 2H, –CH=CH–, $J$ = 8.5 Hz), 8.21–8.27 (*m*, 8H, *o*-tetraphenyl), 8.83 (*s*, 1H, –N=CH–), 8.85–8.88 (*m*, 6H, *β*-pyrrolic), 8.92 (*d*, 2H, *β*-pyrrolic, $J$ = 4.5 Hz); MS (*m/z*): 870 (M + H)$^+$; IR (KBr, cm$^{-1}$): 1594 (stretching of C=N); UV–Vis $\lambda$max (in toluene, nm): 370, 421 (Q band), 516, 551, 593, 648 (four Soret bands).

*Porphyrin Schiff base* **13**: purple solid; Yield: 85 %; m.p. >300 °C; $^1$H-NMR (500 MHz, $CDCl_3$, $\delta$, ppm): –2.72 (*s*, 2H, internal NH), 7.24 (*d*, 2H, phenyl, $J$ = 8.0 Hz), 7.61 (*d*, 2H, phenyl, $J$ = 8.5 Hz), 7.75–7.80 (*m*, 9H, *m,p*-triphenyl), 8.04–8.07 (*m*, 2H, C=N–phenyl), 8.24–8.27 (*m*, 8H, *o*-tetraphenyl), 8.77 (*s*, 1H, –N=CH–), 8.88–8.90 (*m*, 6H, *β*-pyrrolic), 8.94 (*d*, 2H, *β*-pyrrolic, $J$ = 4.5 Hz); MS (*m/z*): 736 (M + H)$^+$; IR (KBr, cm$^{-1}$): 1587, 1597 (stretching of C=N); UV–Vis $\lambda_{max}$ (in toluene, nm): 421 (Q band), 516, 551, 593, 649 (four Soret bands).

*Porphyrin Schiff base* **14**: purple solid; Yield: 85 %; m.p. >300 °C; $^1$H-NMR (500 MHz, $CDCl_3$, $\delta$, ppm): –2.73 (*s*, 2H, internal NH), 7.41 (*d*, 2H, phenyl, $J$ = 8.5 Hz), 7.53 (*d*, 2H, phenyl, $J$ = 8.0 Hz), 7.69–7.74 (*m*, 9H, *m,p*-triphenyl), 7.85 (*d*, 2H, C=N–phenyl, $J$ = 8.5 Hz),

8.19–8.22 (*m*, 8H, *o*-tetraphenyl), 8.62 (*s*, 1H, –N=CH–), 8.85–8.86 (*m*, 6H, *β*-pyrrolic), 8.89 (*d*, 2H, *β*-pyrrolic, $J$ = 4.5 Hz); MS (*m/z*): 752 $(M + H)^+$; IR (KBr, $cm^{-1}$): 1590 (stretching of C=N); UV–Vis $\lambda_{max}$ (in toluene, nm): 420 (Q band), 516, 551, 593, 649 (four Soret bands).

*Porphyrin Schiff base* **15**: purple solid; Yield: 75 %; m.p. >300 °C; $^1$H-NMR (500 MHz, $CDCl_3$, $\delta$, ppm): –2.67 (*s*, 2H, internal NH), 7.60 (*d*, 2H, phenyl, $J$ = 8.0 Hz), 7.65 (*d*, 2H, phenyl, $J$ = 8.5 Hz), 7.77–7.81 (*m*, 9H, *m,p*-triphenyl), 7.86 (*d*, 2H, C=N–phenyl, $J$ = 8.5 Hz), 8.27–8.28 (*m*, 8H, *o*-tetraphenyl), 8.69 (*s*, 1H, –N=CH–), 8.91–8.92 (*m*, 6H, *β*-pyrrolic), 8.95 (*d*, 2H, *β*-pyrrolic, $J$ = 5.0 Hz); MS (*m/z*): 596 $(M + H)^+$: IR (KBr, $cm^{-1}$): 1585, 1595 (stretching of C=N); UV–Vis $\lambda_{max}$ (in toluene, nm): 421 (Q band), 516, 551, 592, 649 (four Soret bands).

## CONCLUSIONS

A series of novel porphyrin Schiff bases was synthesized and structurally characterized by FAB–MS, $^1$H-NMR and IR spectroscopy. As evidenced by the analysis of UV–Vis and fluorescence spectra, a good intra-molecular energy transfer from the styryl unit to the porphyrin moiety was found when the porphyrin Schiff bases **10**–**12** were excited at 370–390 nm.

*Acknowledgements*. The Natural Science Foundation of Tianjin (No. 07JCZDJC00300) is thanked for the support.

## И З В О Д

## СИНТЕЗА И КАРАКТЕРИЗАЦИЈА НОВИХ ПОРФИРИНСКИХ ШИФОВИХ БАЗА

LEI WANG, YAQING FENG, JINQIANG XUE и YUKUN LI

*School of Chemical Engineering and Technology, Tianjin University, Tianjin 300072, China*

Нове порфиринске Шифове базе синтетисане су једноставном кондензацијом у толуену уз рефлукс, између 5-(4-аминофенил)-10,15,20-трифенилпорфирина (АТТР) **3** и стирил-алдехида **4**–**6** или *p*-халоген-бензалдехида **7**–**9**. Новосинтетисане порфиринске Шифове базе карактерисане су на основу њихових хемијских својстава и спектралних података. Установљен је добар интрамолекулски пренос енергије са стирил јединице на порфиринski део молекула.

(Примљено 14. јуна 2007, ревидирано 9. августа 2007)

## REFERENCES

1. G. A. Bogdanovic, V. Medakovic, M. K. Milcic, S. D. Zaric, *Int. J. Mol. Sci.* **5** (2004) 174
2. P. I. Premović, I. R. Tonsa, D. M. Đorđević, M. S. Pavlović, *J. Serb. Chem. Soc.* **65** (2000) 113
3. P. A. Liddell, G. Kodis, A. L. Moore, T. A. Moore, D. Gust, *J. Am. Chem. Soc.* **124** (2002) 7668
4. S. M. Le Cours, H. W. Guan, S. G. DiMagno, C. H. Wang, M. J. Therien, *J. Am. Chem. Soc.* **118** (1996) 1497
5. S. Antohe, L. Tugulea, *Phys. Stat. Sol.(A)* **128** (1991) 253
6. P. K. Poddutoori, B. G. Maiya, *Indian J. Chem. A* **42** (2002) 2198
7. D. M. Li, Z. X. Zhao, S. Q. Liu, G. F. Liu, T. S. Shi, X. X. Liu, *Synth. Commun.* **30** (2000) 4017
8. W. J. Kruper, J. A. Chamberlin, M. Kochanny, *J. Org. Chem.* **54** (1989) 2753.

Journal of the Serbian Chemical Society
JSCS@tmf.bg.ac.yu • www.shd.org.yu/JSCS
*J. Serb. Chem. Soc.* 73 (1) 7–13 (2008) UDC 547.754+547.367+547.497:615.281/.282:615.276
*JSCS–3683* *Original scientific paper*

# Antimicrobial activity of some isatin-3--thiosemicarbazone complexes

SANDRA S. KONSTANTINOVIĆ[1]*, BLAGA C. RADOVANOVIĆ[2], SOFIJA P. SOVILJ[3#] and SVETLANA STANOJEVIĆ[4]

[1]*Faculty of Technology, Bulevar Oslobođenja 124, 16000 Leskovac,* [2]*Department of Chemistry, Faculty of Science, Višegradska 33, 18000 Niš,* [3]*Faculty of Chemistry, University of Belgrade, P.O. Box 158, 11001 Belgrade and* [4]*Health Center, Biochemistry Laboratory, Svetozara Markovića 166, 16000 Leskovac, Serbia*

(Received 26 June 2006, revised 25 September 2007)

*Abstract*: Isatin-3-thiosemicarbazone complexes with Co(II), Ni(II), Cu(II), Zn(II), Hg(II) and Pd(II) were synthesized and evaluated for their antimicrobial activity against 7 pathogenic bacteria and 4 fungi. The complexes have an enhanced activity compared to the ligand due to transition metal involved in coordination. The anti-amoebic activity *in vitro* was evaluated against the HM1:IMSS strain of *Entamoeba histolytica* and the results were compared with the standard drug, metronidazole. The preliminary test results showed that the complexes had better anti-amoebic activity than their respective ligands. Moreover, the complexes showed better inhibition of the test organism.

*Keywords*: isatin-3-thiosemicarbazone complex; antibacterial activity; antifungal activity; anti-inflammatory activity; anti-amoebic activity.

## INTRODUCTION

Thiosemicarbazones are of considerable interest because of their chemistry and potentially beneficial biological activities, such as antitumor, antibacterial, antiviral and antimalarial activities.[1,2] Although thiosemicarbazones as ligands and their complexes are not unknown, there is not enough data about their antibacterial, antifungal and anti-amoebic activity. In the present study, the aim was to achieve a better biological profile at lower concentrations, by preparing and evaluating isatin-3-thiosemicarbazone and the corresponding complexes with Co(II), Ni(II), Cu(II), Zn(II), Hg(II) and Pd(II).

## EXPERIMENTAL

### *Materials, methods and instruments*

All chemicals used in the present work, *viz.*, isatin, thiosemicarbazide, metal chlorides and solvents were of analytical reagent (A.R.) grade (E. Merck).

* Corresponding author. E-mail: andjelkovic_s@yahoo.com
# Serbian Chemical Society member.
doi: 10.2298/JSC0801007K

*General procedure for the preparation of isatin-3-thiosemicarbazone (ITC) and the complexes*

Isatin-3-thiosemicarbazone (ITC) was prepared using a standard method.[3] The complexes were synthesized using the direct method between the ligand and the required metal(II) chloride (2:1 for Ni(II) Co(II)) and 1:1 molar ratio for Cu(II), Zn(II), Pd(II) and Hg(II).[3] The solutions were heated under reflux for 3–5 h and the products were filtered, washed with ethanol and dried *in vacuo* over $CaCl_2$ (Fig. 1).

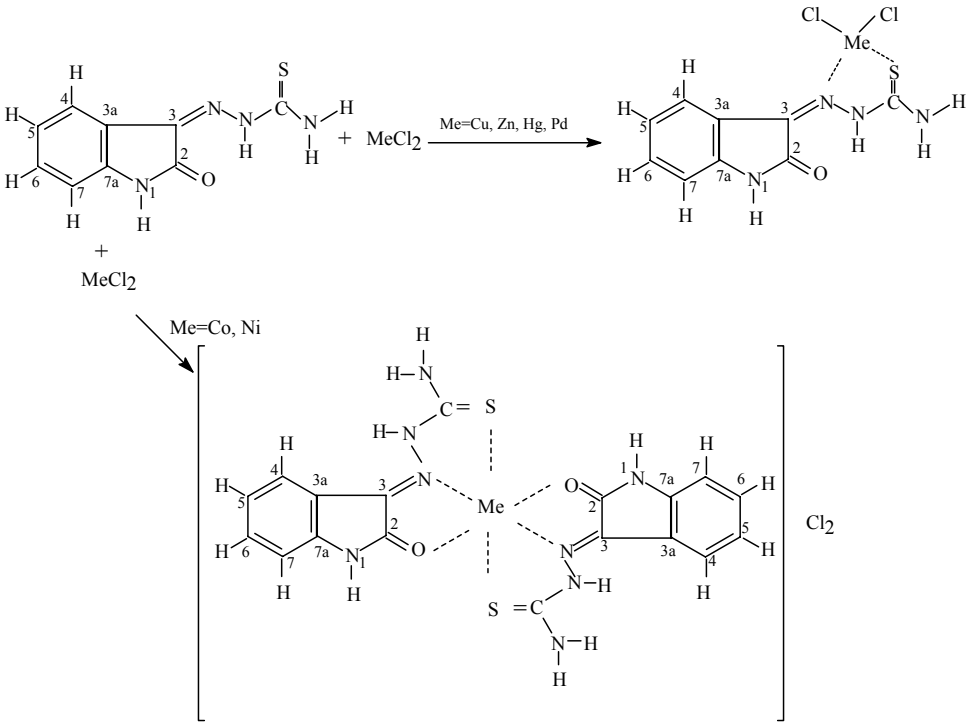


Fig. 1. Reaction scheme of the formation of the complexes.

*Analytical measurements*

Microanalysis for carbon, hydrogen and nitrogen was carried with a Carlo Erba 1106 microanalyzer. The chloride content was determined potentiometrically. The metal contents were determined using a Virial AA-457 double beam spectrometer. The FTIR spectra were recorded on a Michaelson Bomen MB-series spectrophotometer, using the KBr pellet technique (1 mg/100 mg). The electronic spectra were recorded on a Perkin/Elmer Lambda 15 UV/Vis spectrophotometer using $10^{-3}$ mol $dm^{-3}$ solutions in DMF. The $^1$H-NMR spectra were obtained in DMSO solution using a Gemini-200 "HF NMR" spectrometer. The magnetic susceptibility measurements were made at room temperature using an MSB-MKI magnetic balance (Sherwood Scientific Ltd.). The data were corrected for diamagnetism.

In vitro *antibacterial, antifungal and anti-amoebic activity*

The compounds were evaluated for their *in vitro* antibacterial activity against *Escherichia coli*, *Staphylococcus aureus*, *Enterobacter* sp., *Proteus mirabilis*, *Bacillus anthracis*, *Pseudomonas aeruginosa* and *Streptococcus faecalis*. The minimum inhibitory concentration (MIC) was assessed by the agar dilution method according to guidelines established by the NCCLS

standard M7-A5.[4] A series of different concentrations of the compounds with Mueller Hinton broth was inoculated and incubated at 37 °C for 24 h. The minimum inhibitory concentration (MIC, in μg $cm^{-3}$) was considered to be the lowest concentration, which exhibited the same turbidity as the blank tube. The compounds were evaluated for their *in vitro* antifungal activity against *Microsporum gypsum*, *Epidermophyton floccosum*, *Histoplasma capsulatum*, *Candida albicans* and *Aspergillus niger* following the guidelines in the NCCLS document M27-A using the microdilution broth method.[5] The antifungal activities of the yeast were performed in RPMI 1640 medium as outlined in the document M27-A in DMF as solvent. The chemical compounds–broth medium serial tube dilutions inoculated with each yeast were incubated at 37 °C for 48–72 h. The anti-amoebic activities of the in vitro culture against the HM1:IMSS strain of *Entamoeba histolytica* was performed by the standard method.[6-9] The *E. histolytica* strain HM1:IMSS was cultured using Diamond TYIS-33 medium.[8] All the compounds were dissolved in DMF whereby the maximum concentration of DMF did not exceed 0.1 %, at which level no inhibition of amoebae growth occurred.[9,10] All the experiments were carried out in triplicate at each concentration level and repeated twice. The optical density of the resulting solution in each well was determined at 490 nm with a microplate reader. The per cent inhibition of amoebae growth was calculated from the optical densities of the control and test wells and plotted against the logarithm of the dose of the tested drug. Linear regression analysis was used to determine the best fitting straight line, from which the $IC_{50}$ value was found.

## RESULTS AND DISCUSSION

The analytical data for the prepared ligand and complexes are given below.

*ITC.* Yield: 91.1 %; yellow crystalline; m.p. 239–241 °C. Anal. calcd.: C, 49.08; H, 3.70; N, 25.32; S 14.56. Found: C, 49.05; H, 3.75; N, 25.30; S 14.51; FTIR (KBr, $cm^{-1}$): 1710 (C=O stretching), 1585 (C=N stretching), 1250, 854 (C=S); $^1$H-NMR (200 MHz, DMSO-$d_6$, $\delta$, ppm): 6.91–7.64 (*m*, 4H, Ar), 8.69, 9.04 (*s*, 2H, $NH_2$), 11.21 (*s*, 1H, NH), 12.47 (*s*, 1H, NH); UV/Vis ($\lambda$ ($cm^{-1}$)/$\varepsilon_{max}\times10^{-3}$ ($mol^{-1}$ $dm^3$ $cm^{-1}$)): 28.6/0.946 ($\pi\rightarrow\pi^*$); 27.3/1.325 ($\pi\rightarrow\pi^*$).

*$Co(ITC)_2Cl_2$.* Yield: 54.52 %, dark red microcrystalline, m.p. 264 °C. Anal. calcd.: C, 42.30; H, 3.00; N, 21.70; Cl, 12.16; Co, 10.44. Found: C, 42.28; H, 2.95; N, 21.65; Cl, 12.12; Co, 10.45; FTIR (KBr, $cm^{-1}$): 1650 (C=O stretching), 1575 (C=N stretching), 1228, 838 (C=S). UV/Vis ($\lambda$ ($cm^{-1}$)/$\varepsilon_{max}\times10^{-3}$ ($mol^{-1}$ $dm^3$ $cm^{-1}$)): 19.5/0.817 ($^4T_{1g}(F)\rightarrow{}^4T_{1g}(P)$); 16.7/0.013 ($^4T_{1g}(F)\rightarrow{}^4A_{2g}(F)$); 14.7/0.005 ($^4T_{1g}\rightarrow{}^4A_{2g}$). $\mu_{eff}$ = 4.82 $\mu_B$.

*$Ni(ITC)_2Cl_2$.* Yield: 47.89 %, brown microcrystalline, m.p. 298 °C. Anal. calcd.: C, 38.90; H, 2.54; N, 21.80; Cl, 12.16; Ni, 10.03. Found: C, 39.01; H, 2.50; N, 21.81; Cl, 12.15; Ni, 10.06. FTIR 1659 (C=O stretching), 1554 (C=N stretching), 1227, 814 (C=S). UV/Vis ($\lambda$ ($cm^{-1}$)/$\varepsilon_{max}\times10^{-3}$ ($mol^{-1}$ $dm^3$ $cm^{-1}$)): 22.2/1.223 ($^3A_{2g}\rightarrow{}^3T_{1g}(P)$); 18.7/0.226 ($^3A_{2g}\rightarrow{}^3T_{1g}(F)$); 13.5/0.02 ($^3A_{2g}\rightarrow{}^3T_{2g}(F)$). $\mu_{eff}$ = 3.39 $\mu_B$.

*$Cu(ITC)Cl_2$.* Yield: 45.56 %, brown microcrystalline, m.p. 279 °C. Anal. calcd.: C, 36.90; H, 2.50; N, 18.50; Cl, 11.63; Cu, 19.53. Found: C, 36.87; H, 2.60; N, 18.39; Cl, 11.65; Cu, 19.56. FTIR (KBr, $cm^{-1}$): 1639 (C=O stretching); 554 (C=N stretching), 1237, 833 (C=S). UV/Vis ($\lambda$ ($cm^{-1}$)/$\varepsilon_{max}\times10^{-3}$ ($mol^{-1}$ $dm^3$ $cm^{-1}$)): 25.3/0.451 ($^2B_{1g}\rightarrow{}^2E_g$); 19.8/0.176 ($^2B_{1g}\rightarrow{}^2A_{1g}$); 13.4/0.02 ($^2B_{1g}\rightarrow{}^2B_{2g}$). $\mu_{eff}$ = 1.85 $\mu_B$.

*Zn(ITC)Cl$_2$*. Yield: 55.56 %, yellow microcrystalline, m.p. 259 °C. Anal. calcd.: C, 30.30; H, 2.65; N, 15.17; Cl, 19.12; Zn, 18.28. Found: C, 30.35; H, 2.70; N, 15.13; Cl, 19.15; Zn, 18.25. FTIR (KBr, cm$^{-1}$): 1638 (C=O stretching); 1575 (C=N stretching); 1233, 838 (C=S). $^1$H-NMR (200 MHz, DMSO-$d_6$, $\delta$, ppm): 6.91––7.64 (*m*, 4H, Ar), 8.75, 9.11 (*s*, 2H, NH$_2$), 11.28 (*s*, 1H, NH), 12.41 (*s*, 1H, NH). UV/Vis ($\lambda$ (cm$^{-1}$)/$\varepsilon_{max}\times10^{-3}$ (mol$^{-1}$ dm$^3$ cm$^{-1}$)): 18.2/0.058 (CT), 17.1/0.055 (d→d*).

*Hg(ITC)Cl$_2$*. Yield: 68.89 %, orange powder, m.p. 292 °C. Anal. calcd.: C, 22.31; H, 1.59; N, 11.09; Cl, 14.83. Found: C, 22.32; H, 1.55; N, 11.05; Cl, 14.85. FTIR (KBr, cm$^{-1}$): 1638 (C=O stretching), 1570 (C=N stretching), 1228, 838 (C=S). $^1$H-NMR (200 MHz, DMSO-$d_6$, $\delta$, ppm): 6.91–7.65 (*m*, 4H, Ar); 8.77, 9.11 (*s*, 2H, NH$_2$); 11.28 (*s*, 1H, NH); 12.41 (*s*, 1H, NH). UV/Vis ($\lambda$ (cm$^{-1}$)/$\varepsilon_{max}\times10^{-3}$ (mol$^{-1}$ dm$^3$ cm$^{-1}$)): 24.5/3.435 (CT), 17.0/0.029 (d→d*).

*Pd(ITC)Cl$_2$*. Yield: 59.69 %, orange powder, m.p. 286 °C. Anal. calcd.: C, 28.71; H, 2.09; N, 13.39; Cl, 18.54. Found: C, 28.75; H, 2.06; N, 13.35; Cl, 18.56. FTIR (KBr, cm$^{-1}$): 1705 (C=O stretching), 1575 (C=N stretching), 1231, 834 (C=S). UV/Vis ($\lambda$ (cm$^{-1}$)/$\varepsilon_{max}\times10^{-3}$ (mol$^{-1}$ dm$^3$ cm$^{-1}$)): 19.5/0.817 (CT), 16.7/0.01 (d→d*).

The complexes were evaluated for their *in vitro* antimicrobial activity against 7 pathogenic bacteria and 4 fungi. The data for metal(II) chlorides, sulfamethoxazole, trimethoprim and clotrimazole are included for comparison. All compounds have different antibacterial activity *in vitro* against the tested gram-positive and gram-negative bacteria as well as the fungi. The obtained results of the coordination compounds show enhanced activity compared to the ligand, which indicates that the coordinated metal have an influence on the anitimicrobial effects. Since all complexes are soluble in DMF, the different activities cannot be correlated with different solubility. However, the higher activity of the complexes, as compared to the free ligand, can be understood in terms of the chelation theory. This theory explains that a decrease in the polarizability of the metal could enhance the lipophilicity of the complexes.[10] The complexes with Hg(II), Pd(II) and Zn(II) were the most active against all the tested bacteria and fungi (Tables I and II).

All the complexes showed a higher activity than sulfamethoxazole, but the ligand had the same activity against *B. anthracis* and *E. coli* and less activity against *Enterobacter* sp. All the compounds showed higher activity than trimethoprim against *S. aureus*, *B. anthracis* (except the ligand) and *P. aeruginosa* and lower activity against *E. coli*. The complex with Hg(II) showed better activity than trimethoprim against *P. mirabilis* (Zn(II) and Pd(II) complexes exhibited the same activity), while against *S. faecalis*, the Hg(II) and Pd(II) complexes exhibited higher activity, while the Zn(II) complex had the same activity as trimethoprim.

The antifungal activity of the compounds was studied against four pathogenic fungi (Table II). Clortrimazole was used as the reference for inhibitory activity against fungi.

All the compounds showed a significant antifungal activity, especially the Hg(II) complex, against all the tested fungi. When compared to clotrimazole,

Pd(II) exhibited higher activity against *M. gypsum*, while Zn(II) and Ni(II) complexes were equipotent against *M. gypsum*. The complexes with Co(II), Cu(II) and Pd(II) were equipotent against *A. niger*.

TABLE I. MIC Values (μg $cm^{-3}$) of the investigated compounds against the tested bacteria

| Compound | *S. aureus* | *B. anthracis* | *Enterobacter* sp. | *E. coli* | *P. aeruginosa* | *P. mirabilis* | *S. faecalis* |
|---|---|---|---|---|---|---|---|
| ITC | 1250 | 2500 | 1250 | 1250 | 2500 | 1250 | 1250 |
| $Co(ITC)_2Cl_2$ | 78.12 | 39.06 | 312.5 | 312.5 | 156.25 | 312.5 | 156.25 |
| $Ni(ITC)_2Cl_2$ | 78.12 | 312.5 | 156.25 | 156.25 | 625 | 312.5 | 156.25 |
| $Cu(ITC)Cl_2$ | 156.25 | 156.25 | 625 | 625 | 156.25 | 312.5 | 312.5 |
| $Zn(ITC)Cl_2$ | 39.06 | 39.06 | 156.25 | 156.25 | 156.25 | 156.25 | 78.12 |
| $Hg(ITC)Cl_2$ | <5 | <5 | <5 | <5 | <5 | <5 | <5 |
| $Pd(ITC)Cl_2$ | 9.76 | 39.06 | 156.25 | 156.25 | 312.5 | 39.06 | 9.76 |
| Sulfamethoxazole | 2500 | 2500 | 625 | 1250 | >5000 | 2500 | 2500 |
| Trimethoprim | 2500 | 2500 | 156.25 | 19.53 | >5000 | 156.25 | 78.12 |
| $CoCl_2 \cdot 6H_2O$ | >5000 | >5000 | >5000 | >5000 | >5000 | >5000 | >5000 |
| $NiCl_2 \cdot 6H_2O$ | >5000 | >5000 | >5000 | >5000 | >5000 | >5000 | >5000 |
| $CuCl_2 \cdot 2H_2O$ | >5000 | >5000 | >5000 | >5000 | >5000 | >5000 | >5000 |
| $ZnCl_2$ | >5000 | >5000 | >5000 | >5000 | >5000 | >5000 | >5000 |
| $HgCl_2$ | 156.25 | 625 | 156.25 | 625 | 625 | 625 | 625 |
| $PdCl_2$ | 2500 | 5000 | 5000 | 2500 | 5000 | 2500 | 2500 |

TABLE II. MIC Values (μg $cm^{-3}$) of the investigated compounds against the tested fungi

| Compound | *M. gypsum* | *E. floccosum* | *H. capsulatum* | *C. albicans* | *A. niger* |
|---|---|---|---|---|---|
| ITC | 39.06 | 39.06 | 156.25 | 78.12 | 78.12 |
| $Co(ITC)_2Cl_2$ | 9.76 | 19.53 | 39.06 | 9.76 | 2.44 |
| $Ni(ITC)_2Cl_2$ | 4.88 | 1953 | 39.06 | 4.88 | 4.88 |
| $Cu(ITC)Cl_2$ | 39.08 | 9.76 | 78.12 | 9.76 | 2.44 |
| $Zn(ITC)Cl_2$ | 4.88 | 9.76 | 78.12 | 9.76 | 4.88 |
| $Hg(ITC)Cl_2$ | <0.3 | <0.3 | <0.3 | <0.3 | <0.3 |
| $Pd(ITC)Cl_2$ | 2.44 | 4.88 | 78.12 | 2.44 | 2.44 |
| Clotrimazole | 4.88 | 2.44 | 19.53 | 0.3 | 2.44 |

The *in vitro* anti-amoebic activities of isatin-3-thiosemicarbazone and its complexes were tested using the HM1:IMSS strain of *E. histolytica* to ascertain the effectiveness of the metal complexes in comparison with their ligand. Metronidazole was used as the reference drug with an $IC_{50}$ 1.8 μM and the results are given in Table III.

The results were estimated as the percentage of growth inhibition compared with the inhibited controls and plotted as probate values as a function of the drug

concentration. $IC_{50}$ and 95 % confidence limits were interpolated in the corresponding dose response curve. Complexing enhances the activity of the ligand, which may be due to chelation, which reduces the polarity of the central metal atom because of partial sharing of its positive charge with the ligand. The Co(II), Zn(II) and Pd(II) complexes were more active than metronidazole with smaller $IC_{50}$ values (1.44, 0.90 and 0.70 μM, respectively). The results were statistically evaluated by analysis of the variance. The null hypothesis was tested using the *t*-test. The significance of the difference between the $IC_{50}$ values of metronidazole and the complexes with Co(II), Zn(II) and Pd(II) was evaluated by the *t*-test. The calculated *t* values were found to be higher than the table value of *t* at the 5 % level. Thus it can be concluded that the character under study was significantly influenced by the treatment. Detailed studies of the toxicity of these compounds, mechanism of action as well as *in vivo* studies are in progress.

TABLE III. *In vitro* anti-amoebic activities of isatin-3-thiosemicarbazone and its complexes against the (HM1:IMSS) strain of *E. histolytica*

| Compound | $IC_{50}$ / μM | *S.D.*[a] |
|---|---|---|
| ITC | 3.90 | 0.14 |
| $Co(ITC)_2Cl_2$ | 1.44 | 0.06 |
| $Ni(ITC)_2Cl_2$ | 2.08 | 0.06 |
| $Cu(ITC)Cl_2$ | 2.23 | 0.05 |
| $Zn(ITC)Cl_2$ | 0.90 | 0.05 |
| $Pd(ITC)Cl_2$ | 0.70 | 0.15 |
| Metronidazole | 1.80 | 0.10 |

[a]Standard deviation

*Acknowledgments.* The Ministry of Science of the Republic of Serbia supports this work.

И З В О Д

## АНТИМИКРОБНА АКТИВНОСТ НЕКИХ КОМПЛЕКСА СА ИЗАТИН-3-ТИОСЕМИКАРБАЗОНОМ

САНДРА С. КОНСТАНТИНОВИЋ[1], БЛАГА Ц. РАДОВАНОВИЋ[2], СОФИЈА П. СОВИЉ[3] и СВЕТЛАНА СТАНОЈЕВИЋ[4]

*[1]Tehnolo{ki fakultet, Univerzitet u Ni{u, Bulevar Oslobo|ewa 124, 16000 Leskovac, [2]Prirodno-matemati~ki fakultet, Odsek za hemiju, Univerzitet u Ni{u, Vi{egradska 33, 18000 Ni{, [3]Hemijski fakultet, Univerzitet u Beogradu, p. pr. 158, 11001 Beograd i [4]Dom zdravqa, Biohemijska laboratorija, Svetozara Markovi}a 166, 16000 Leskovac*

Синтетисана су координациона једињења Co(II), Ni(II), Cu(II), Zn(II), Hg(II) и Pd(II) са изатин-3-тиосемикарбазоном и испитивана је њихова антимикробна активност у односу на 7 патогених бактерија и 4 гљиве. Такође, *in vitro* је испитана активност једињења у односу на HM1:IMSS сој *Entamoeba histolytica*. Резултати показују да комплекси поседују бољу активност у односу на лиганд у свим изведеним тестовима.

(Примљено 26. јуна 2006, ревидирано 25. септембра 2007)

## REFERENCES


1. J. F. M. da Silva, S. J. Garden, A. C. Pinto, *J. Braz. Chem. Soc*. **12** (2001) 273
2. E. M. Jouad, G. Larcher. M. Allain. A. Riou, G. M. Bouet, M. A. Khan, X. Do Thanh, *J. Inorg. Biochem.* **86** (2001) 565
3. S. S. Konstantinović, B. C. Radovanović, A. Krklješ, *J. Therm. Anal. Calorim.* **90** (2007) 525
4. *NCCLS Approval Standard Document M7-A5*, National Committee for Clinical Laboratory Standards, Villanova, Pa, USA, 2000
5. *Reference method for broth dilution antifungal susceptibility testing for yeasts; approved standard Document M27-A*, National Committee for Clinical Laboratory Standards, Villanova, PA, USA, **17** (1997) 1–29
6. C. W. Wright, M. J. O'Neill, J. D. Phillipson, D. C. Warhurst, *Antimicrob. Agents Chemother*. **32** (1988) 1725
7. L. S. Diamond, C. G. Clark, C. C. Cunnick, *J Eukaryot. Microbiol*. **42** (1995) 277
8. F. D. Gillin, D. S. Reiner, M. Suffness, *Antimicrob. Agents Chemother*. **22** (1982) 342
9. A. T. Keen, A. Harris, J. D. Phillipson, D. C. Warhurst, *Planta Med*. **33** (1986) 278
10. S. O. Podunavac–Kuzmanović, V. M. Leovac, N. U. Perišić–Janjić, J. Rogan, G. Balaš, *J. Serb*. *Chem. Soc.* **64** (1999) 381.

Journal of the Serbian Chemical Society
JSCS@tmf.bg.ac.yu • www.shd.org.yu/JSCS
*J. Serb. Chem. Soc.* *73* (1) 15–27 (2008) UDC 547.912+535–31+547.216+544.35:66.022.362
*JSCS–3684* *Original scientific paper*

# Stability of carotenoids toward UV-irradiation in hexane solution

DRAGAN CVETKOVIĆ and DEJAN MARKOVIĆ*

*Faculty of Technology, University of Niš, Bulevar oslobodjenja 124, 16000 Leskovac, Serbia*

(Received 12 January 2007, revised 8 August 2007)

*Abstract*: The stabilities of four selected carotenoids dissolved in hexane, two carotenes and two xanthophylls, toward UV-irradiation of three different ranges (UV-A, UV-B and UV-C) were studied in this work. The carotenoids underwent bleaching *via* a probable free radical mediated mechanism following first-order kinetics. The bleaching rates were highly dependent on the input of the involved photons and, although not consistently, on the chemical structures of the investigated compounds. For the two xanthophylls, a possible role of oxygen associated with their bleaching cannot be neglected.

*Keywords*: carotenoids; UV-irradiation; free radicals; bleaching; kinetics.

## INTRODUCTION

Depletion of the stratospheric ozone has led to an increase of biologically damaging UV-light at ambient levels (mainly UV-B light, 280–320 nm). The induced consequences affect many crucial biologically important processes of global importance, such as DNA replication,[1,2] photosynthesis,[3,4] *etc*.

Although UV-light can generally influence the whole human immune system,[5,6] it has been especially recognized as one of the major agents leading to melanoma skin cancer,[7] playing a triggering role in the initiation of very complex process leading finally to cancer.[8] Many cosmetics and pharmaceutical formulations have recently been employed for skin protection from UV-light. Some of them, in a form of a filter, employ plant protection pigments, such as flavonoids, or plant photosynthetic pigments, such as chlorophylls and carotenoids, despite the fact that their interaction with UV-light has not yet been sufficiently well elucidated at the basic level. The use of flavonoids for skin protection against UV-light is more understandable, since they are excellent UV-absorbers.[9] On the other hand, chlorophyll and carotenoids predominantly absorb in the visible region,[10] and, as is known from experiments performed *in vivo* on leaves or on isolated photosynthetic organelles, their composition is significantly altered when exposed to UV-light.[3]

* Corresponding author. E-mail: markovic57@info-net.co.yu
doi: 10.2298/JSC0801015C

Hence, to understand the basic mechanisms of interaction of photosynthetic pigments with UV-light in oil/water emulsions, a fundamental component of most pharmaceutical and cosmetics formulations[11−13] and related technologies, inherent knowledge must first be obtained in the simplest possible feasible system: in solution.

For such a purpose, the stability of four chosen carotenoids, two carotenes ($\beta$-carotene and lycopene) and two xanthophylls (lutein and neoxanthin) toward UV-irradiation of three different ranges (UV-A, UV-B and UV-C) has been studied in this work. The irradiation was performed in hexane solution for different irradiation periods, providing possibilities for kinetics analysis.

## EXPERIMENTAL

Pigments were isolated from plant material ($\beta$-carotene, lutein and neoxanthin from spinach, and lycopene from tomato fruits) purchased at the local market. All experiments and experimental procedures, beginning with extraction, were performed under dim light as much as possible and inside vessels and equipment covered with aluminum foil or black cloth, preventing possible pigment photo-oxidation.

*Pigment extraction from spinach (*Spinacia oleracea*)*

Plant pigments were extracted from spinach leaves using a modified method proposed by Swec.[14] Fresh spinach leaves free of midribs (0.030 kg) were dropped into boiling water, which was quickly replaced (after 1−2 min) with cooled water. Hot water inactivates enzymes thus preventing alteration of the pigments and permits coagulation of proteins and extracts water-soluble substances. After drying between paper towels, the leaves were separated and placed in a mixture of methanol (60 $cm^3$) and 40–75 °C petroleum ether (30 $cm^3$); the mixture was occasionally agitated over the next 30 min. Methanol removes water from the plant material and the petroleum ether extracts the pigments before they undergo secondary reactions. The deep-green extract was decanted through a cotton pad. The leaves were re-extracted twice with same quantities of methanol and 40–75 °C petroleum ether (2:1). The extracts were mixed with 120 $cm^3$ of saturated NaCl solution, whereby most of the pigments remained in the petroleum ether layer. The remaining aqueous methanol layer was re-extracted with 40 $cm^3$ of a mixture containing 40–75 °C petroleum ether and diethyl ether (1:1), ensuring solubility of the pigments in the organic phase. The successive extracts were treated by the same procedure. The final extract was a mixture of pigments and contained various forms of chlorophyll, as well as accessory pigments – carotenoids (carotenes and xanthophylls).

*Isolation of carotenoids from the spinach extract by column chromatography*

The carotenoid-fractions were isolated using a modified procedure of Swec[15] and Brockman[16] – column chromatography with silica gel (silica gel 60, Merck, 0.063–0.200 mm) as the adsorbent and a benzene/acetone mixture as the eluent. The benzene/acetone ratio was changed from initial 1:0 to final 1:1, to facilitate the elution of the polar fractions. $\beta$-Carotene appeared first (eluted by benzene only), followed by the chlorophylls (benzene:acetone, 7:1) and the xanthophylls fractions, lutein and neoxanthin, (benzene:acetone, 6:1−1:1). The fractions were dried and redissolved in hexane. Identification of the fractions was performed by comparing their Vis spectra with standards spectra.

*Pigments extraction from tomato fruits*

Ground tomato fruit (8 g) was thoroughly mixed with 40 $cm^3$ of ethanol. The slurry was stirred until the tomato paste material was no longer sticky (about 3 min). The ethanol was removed by vacuum filtration. The retained tomato residue was mixed with 60 $cm^3$ of a mixture of acetone and petroleum ether (1:1). The extract was collected by vacuum filtration and the filter residue was rewashed with the solvent mixture (20 $cm^3$) in order to improve the yield. The filtrate was transferred to a small separating funnel and mixed with 50 $cm^3$ of saturated NaCl solution. The organic layer was rewashed twice, repeatedly, first with 50 $cm^3$ of 10 % potassium carbonate and then with 50 $cm^3$ of water. Finally, approximately 1 g of anhydrous magnesium sulfate was added to dry the organic layer. After 10–15 minutes, the solution was vacuum filtered to remove the drying agent.

*Isolation of carotenoids from the tomato extract by column chromatography*

The lycopene fraction was isolated by column chromatography with alumina (aluminum oxide 90, Merck, 0.063–0.200 mm) as the adsorbent and petroleum ether/acetone mixture as the eluent. The mixture ratio was changed from the initial 10:0.1 to the final 9:1, to permit an easier elution of lycopene. $\beta$-Carotene appears first (eluted by the petroleum ether/acetone mixture of 10:0.1), followed by the lycopene fraction (eluted by the 9:1 mixture). The fractions were dried and redissolved in hexane.

*HPLC analysis of the carotenoids fractions*

HPLC analysis (Hewlet Packard) showed that there were a high percentage of carotenoids in the separated fraction. The analysis was performed under the following conditions; column: Zorbax Eclipse XDB-C18, mobile phase: acetonitrile/methanol/ethyl acetate, 60:20:20; flow rate: 0.5 ml $min^{-1}$. The monitoring wavelengths were: 445 nm for $\beta$-carotene and lycopene, 438 nm for lutein and 447 nm for neoxanthin.

*Vis spectroscopy*

The Vis spectra of the carotenoids fractions in hexane were recorded on a Varian Cary-100 Spectrophotometer. All spectra, before and after irradiation with UV-light, were recorded from 300 to 600 nm.

*UV-treatment*

Continuous irradiation of the pigments in hexane was performed in a cylindrical photochemical reactor "Rayonnet", with 14 symmetrically placed lamps with emission maxima in three different ranges: 254 nm (UV-C), 300 nm (UV-B) and 350 nm (UV-A). The samples were irradiated for different time periods in quartz cells (1 cm×1 cm×4.5 cm) placed on a rotating circular holder. The total measured energy flux was about 25 W $m^{-2}$ for 254 nm, 21 W $m^{-2}$ for 300 nm and 18 W $m^{-2}$ for 350 nm, at a distance of 10 cm from the lamps, corresponding to light intensity values of 26.6, 26.3 and 26.4 μmol $m^{-2}$ $s^{-1}$, respectively (the emission spectra of the employed lamps are given in the supplement). These very similar values were obtained from the calculated, approximately the same number of absorbed photons (belonging to the three UV-ranges), ensuring that changes in the carotenoids concentrations, if found to be caused by the UV-irradiation, were primarily related to the energy of the photons. The concentrations of $\beta$-carotene, lutein, neoxanthin and lycopene were adjusted to be about $1.3\times10^{-6}$ mol $dm^{-3}$, by using the following molar extinction coefficient ($\varepsilon$) values: $1.39\times10^5$ $dm^3$ $mol^{-1}$ $cm^{-1}$ for $\beta$-carotene in hexane at 453 nm, $1.72\times10^5$ $dm^3$ $mol^{-1}$ $cm^{-1}$ for lycopene in hexane at 503 nm, $1.41\times10^5$ $dm^3$ $mol^{-1}$ $cm^{-1}$ for lutein in diethyl ether at 445 nm and $1.36\times10^5$ $dm^3$ $mol^{-1}$ $cm^{-1}$ for neoxanthin in ethanol at 438 nm.[17-19]

RESULTS

The structures of the carotenes, $\beta$-carotene and lycopene, changed during a continuous prolonged irradiation with UV-A light (350 nm) as evidenced by the changes in their absorption spectra in hexane. Kinetic log absorbance plots as a function of irradiation time with UV-A light are shown in Figs. 1 and 2, for $\beta$-carotene and lycopene, respectively. The pigments absorption spectra showed similar behavior during irradiation with UV-B and UV-C light (not shown). Their kinetic log plots were of a very similar shape to those presented. The plots are linear with average $R$ values of about 0.98. The photolysis kinetics seem to obey a first-order law, $y = kx + n$ where $y$ is the log absorbance (the pigment absorption in hexane at 448 nm for $\beta$-carotene and 470 nm for lycopene, $x$ is the UV-irradiation time and $k$ is the rate constant for pigments bleaching).

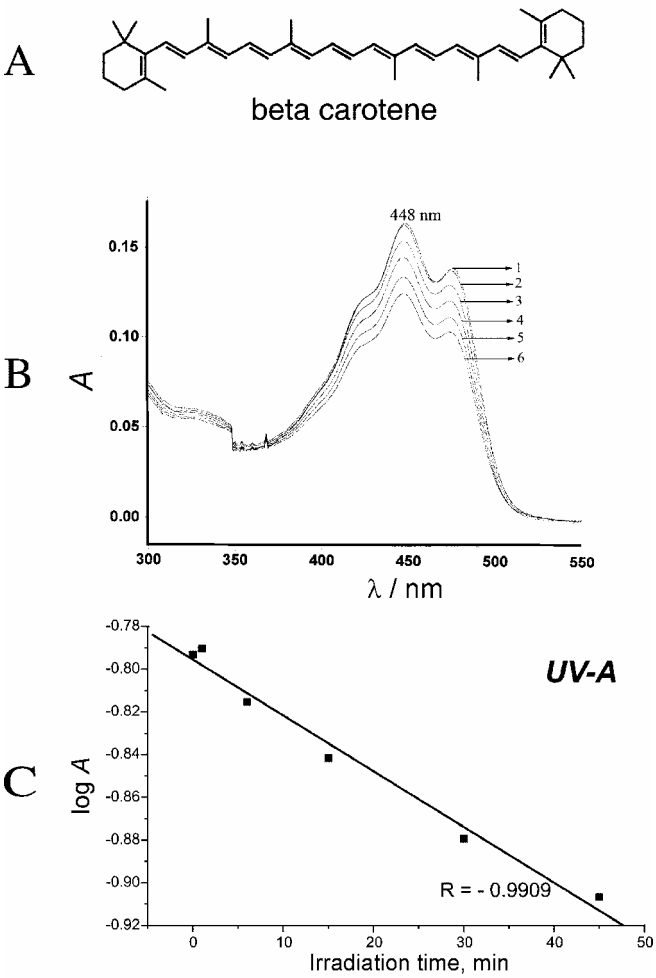


Fig 1. (A) Structure of $\beta$-carotene; (B) changes in the absorption spectra of $\beta$-carotene exposed to UV-A radiation (350 nm) in hexane. The exposure time periods were: (1) 0 min; (2) 1 min (3) 6 min; (4) 15 min; (5) 30 min; (6) 45 min. The approximate concentration of $\beta$-carotene was $1.3\times10^{-6}$ mol dm$^{-3}$; (C) the kinetic log absorbance plot of the bleaching of $\beta$-carotene in hexane against the time of UV-A irradiation. The absorbance of $\beta$-carotene was followed at 448 nm.

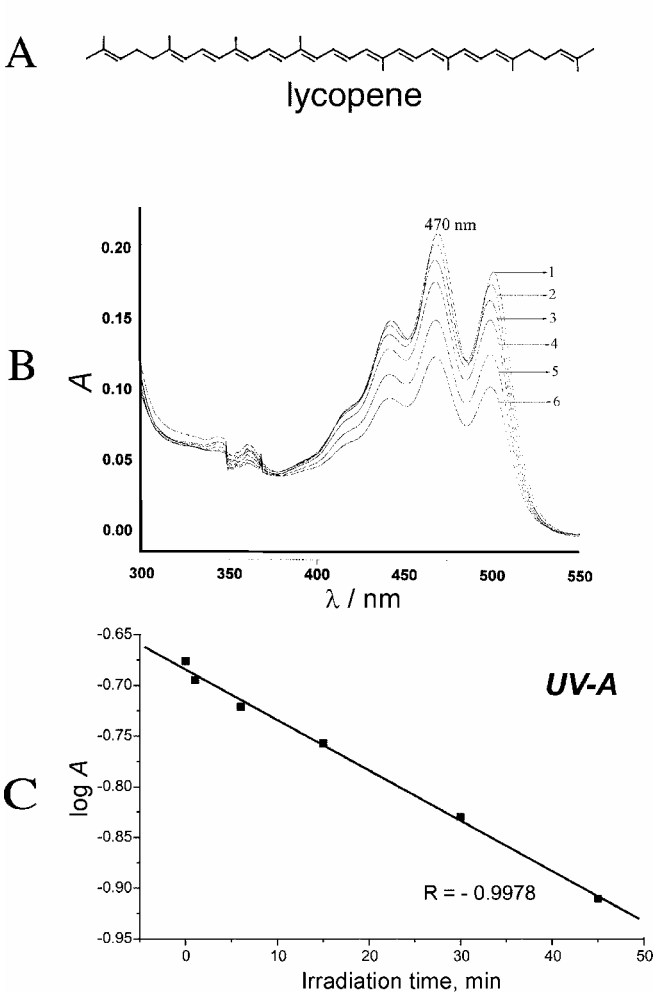


Fig. 2. (A) Structure of lycopene; (B) changes in the absorption spectra of lycopene exposed to UV-A radiation (350 nm) in hexane. The exposure time periods were: (1) 0 min; (2) 1 min; (3) 6 min; (4) 15 min; (5) 30 min; (6) 45 min. The approximate concentration of lycopene was $1.3\times10^{-6}$ mol dm$^{-3}$; (C) the kinetic log absorbance plot of the bleaching of lycopene in hexane against the time of UV-A irradiation. The absorbance of lycopene was followed at 470 nm.

The structures of the xanthophylls (lutein and neoxanthin) also changed during continuous prolonged irradiation with UV-B light (300 nm). The kinetic log absorbance as a function of irradiation time with UV-B light plots are shown in Figs. 3 and 4 for lutein and neoxanthin, respectively. The changes in the absorption spectra of lutein in hexane after a continuous prolonged irradiation with UV-C light (254 nm) and the kinetic log absorbance *vs*. irradiation time with UV-C light plot are shown in Fig. 5. The pigments absorption spectra show very similar responses during the same time regime of irradiation with UV-A light (lutein and neoxanthin) and UV-C light (neoxanthin (not shown)). The not-presented absorption spectra of all the pigments for all three irradiation regimes are given in the supplementary material. The kinetics log absorbance plots are of very similar shape to those presented. The plots again show an acceptable linear fitting, with

average $R$ values about 0.98, and photolysis kinetics seems again to obey a first-order law $y = kx + n$ where $y$ is log absorbance (the pigments absorption in hexane at 444 nm for lutein and 436 nm for neoxanthin), $x$ is the UV-irradiation time and $k$ is the rate constant for pigments bleaching.

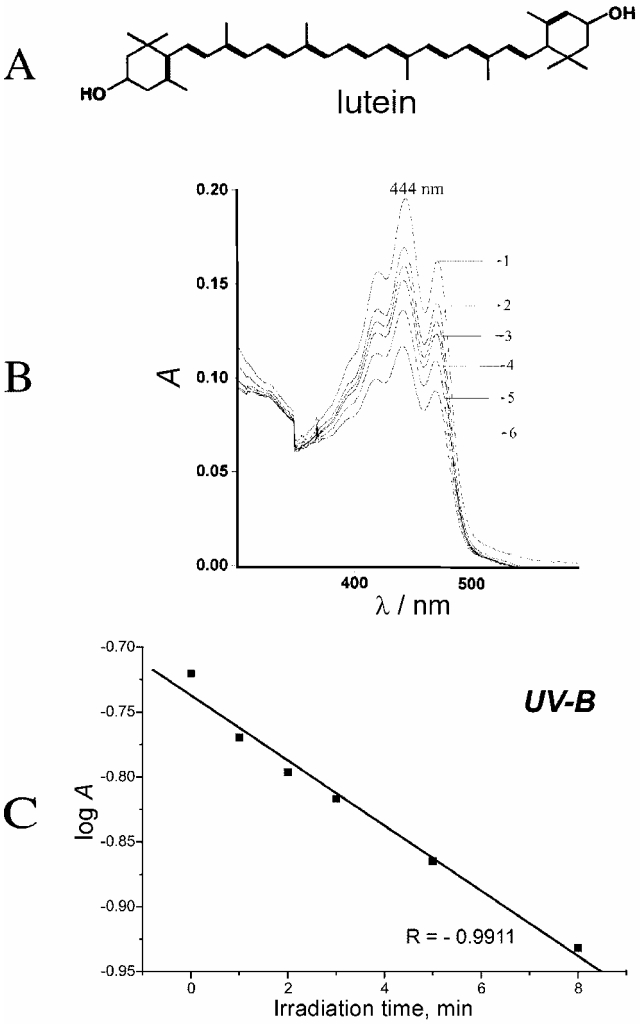


Fig. 3. (A) Structure of lutein; (B) changes in the absorption spectra of lutein exposed to UV-B radiation (300 nm) in hexane. The exposure time periods were: (1) 0 min; (2) 1 min; (3) 2 min; (4) 3 min; (5) 5 min; (6) 8 min. The approximate concentration of lutein was $1.3\times10^{-6}$ mol $dm^{-3}$; (C) the kinetic log absorbance plot of the bleaching of lutein in hexane against the time of UV-B irradiation. The absorbance of lutein was followed at 444 nm.

The calculated slopes ($k$) for each carotenoid and each radiation type are presented in Table I. Such a presentation provides for a comparison of the slopes, which reflect differences in the kinetics of pigments bleaching for all three UV-irradiation ranges. It therefore allows an insight into the pigments resistance toward UV-light.

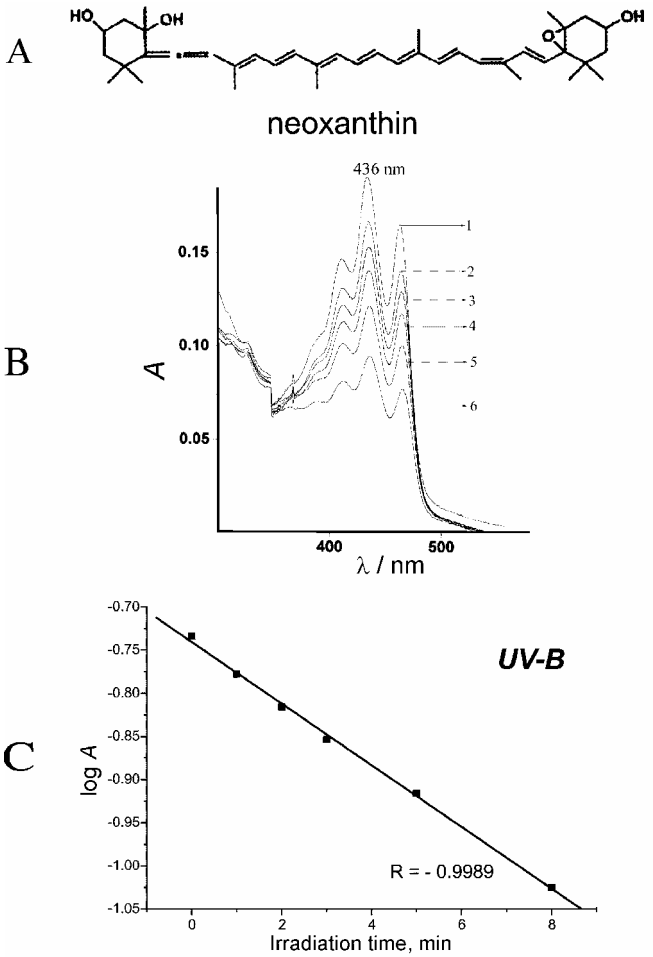


Fig. 4. (A) Structure of neoxanthin; (B) changes of the absorption spectra of neoxanthin exposed to UV-B radiation (300 nm) in hexane. The exposure time periods were: (1) 0 min; (2) 1 min; (3) 2 min; (4) 3 min; (5) 5 min; (6) 8 min. The approximate concentration of neoxanthin was $1.3\times10^{-6}$ mol $dm^{-3}$; (C) the kinetic log absorbance plot of the bleaching of neoxanthin in hexane against the time of UV-B irradiation. The absorbance of neoxanthin was followed at 436 nm.

## DISCUSSION

Carotenoids are usually $C_{40}$ tetraterpenoids built up from eight $C_5$ isoprenoid units. The basic linear and symmetrical skeleton can be cyclized at one or both ends. A significant characteristic is a long conjugated double-bond system, providing an extended π-delocalization, leading to a substantial bathochromic shift in the Vis region. The shift is responsible for the yellow, orange or red color of these compounds. Carotenoids consisting of only carbon and hydrogen are called carotenes, whereas those containing oxygen are called xanthophylls.

With an absorption maximum in the Vis region, carotenoids are obviously not efficient UV-absorbers but still are able to perform a protective function against UV-light in plants.[3,4] The explanation for such a behavior should be searched for not only in *in vivo* studies,[20,21] but also in basic studies, in very simple homogeneous solution media.

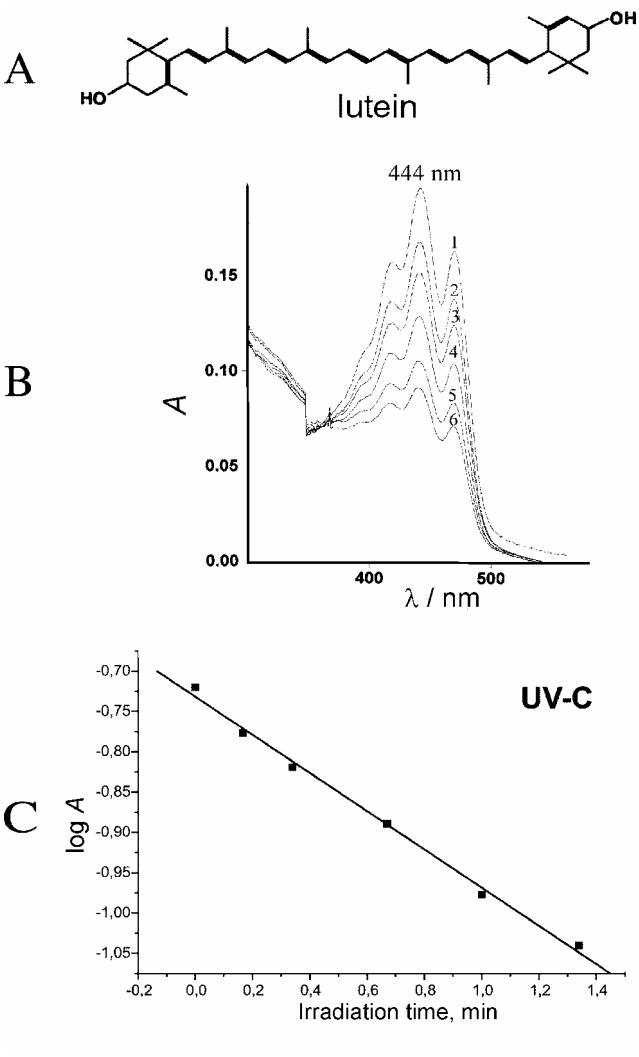


Fig 5. (A) Structure of lutein; (B) changes of the absorption spectra of lutein exposed to UV-C radiation (254 nm) in hexane. The exposure time periods were: (1) 0 min; (2) 0.17 min; (3) 0.34 min; (4) 0.67 min; (5) 1 min; (6) 1.34 min. The approximate concentration of lutein was $1.3\times10^{-6}$ mol dm$^{-3}$; (C) The kinetic log absorbance plot of the bleaching of lutein in hexane against time of UV-C irradiation. The absorbance of lutein was followed at 444 nm.

The other very important function of carotenoids, of global character, is their anti-oxidant function (this is one of the reasons for the wide use of carotenoids in the food industry[22,23]). For such a purpose, carotenoids may act in a preventive manner, *i.e.*, they inhibit the formation of reactive oxygen species (ROS) by reacting directly with oxygen, or, if radicals are already present, they act as chain-breaking anti-oxidants.[23–27] There are three possible mechanisms for carotenoid (CAR)–radical ($R^{\bullet}$) interactions: (*i*) radical addition or adduct formation ($CAR–R^{\bullet}$), (*ii*) electron-transfer reaction resulting in either a cation-radical ($CAR^{\bullet+}$), anion-radical ($CAR^{\bullet-}$) or a neutral alkyl-radical ($CAR^{\bullet}$), and (*iii*) hydrogen-abstraction, mostly related to the presence of carbonyl chromophores in

the involved radicals ($CAR + ROO^{\bullet} \rightarrow CAR^{\bullet} + ROOH$).[28–31] The cation-radicals ($CAR^{\bullet+}$) absorb strongly in the near-IR, with maxima in 900–1000 nm range.[32–34] The anion-radicals ($CAR^{\bullet-}$) also absorb strongly in the near-IR.[35] On the other hand, it is very difficult to characterize neutral carotenoid-radicals ($CAR^{\bullet}$), since they have no distinctive strong absorption, as observed for $CAR^{\bullet+}$ or $CAR^{\bullet-}$.[30] The possible occurrence of any of the cited mechanisms (*i–iii*) with carotenoids in hexane solution certainly depends on the chemical structures of the involved species.

TABLE I. Kinetics of pigment bleaching in hexane during increasing times of UV-irradiation for three different UV-ranges: 254 nm (UV-C), 300 nm (UV-B) and 350 nm (UV-A). The absorbances of $\beta$-carotene, lycopene, lutein and neoxanthin were followed at 448 nm, 470 nm, 444 nm and 436 nm, respectively. The kinetics obey a linear first-order plot: $y = kx + n$, where $y$ is log absorbance (the pigments absorption in hexane at 448 nm ($\beta$-carotene), 470 nm (lycopene), 444 nm (lutein) and 436 nm (neoxanthin)), $x$ the UV-irradiation time and $k$ is the first order rate constant for pigment bleaching.

| $\lambda_{UV}$ / nm | $k$ / min$^{-1}$ | | | |
|---|---|---|---|---|
| | $\beta$-Carotene ($A_{max}$ at 448 nm) | Lycopene ($A_{max}$ at 470 nm) | Lutein ($A_{max}$ at 444 nm) | Neoxanthin ($A_{max}$ at 436 nm) |
| 254 | 0.24434 | 0.60110 | 0.23685 | 0.47786 |
| 300 | 0.04205 | 0.05951 | 0.02510 | 0.03573 |
| 350 | 0.00261 | 0.00497 | 0.00228 | 0.00229 |

Since carotenoids, including the four studied here, are not efficient UV-absorbers, their increasing bleaching during prolonged UV-irradiation could be radical-mediated; if this occurs then the electron-transfer mechanism (*ii*)[28,30] appears more probable than the other two (*i* and *iii*). As reported, the reactions of $\beta$-carotene in organic solvents, specifically in an ionized hexane solution, are very fast and lead to the formation of strongly absorbing intermediates, $CAR^{\bullet+}$ and $CAR^{\bullet-}$.[35] Adduct formation (*i*) and hydrogen abstraction (*iii*) appear less probable. The Vis absorbance (*i.e.* the carotenoids spectra) should remain unaltered if the former mechanism occurs, since, as reported, the CAR-adducts ($CAR–R^{\bullet}$) have similar spectra to that of CAR itself,[30,31] and this is evidently not the case here (Figs. 1B, 2B, 3B, 4B and 5B); however, this mechanism can theoretically not be excluded as a possibility, but if it occurs short-lived adducts species are formed, which could not be detected with the techniques employed in this study. The hydrogen abstraction mechanism should be neglected because there are no carbonyl moieties, the most selective H-abstractors, present in the investigated solution.[36–38]

There is another hypothetical possibility that the production of at least one of the two CAR-ion-radicals involves ROS species, specifically the superoxide anion radical, $O_2^{\bullet-}$. The reports about the production of them *in vivo* under shorter,[39] or even longer UV-light[21,40] are not comparable with the system studied in

this work, although oxygen was certainly present in the hexane solutions.[41] However, even if $O_2^{\bullet-}$ were really present in solution, it should not affect the above discussion. Since there are neither $H^+$ ions nor free metal ions in solution, its conversion into hydrogen peroxide and then to hydroxyl radicals ($OH^\bullet$), also possible hydrogen abstraction agents[42,43] *via* the Fenton reaction,[44] is not possible. The possibility for adduct formation with $O_2$[23–26] can not hypothetically be excluded but if this occurs at all, it is to a minor extent since the adduct (CAR–$O_2$) has the same spectrum as CAR itself[30,31] and hence, the absorbance should not change significantly during UV-irradiation. The recorded spectra (Figs. 1B, 2B, 3B, 4B and 5B) show this was not the case. The presence of short-chain, oxygen--containing derivatives, indicating instabilities of the carotenoids in the presence of oxygen, which has been already reported,[45] and which should certainly be expressed through a blue-shift of the recorded spectra, was also not detected in this study (Figs. 1B, 2B, 3B, 4B and 5B).

The kinetic plots for the carotenes ($\beta$-carotene and lycopene, Figs. 1C and 2C) and the two xanthophylls (lutein and neoxanthin, Figs. 3C, 4C and 5C) are indications for the possible proposed mechanism of the involved bleaching of the carotenoids leading to $CAR^{\bullet+}$ formation, even independent of the UV-irradiation range. The two carotenes irradiated with UV-A and the two xanthophylls irradiated with UV-B both expressed obvious first-order kinetics, implying the rate of reaction is dependent on the carotenoid concentration. In a very relevant study performed in ionized hexane solution, the solvent itself was proposed to be an acceptor, preceded by $\beta$-carotene cation-radical formation.[35] As the solvent was present in a huge excess (compared to the carotenoids concentration), it does not affect the reaction rate.

The bleaching rates of the four investigated carotenoids (expressed as the slopes of the linear plots, $k$, in $min^{-1}$) for the three UV-ranges are presented in Table I. The results suggest that the bleaching rates are dependent on two factors: the type of UV-irradiation (*i.e.*, the energy of the photons) and the chemical structure of the carotenoid.

Concerning the photon energy input, it is clear from Table I that the bleaching rates decline approximately by one order of magnitude for all investigated carotenoids on going from UV-C to UV-A irradiation. The only exception is $\beta$-carotene, for which the ratio between the bleaching rates achieved by UV-C and UV-B radiation was about 6 and the ratio of the bleaching rates for UV-B and UV-A was about 20, which is about double the value when compared to the corresponding ratios obtained with the other carotenoids (Table I). For lycopene, lutein and neoxanthin the UV-C/UV-B and UV-B/UV-A ratios of the bleaching rates are close to 10, emphasizing the crucial governing role of the involved photons. Evidently, basic structural difference between the two carotenes and the two xanthophylls (absence or presence of oxygen, respectively), where lutein and

neoxanthin mimic the structure of β-carotene rather than that of lycopene (with cyclic, oxygen-containing moieties at the ends of the hydrocarbons chains) does not counter this fact.

However, the differences between the chemical structures of the investigated compounds (Figs. 1A, 2A, 3A and 4A) certainly play an undeniable role.

The bleaching rates of lycopene were higher than the ones of β-carotene for all three UV-ranges (Table I). However, the difference was the largest for UV-C (a ratio of 2.5), then for UV-A (1.9) and UV-B (1.42). Lycopene is clearly more reactive and the difference must be somehow connected to the absence of rings at the end of the hydrocarbon chain. For the xanthophylls, the situation is a little clearer. The ratios of the bleaching rates (neoxanthin/lutein, Table I) decreased proportionally from UV-C (2.0), *via* UV-B (1.42) to UV-A (1.0). Since neoxanthin contains two more oxygen atoms than lutein, (Figs. 4A and 3A, respectively), its higher reactivity could reasonably be related to the excess of unpaired electrons (compared to lutein). However, comparison between the carotenes and xanthophylls does not support such a suggestion. The bleaching rates for β-carotene and lutein (lutein containing two hydroxyl groups added to the carotene structure, Figs. 1A and 3A) are very close (particularly for the UV-C and UV-A range) but, on the other hand, the bleaching rates for lycopene (no oxygen, Fig. 2A) are remarkably higher than those of neoxanthin, for all three UV-ranges (Table I).

## CONCLUSIONS

To conclude, (1) even in this simplest possible (solution) system, carotenoids undergo degradation, *i.e.*, bleaching, when exposed to prolonged UV-irradiation; (2) their bleaching is probably free radicals-mediated and highly dependent and proportional to the energy input of the UV-photons; (3) the differences between the chemical structures of the investigated carotenoids do not counter conclusion (2), although a particular role of oxygen in the bleaching of xanthophylls, potentially, can not be excluded.

This study should be viewed as a basis for upcoming studies in more complex, microheterogeneous systems, such as oil/water emulsions (with carotenoids included), as carotenoids are raw materials for numerous cosmetic and pharmaceutical formulations for protection against UV-light[11−13] (specifically against the UV-B component which is increasingly present in the emission spectrum of sunlight) and related technologies. It will be interesting to see how a higher level of molecular organization affects the bleaching ratios established in this work.

## SUPPLEMENTARY MATERIAL

The changes in the spectra and log absorbance *vs.* time plots for all the examined carotenoids not given in the paper, as well as the emission profiles of the employed lamps are available electronically from http://www.shd.org.yu/JSCS/ or from the corresponding author on request.

*Acknowledgements*. Dragan Cvetković is a recipient of a fellowship granted by Ministry of Science of the Republic of Serbia.

И З В О Д

СТАБИЛНОСТ КАРОТЕНОИДА ПРЕМА UV-ОЗРАЧИВАЊУ У ХЕКСАНУ

ДРАГАН ЦВЕТКОВИЋ и ДЕЈАН МАРКОВИЋ

*Tehnolo{ki fakul t e t, Univerzi t e t u Ni{u, Bulevar oslobo|ewa 124, 16000 Leskovac*

У раду је испитивана стабилност 4 изабрана каротеноида (два каротена и два ксантофила) према ултраљубичастом зрачењу (UV) из три различита опсега (UV-A, UV-B и UV-C). Каротеноиди подлежу деструкцији, то јест обезбојавању путем вероватног слободно-радикалског механизма који се може описати кинетиком 1. реда. Константе брзине обезбојавања су врло зависне од енергија упадних фотона, и, мада не на конзистентан начин, од хемијских структура испитиваних једињења. Кад су у питању два испитивана ксантофила могућа улога кисеоника у њиховом обезбојавању не може бити негирана.

(Примљено 12. јануара 2007, ревидирано 8. августа 2007)

REFERENCES

1. M. Ichihashi, M. Ueda, A. Budiyannto, T. Bito, M. Oka, M. Fukunaga, K. Tsuru, T. Horikawa, *Toxicology* **189** (2003) 21
2. G. P. Pfeifer, Y. H. You, A. Besaratinia, *Mutat. Res.* **571** (2005) 19
3. A. H. Teramura, L. H. Ziska, in *Photosynthesis and the Environment*, Kluwer Academic Publishers, Dordrecht, 1996, p. 436
4. A. Strid, W. S. Chow, J. M. Anderson, *Biochim. Biophys. Acta* **1020** (1990) 260
5. T. Schwarz, *Eur. J. Dermatol.* **6** (1996) 227
6. B. J. Vermer, M. Wintzen, F. H. J. Claas, A. A. Schothorst, H. M. H. Hurks, *Eur. J. Dermatol.* **6** (1996) 231
7. A. R. Young, *Eur. J. Dermatol.* **6** (1996) 225
8. A. Ouhtit, H. N. Ananthaswamy, J. *Biomed. Biotechnol.* **1** (2001) 5
9. E. M. Middleton, A. H. Teramura, *Plant. Physiol.* **103** (1993) 741
10. H. Scheer, in *Light Harvesting Antenas in Photosynthesis*, B. R. Green, W. Parson, Eds., Kluwer Academic Publishers, Dordrecht, 2003, p. 29
11. A. Ambrogi, D. A. Cardarelli, R. Eggers, *Lat. Am. Appl. Res.* **33** (2003) 323
12. D. Bezbradica, J. Milić–Aškrabić, S. D. Petrović, S. Šiler–Marinković, *J. Serb. Chem. Soc.* **70** (2005) 115
13. A. Zeb, *J. Biol. Sci.* **4** (2004) 687
14. W. A. Swec, in *Chlorophylls*, H. Scheer, Ed., CRC-Press, Boca Raton, 1991, p. 89
15. W. A. Swec, in *The Porphyrins*, D. Dolphin, Ed., Academic Press, New York, 1978, p. 342
16. H. Brockman, N. Risch, in *Chlorophylls*, H. Scheer, Ed., CRC Press, Boca Raton, 1991, p. 103
17. W. W. Fish, P. Perkins–Veazie, J. K. Collins, *J. Food Compos. Anal.* **15** (2002) 309
18. *Phytoplankton pigments in oceanography: guidelines to modern methods*, S. W. Jeffrey, R. F. C. Mantoura, S. W. Wright, Eds., UNESCO Publishing, Paris, 1996.
19. C. H. Azevado–Maleiro, D. B. Rodrguez–Amaya, *J. Food Compos. Anal.* **17** (2004) 385
20. E. Hideg, C. Barta, T. Kalai, I. Vass, K. Hideg, K. Asada, *Plant Cell Photobiol.* **43** (2002) 1154
21. C. Barta, T. Kalai, K. Hideg, I. Vass, E. Hideg, *Funct. Plant Biol.* **31** (2004) 23
22. J. Paust, *Pure Appl. Chem.* **63** (1991) 45
23. R. Baker, C. Gunther, *Trends Food Sci.* **15** (2004) 484

24. K. Haila, *Academic dissertation*, University of Helsinki, Department of Applied Chemistry and Microbiology, Helsinki, 1999, p. 20
25. P. Palozza, N. I. Krinsky, *Methods Enzymol.* **213** (1992) 403
26. G. W. Burton, K. U. Ingold, *Science* **224** (1984) 569
27. A. A. Woodall, S. W. Lee, R. J. Weesie, M. J. Jackson, G. Britton, *Biochim. Biophys. Acta* **1336** (1997) 33
28. N. I. Krinsky, K.Yeum, *Biochem. Biophys. Res. Commun.* **305** (2003) 754
29. N. E. Polyakov, A. I. Kruppa, T. V. Leshina, T. A. Konovalova, L. D. Kispert, *Free Radical Biol. Med.* **31** (2001) 43
30. R. Edge, T. G. Truscott, *Spectrum* **13** (2000) 12
31. A. Mortensen, L. H. Skibsted, T. G. Truscott, *Arch. Biochem. Biophys.* **385** (2001) 13
32. N. Polyakov, V. V. Konovalov, T. V. Leshina, O. A. Luzina, N. F. Salakhutdinov, T. A. Konovalova, L. D. Kispert, *J. Photochem. Photobiol. A* **141** (2001) 117
33. J. A. Jeevarajan, C. C. Wei, A. S. Jeevarajan, L. D. Kispert, *J. Phys. Chem.* **100** (1996) 5637
34. C. A. Tracewell, J. S. Vrettos, J. A. Bautista, H. A. Frank, *Arch. Biochem. Biophys.* **385** (2001) 61
35. M. G. Simic, *Methods Enzymol.* **213** (1992) 444
36. D. Z. Markovic, L. K. Patterson, *Photochem. Photobiol.* **49** (1989) 531
37. D. Z. Markovic, T. Durand, L. K. Patterson, *Photochem. Photobiol.* **51** (1990) 389
38. D. Z. Markovic, L. K. Patterson, *Photochem. Photobiol.* **58** (1993) 329
39. P. Zhang, J. Yu, X. Tang, *J. Integ. Plant Biol.* **47** (2005) 683
40. M. E. Pospelov, G. Fraikin, *Akad. Nauk SSSR Biol.* **2** (1989) 308
41. I. Cibulka, A. Heintz, *Fluid Phase Equilibr.* **107** (1995) 235
42. M. G. J. Heijman, H. Nauta, Y. K. Levine, *Radiat. Phys. Chem.* **26** (1985) 73
43. J. Aikens, T. A. Dix, *Arch. Biochem. Biophys.* **305** (1993) 516
44. N. Mimica–Dukic, *Arh. Farm.* **5** (1997) 475
45. H. S. Black, *Nutr. Cancer* **31** (1998) 212.

Journal of the Serbian Chemical Society
JSCS@tmf.bg.ac.yu • www.shd.org.yu/JSCS
*J. Serb. Chem. Soc. 73* (1) 29–39 (2008)
*JSCS–3685*
UDC 547.831+546.650:66.061:620.168.3
*Original scientific paper*

# Crown ethers as synergistic agents in the solvent extraction of trivalent lanthanides with 8-hydroxyquinoline

M. ATANASSOVA*

*University of Chemical Technology and Metallurgy, Department of General and Inorganic Chemistry, 8 Kl. Okhridski, 1756, Sofia, Bulgaria*

(Received 17 July 2006)

*Abstract*: The liquid extraction of the 13 lanthanides with mixtures of 8-hydroxyquinoline (HQ) and crown ethers (S) dibenzo-18-crown-6 (DB18C6) and dibenzo-24-crown-8 (DB24C8) in 1,2-dichloroethane as a diluent from chloride medium at constant ionic strength $\mu = 0.1$ was investigated. The composition of the extracted species was established as $LnQ_3$ with HQ alone and as $LnQ_3 \cdot S$ in the presence of a crown ether. The values of the equilibrium constants were calculated. The addition of DB18C6 to the metal chelate system improved the extraction efficiency, while a weak synergistic enhancement was found when the metals were extracted with mixtures of HQ–DB24C8. The parameters of the extraction process were determined and the separation factors between two adjacent lanthanides(III) were calculated.

*Keywords*: synergistic extraction; 8-hydroxyquinoline; dibenzo-24-crown-8; dibenzo-18-crown-6; lanthanides separation factors.

## INTRODUCTION

The coordination chemistry of macrocyclic polyethers (commonly referred to as "crown" ethers) has been the subject of numerous investigations since the discovery of such compounds by Pedersen in 1967.[1] They are often used as synergistic additives to chelating, acidic or neutral extractants for the extraction of various metal ions. The synergistic solvent extraction of multi-charged transition ions,[2–4] lanthanide and actinide ions,[5–22] as well as alkali and alkaline earth metals[2–4] has been extensively studied using acidic chelating agents, *e.g.*, *β*-diketones and various crown ethers as synergists. It was found that the metal ions can be extracted synergistically. The formation of mixed adducts containing one or two crown ether molecules has been reported. In most cases, the separation of the lanthanides has also been discussed because of their chemical similarities, which makes their separation difficult. Reddy *et al.*[15–17] reported an increase of both

* E-mail: ma@uctm.edu
doi: 10.2298/JSC0801029A

the extractability and selectivity for the extraction of Nd, Eu and Tm with acylpyrazolones and 18C6, DCH18CH, or DB18C6.

A review of crown ether containing extraction systems has recently been published.[23] Only a few papers dealing with the extraction of Co(II) with mixtures of 8-hydroxyquinoline and DB18C6 have been published.[24,25] This provoked interest in extraction systems containing HQ, as a part of systematic studies of synergistic solvent extraction and the separation of lanthanide ions.

The aim of the present work was to study synergistic solvent extraction and separation of the metals of the entire lanthanide series (with the exception of Ce because of its unstable trivalent state and the radioactive Pm) using 8-hydroxyquinoline (HQ) and dibenzo-18-crown-6 (DB18C6) or dibenzo-24-crown-8 (DB24C8) in 1,2-dichloroethane. The conditions of the extraction experiment, the probable mechanism of extraction process, as well as the composition of the metal complexes transferred into the organic phase are specified.

## EXPERIMENTAL

### *Reagents*

The commercial products 8-hydroxyquinoline (Riedel-de Haen, 99 %), dibenzo-24-crown-8 (Fluka, > 98 %) and dibenzo-18-crown-6 (Fluka, >98 %) were used as received. The diluent was 1,2-dichloroethane (Merck, p.a.). Stock solutions of the metals were prepared from their oxides (Fluka, puriss). Arsenazo III (Fluka) was of analytical grade purity, as were the other employed reagents.

### *Apparatus*

An S-20 spectrophotometer, Boeco (Germany) was used for measuring the absorbances. A pH 211 HANNA digital pH meter was used for the pH measurements.

### *Procedure*

The experiments were performed using 10 $cm^3$ volumes of the aqueous and organic phases. The samples were shaken mechanically for 45 min at room temperature, which was sufficient for equilibrium to be attained. After the separation of the phases, the metal concentration in the aqueous phase was determined photometrically using Arsenazo III.[26] The acidity of the aqueous phase was measured by a pH-meter with an accuracy of 0.01 pH units. The ionic strength was maintained at 0.1 M with (Na,H)Cl. The initial concentration of the metals in all experiments was $2.5\times10^{-4}$ mol $dm^{-3}$.

## RESULTS AND DISCUSSION

### *Solvent extraction of $Ln^{3+}$ ions with 8-hydroxyquinoline or crown ethers alone*

The extraction behavior of the lanthanide ions using HQ in 1,2-dichloroethane was studied as a function of pH and [HQ]. The plots of log $D$ ($D$ is the distribution coefficient for the extraction with HQ alone) *vs.* pH and log [HQ] were linear, with slopes close to three (these plots are not shown).

Hence, the extraction of $Ln^{3+}$ ions can be described by the equation:

$$Ln^{3+}_{(aq)} + 3HQ_{(o)} \rightleftharpoons LnQ_{3(o)} + 3H^{+}_{(aq)} \quad (1)$$

where Ln denote a lanthanide and “aq” and “o”, the aqueous and organic phase, respectively.

The formation of chelates was found in some other studies.[27] It was stated that all the investigated Ln(III) ions were extracted with HQ, as well as with Hdbq (5,7-dibromo-8-hydroxyquinoline) as simple 1:3 chelates into chloroform.[28] However, $Ho^{3+}$ and $Er^{3+}$ were extracted with Hdcq (5,7-dichloro-8-hydroxyquinoline) as self-adducts of the type $Ln(dcq)_3 \cdot Hdcq$.[29] Moreover, in the extraction of $Gd^{3+}$ with HQ, as well as $Pr^{3+}$, $Dy^{3+}$ and $Yb^{3+}$ with Hdcq,[30] the existence of both of the chelates ($GdQ_3$ or $Ln(dcq)_3$) and the self-adducts ($GdQ_3 \cdot HQ$ or $Ln(dcq)_3 \cdot Hdcq$) were observed. It is further reported[31] that $Nd^{3+}$ is extracted as $Nd(dbq)_3$, as are other $Ln^{3+}$ (La, Gd and Lu) as $Ln(dbq)_3$ into $CHCl_3$.

As the partition of HQ towards the aqueous phase is very low,[32] the relationship between the distribution coefficient $D_Q$ and the equilibrium constant $K_Q$ can be expressed as:

$$\log K_Q = \log D_Q - 3\mathrm{pH} - 3\log [HQ] \quad (2)$$

The values of the equilibrium constant $K_Q$ are given in Table I. It can be seen that they increase with decreasing radius of the $Ln^{3+}$ ion. The increase in the extractability along the lanthanide series can be due to the increase in electrostatic interaction between the cation and the ligand with decreasing ionic radius.[22]

The experimental data show that the extraction of the lanthanides(III) with both DB18C6 and DB24C8 alone was negligible under the experimental conditions employed in the present study.

TABLE I. Values of the equilibrium constants $K_{Q,S}$ and $\beta_{Q,S}$ for the extraction of lanthanide metals with HQ−DB24C8 and HQ−DB18C6 mixtures in 1,2-dichloroethane

| $Ln^{3+}$ | $\log K_Q$ | $\log K_{Q,S}$ | | $\log \beta_{Q,S}$ | |
|---|---|---|---|---|---|
| | | DB24C8 | DB18C6 | DB24C8 | DB18C6 |
| La | –15.95 | –13.52 | –13.42 | 2.35 | 2.53 |
| Pr | –15.30 | –12.74 | –12.54 | 2.56 | 2.76 |
| Nd | –15.00 | –12.58 | –11.96 | 2.42 | 3.04 |
| Sm | –14.35 | –11.96 | –11.30 | 2.39 | 3.05 |
| Eu | –14.12 | –11.60 | –10.58 | 2.60 | 3.54 |
| Gd | –13.90 | –11.36 | –10.06 | 2.54 | 3.84 |
| Tb | –13.60 | –11.02 | –9.82 | 2.58 | 3.78 |
| Dy | –13.40 | –10.83 | –9.56 | 2.57 | 3.84 |
| Ho | –13.15 | –10.64 | –9.28 | 2.51 | 3.87 |
| Er | –12.98 | –10.44 | –8.84 | 2.54 | 4.14 |
| Tm | –12.82 | –10.24 | –8.44 | 2.58 | 4.38 |
| Yb | –12.64 | –10.11 | –8.06 | 2.53 | 4.58 |
| Lu | –12.38 | –9.87 | –7.70 | 2.51 | 4.68 |

*Solvent extraction of $Ln^{3+}$ ions with mixtures of HQ and DB18C6 or DB24C8*

The synergistic solvent extraction of $Ln^{3+}$ ions with mixtures of HQ and DB18C6 or DB24C8 (S) can be expressed by the equation:

$$Ln^{3+}_{(aq)} + mHQ_{(o)} + nS_{(o)} \rightleftharpoons LnQ_m \cdot S_{n(o)} + mH^+_{(aq)} \quad (3)$$

It may be shown easily that:

$$\log D_{Q,S} = \log K_{Q,S} + m\log [HQ] + n\log [S] + m\text{pH} \quad (4)$$

where $D_{Q,S}$ is the distribution coefficient due to the synergistic effect.

As the lanthanide extraction with the crown ethers was negligible under the experimental conditions employed in the present study, the values of the experimentally obtained distribution coefficient $D$ is the sum of $D_{Q,S}$ and $D_Q$. Hence, the values of $D_{Q,S}$ can be calculated as $D - D_Q$. If hydrolysis and complexation in the aqueous phase, as well as polymerization in the organic phase occur to a negligible extent only, then the double logarithmic plots of $D_{Q,S}$ *vs.* one of the variables $[H^+]$, [HQ] or [DB18C6(DB24C8)], keeping the other two constant, should be linear and the slopes will give the number of the ligands participating in the formation of the adduct.

The experimental data for the extraction of the lanthanides with mixtures of HQ and DB18C6 or DB24C8 are shown in Figs. 1–6. The plots of log $D_{Q,S}$ *vs.* pH and log [HQ] are linear with slopes of three while the plots of log $D_{Q,S}$ *vs.* [S] exhibit slopes equal to one. On the basis of the analysis of the slope data, the synergistic extraction of lanthanides can be described by the following reaction:

$$Ln^{3+}_{(aq)} + 3HQ_{(o)} + S_{(o)} \rightleftharpoons LnQ_3 \cdot S_{(o)} + 3H^+_{(aq)} \quad (5)$$

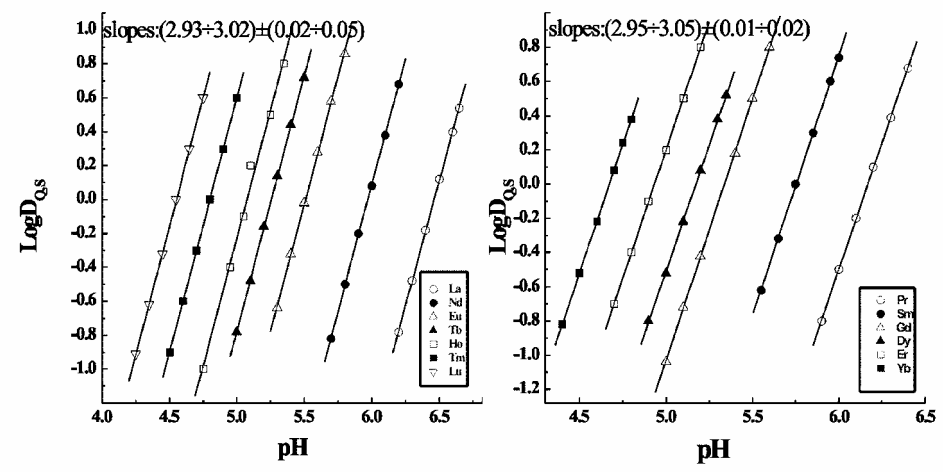


Fig. 1. log $D_{Q,S}$ *vs.* pH for the extraction of lanthanide(III) ions with HQ–DB18C6 mixture at [HQ] = $6\times10^{-2}$ mol $dm^{-3}$ and [DB18C6] = $5\times10^{-3}$ mol $dm^{-3}$.

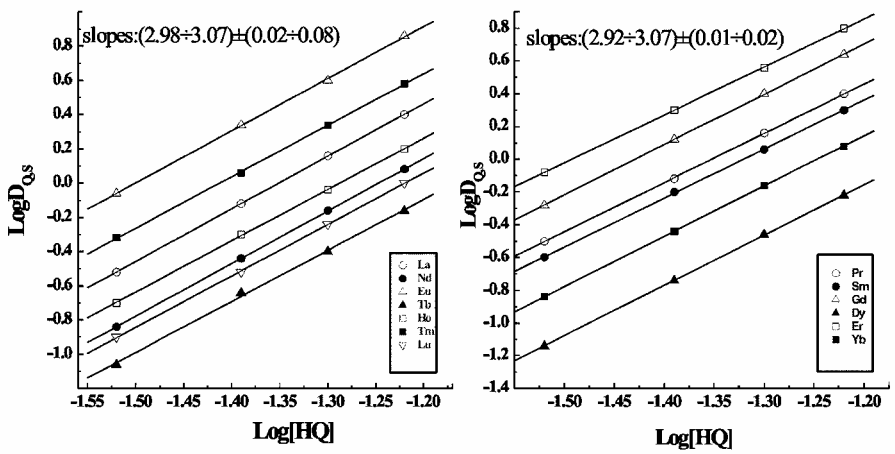


Fig. 2. log $D_{Q,S}$ *vs*. log [HQ] for the extraction of lanthanide(III) ions with the mixture HQ–DB18C6 at [DB18C6] = $5\times10^{-3}$ mol dm$^{-3}$ (La, pH 6.60; Nd, pH 6.00; Eu, pH 5.80; Tb, pH 5.20; Ho, pH 5.15; Tm, pH 5.00; Lu, pH 4.55; Pr, pH 6.30; Sm, pH 5.85; Gd, pH 5.55; Dy, pH 5.10; Er, pH 5.20; Yb, pH 4.70).

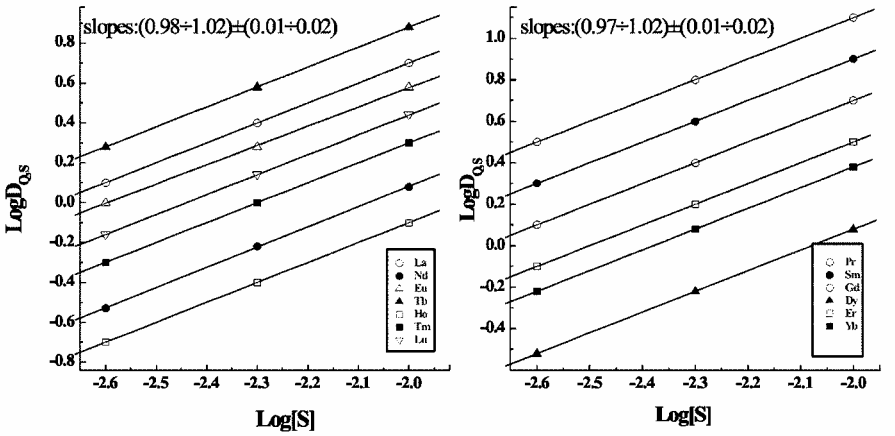


Fig. 3. log $D_{Q,S}$ *vs*. log [DB18C6] for the extraction of lanthanide(III) ions with the mixture HQ–DB18C6 at [HQ] = $6\times10^{-2}$ mol dm$^{-3}$ (La, pH 6.60; Nd, pH 5.90; Eu, pH 5.60; Tb, pH 5.45; Ho, pH 4.95; Tm, pH 4.80; Lu, pH 4.60; Pr, pH 6.30; Sm, pH 5.95; Gd, pH 5.60; Dy, pH 5.10; Er, pH 5.00; Yb, pH 4.70).

The same type of mixed adduct complexes (Ln(TTA)$_3$·S) was established for the synergistic solvent extraction of metals of entire 4f-series with the chelating extractant HTTA and the crown ethers DB18C6 and DB24C8.[19] Reddy *et al.*,[15–17,20,22] Dukov *et al.*[10] and Ensor and Shah[33] have also reported the involvement of one molecule of the crown ether in the synergistic species when trivalent lanthanides were extracted with chelating extractants and various crown ethers.

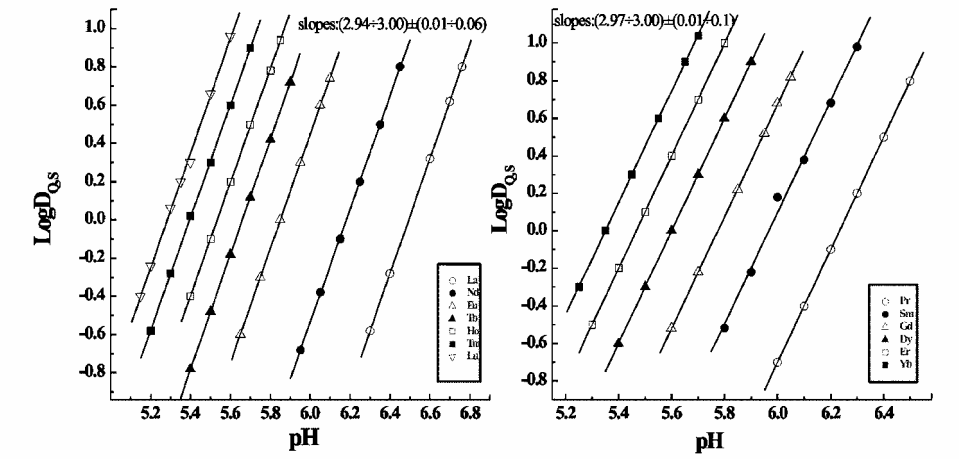


Fig. 4. log $D_{Q,S}$ *vs*. pH for the extraction of lanthanide(III) ions with the HQ−DB24C8 mixture at [HQ] = $6\times10^{-2}$ mol dm$^{-3}$ and [DB24C8] = $5\times10^{-3}$ mol dm$^{-3}$.

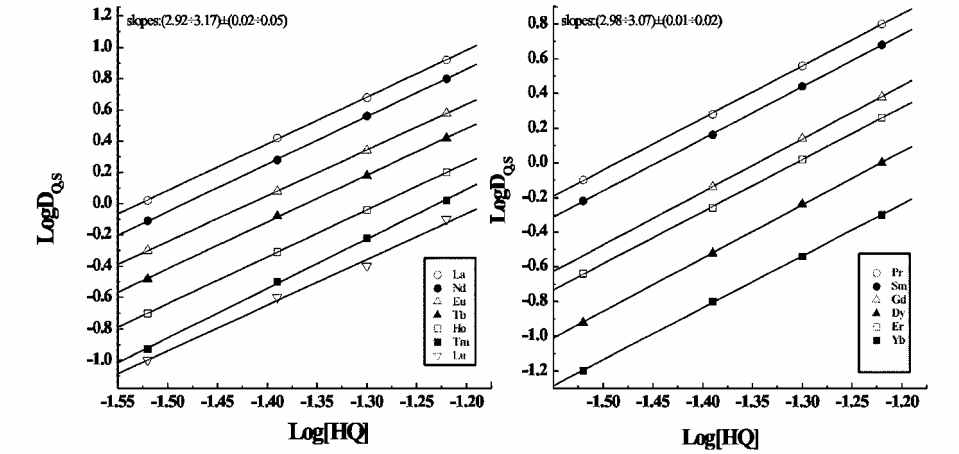


Fig. 5. log $D_{Q,S}$ *vs*. log [HQ] for the extraction of lanthanide(III) ions with the mixture HQ−DB24C8 at [DB24C8] = $5\times10^{-3}$ mol dm$^{-3}$ (La, pH 6.80; Nd, pH 6.45; Eu, pH 6.05; Tb, pH 5.80; Ho, pH 5.60; Tm, pH 5.40; Lu, pH 5.25; Pr, pH 6.50; Sm, pH 6.20; Gd, pH 5.90; Dy, pH 5.60; Er, pH 5.55; Yb, pH 5.25).

The overall equilibrium constant $K_{Q,S}$ can be determined from the equation:

$$\log K_{Q,S} = \log D_{Q,S} - 3\log [HQ] - \log [S] - 3pH \quad (6)$$

The formation of mixed adducts in the organic phase can be represented by the equation:

$$LnQ_{3(o)} + S_{(o)} \rightleftharpoons LnQ_3{\cdot}S_{(o)} \quad (7)$$

The equilibrium constant $\beta_{Q,S}$ for the synergistic reaction of the organic phase can be determined as:

$$\log \beta_{Q,S} = \log K_{Q,S} - \log K_Q \quad (8)$$

Since the partition coefficient of the employed crown ether ($\log K_D$, DB18C6 = 4.0) are known to be quite large, no correction is necessary for the partitioning of this crown ether in the aqueous phase.[16] It was assured that this is also true for DB24C8. The values of $\log K_{Q,S}$ and $\log \beta_{Q,S}$ (together with the values of $\log K_Q$) are given in Table I.

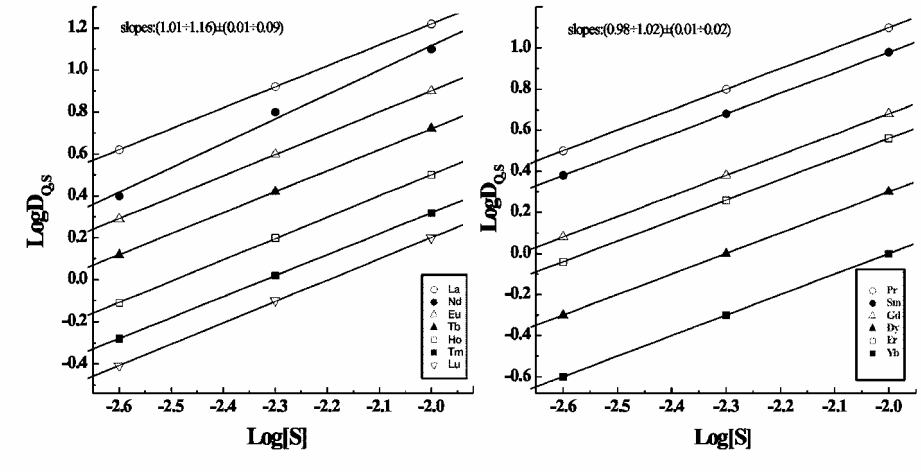


Fig. 6. $\log D_{Q,S}$ *vs*. log [DB24C8] for the extraction of lanthanide(III) ions with the mixture HQ−DB24C8 at [HQ] = $6\times10^{-2}$ mol $dm^{-3}$. (La, pH 6.80; Nd, pH 6.45; Eu, pH 6.05; Tb, pH 5.80; Ho, pH 5.60; Tm, pH 5.40; Lu, pH 5.25; Pr, pH 6.50; Sm, pH 6.20; Gd, pH 5.90; Dy, pH 5.60; Er, pH 5.55; Yb, pH 5.25).

The equilibrium constants are based on the assumption that the activity coefficients of the species do not change significantly under the experimental conditions. The data in Table I show that the value of $\log K_{Q,S}$ increases from La to Lu with decreasing ionic radius of the metal ion. The variation of the equilibrium constants $K_Q$ and $K_{Q,S}$ *vs.* the atomic number $Z$ of the lanthanide is given in Fig. 7, from which it can be seen that the three curves vary practically in the same manner.

The strength of the complexation of trivalent lanthanides follows the order: DB18C6 > DB24C8. DB24C8 is too large (4.5 to 5.6 Å)[34] to form a stable complex with HQ and maybe the decrease of the complexation reflects increasing steric effects.

Comparison of these results with the data found in a recent study[19] for the system HTTA−DB18C6 (DB24C8) showed the opposite tendency. The values of the equilibrium constants, as well as those of the synergistic coefficient were higher when DB24C8 was used as the synergistic agent but the difference bet-

ween these values for the two crown ethers decreased with increasing atomic number. This fact can be explained taking into account that HQ is a weaker acid ($pK_a$ = 9.65)[32] than HTTA ($pK_a$ = 6.2).[35] It is well known that the acidity of the extractant is one of the predominant factors governing extractability, *i.e.*, the lower the $pK_a$ value, the larger is $\log K_{exc}$. Torkestani *et al.*,[36] Sekine *et al.*,[37] and Reddy and coworkers[22] stated that the interaction between the chelating agent and a neutral oxo-donor in $CHCl_3$ are, in general, weaker when the diluent itself has strong interaction with the oxo-donor. However, the difference in the polarity of the diluents is higher (dielectric constant of chloroform = 4.9, 1,2-dichloroethane = 10.4). Hence, the present results demonstrate that steric effects are significant (cavity size and the properties of the extractant).

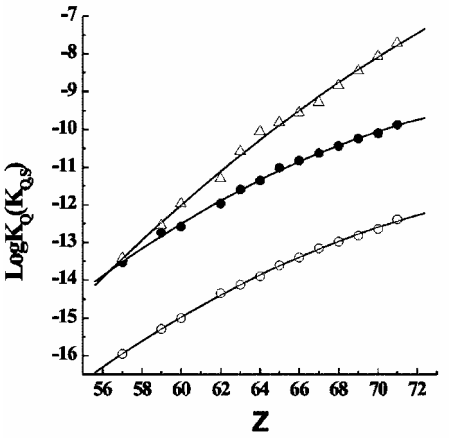


Fig. 7. $\log K_Q(K_{Q,S})$ *vs.* $Z$ (open circles: HQ; solid circles: HQ−DB24C8; triangles: HQ−DB18C6).

The synergistic enhancement obtained for the combination of two extractants can be evaluated calculating the synergistic coefficients (*SC*):[38]

$$SC = \log (D_{1,2}/D_1 + D_2)$$

where $D_{1,2}$, $D_1$ and $D_2$ denote the distribution coefficient of a metal ion using a mixture of extractants ($D_{1,2}$) and using the same extractants individually ($D_1$ and $D_2$). The values of the synergistic coefficients of the lanthanide ions when DB18C6 and DB24C8 were used as synergistic agents in combination with HQ are given in Table II. The synergistic enhancement increased from La to Lu for the HQ−DB18C6 mixture, while the values of the *SC* obtained for the HQ−DB24C8 mixture are almost the same. Reddy *et al.*[22] also reported that the synergistic constant increased from $Nd^{3+}$, $Eu^{3+}$ to $Tm^{3+}$ in their extraction with mixtures of 3-phenyl-4-(4-fluorobenzoyl)-5-isoxazolone and various crown ethers.

The separation factors between the lanthanides, defined as the ratios of the respective equilibrium constants $K_{Q,S}$ are also listed in Table II. The addition of DB18C6 to the $Ln^{3+}$−HQ system improves the separation. Thus, the synergistic mixtures, used in the present study, combine extraction efficiency with improved

selectivity as compared to HQ. It can be seem from Table II that the separation factors obtained for the extraction of the lanthanide ions with HQ alone and those with the HQ−DB24C8 combination do not differ to a large extent.

TABLE II. Values of the synergistic coefficients ([HQ] = $6\times10^{-2}$ mol dm$^{-3}$, [S] = $5\times10^{-3}$ mol dm$^{-3}$, pH = 5.50) and separation factors for the lanthanide extraction with HQ alone, as well as with HQ−DB24C8 or HQ−DB18C6 in 1,2-dichloroethane

| $Ln^{3+}$ | *SC* | | | *SF* | | |
|---|---|---|---|---|---|---|
| | DB24C8 | DB18C6 | | HQ | HQ−DB24C8 | HQ−DB18C6 |
| La | 0.13 | 0.22 | Pr/La | 4.46 | 7.24 | 7.58 |
| Pr | 0.26 | 0.46 | Nd/Pr | 1.99 | 1.44 | 3.80 |
| Nd | 0.12 | 0.73 | Sm/Nd | 4.46 | 4.16 | 4.57 |
| Sm | 0.10 | 0.74 | Eu/Sm | 1.69 | 2.29 | 5.24 |
| Eu | 0.22 | 1.32 | Gd/Eu | 1.65 | 1.74 | 3.31 |
| Gd | 0.24 | 1.54 | Tb/Gd | 1.99 | 2.18 | 1.74 |
| Tb | 0.28 | 1.78 | Dy/Tb | 1.58 | 1.54 | 1.82 |
| Dy | 0.27 | 1.54 | Ho/Dy | 1.77 | 1.54 | 1.90 |
| Ho | 0.21 | 1.57 | Er/Ho | 1.47 | 1.58 | 2.75 |
| Er | 0.24 | 1.56 | Tm/Er | 1.44 | 1.58 | 3.63 |
| Tm | 0.28 | 2.08 | Yb/Tm | 1.52 | 1.35 | 2.90 |
| Yb | 0.23 | 2.28 | Lu/Yb | 1.82 | 1.74 | 2.49 |
| Lu | 0.21 | 2.38 | | | | |

It is interesting to compare the separation factors obtained for the extraction of lanthanides with various chelating extractants and DB18C6. Reddy *et al.*[15−17,20,22] published data for the separation factors of the pairs Eu/Nd and Tm/Eu for various chelating extractants, *viz.* 4,4,4-trifluoro-1-phenyl-1,3-butanedione (HBTFA), 1-phenyl-3-methyl-4-trifluoroacetyl-5-pyrazolone (HPMTFP), 1-phenyl-3-methyl-4-pivaloyl-5-pyrazolone (HPMPP), 3-phenyl-4-(4-fluorobenzoyl)-5-isoxazolone (HFBPI) and 3-phenyl-4-benzoyl-5-isoxazolone (HPBI) with DB18C6. The separation factors for these systems are listed in Table III, together with the data obtained in the study,[19] from which it can be seen that HQ, which is a much poorer extractant for lanthanides than $\beta$-diketones, exhibits a quite high separation factor for the pairs Eu/Nd and Tm/Eu.

TABLE III. Values of the separation factors for the pairs Eu/Nd and Tm/Eu

| Extractants | Eu/Nd | Tm/Eu |
|---|---|---|
| HQ−DB18C6 | 23.98 | 138.04 |
| HTTA−DB18C6[19] | 3.7 | 17.0 |
| HPMTFP−DB18C6[15] | 21.4 | 3.6 |
| HPBI−DB18C6[20] | 25.1 | 1.2 |
| HBTFA−DB18C6[16] | 20.2 | 5.1 |
| HPMPP−DB18C6[17] | 47.9 | 13.4 |
| HFBPI−DB18C6[22] | 4.78 | 1.75 |

## CONCLUSION

The extraction equilibriums of trivalent lanthanides with 8-hydroxyquinoline and with mixtures of HQ and DB18C6 or DB24C8 were investigated. The experimental data show that the $Ln^{3+}$ ions were extracted as $LnQ_3$ and $LnQ_3{-}S$. The equilibrium constants of the synergistic species were found to increase monotonically with decreasing ionic radii of the metal ions. The synergistic enhancement factors, as well as the separation factors between adjacent metal ions, were large when DB18C6 was used as the synergistic agent in combination with HQ.

## И З В О Д

## КРУНСКИ ЕТРИ КАО СИНЕРГИСТИЧКИ ЧИНИОЦИ ПРИ ЕКСТРАКЦИЈИ ТРОВАЛЕНТНИХ ЛАНТАНИДА 8-ХИДРОКСИХИНОЛИНОМ

M. ATANASSOVA

*University of Chemical Technology and Metallurgy, Department of General and Inorganic Chemistry, 8 Kl. Okhridski, 1756, Sofia, Bulgaria*

Испитивана је екстракција у течној фази 13 лантанида смешом 8-хидроксихинолина (HQ) и крунских етара (S), дибензо-18-круна-6 (DB18C6) и дибензо-24-круна-8 (DB24C8), у 1,2-дихлороетану као разблаживачу, из хлоридне средине и при јонској јачини $\mu$ = 0,1. За врсте екстраховане са HQ установљен је састав $LnQ_3$, а LnQ3·S у присуству крунских етара. Израчунате су вредности константи равнотеже. Додавање DB18C6 метал–хелатном систему побољшава ефикасност екстракције, док су слаба синергистичка побољшања добијена уколико се метали екстрахују смешом HQ−DB24C8. Одређени су параметри процеса екстракције и израчунати сепарациони фактори суседних тровалентних лантанида.

(Примљено 17. јула 2006)

## REFERENCES

1. C. J. Pedersen, *J. Am. Chem. Soc.* **89** (1967) 7017
2. M. Lakkis, J. P. Brunette, M. J. F. Leroy, *Solvent Extr. Ion Exch.* **4** (1986) 287
3. A. M. Sastre, A. Sahmoune, J. P. Brunette, M. J. F. Leroy, *Solvent Extr. Ion Exch.* **7** (1989) 395
4. N. E. Kroutchinina, A. Sahmoune, J. P. Brunette, M. J. F. Leroy, *Solvent Extr. Ion Exch.* **5** (1987) 73
5. G. M. Nair, D. R. Prabhu, *J. Radioanal. Nucl. Chem., Articles* **121** (1988) 83
6. S. M. Khalifa, N. Zakaeia, H. F. Aly, *J. Radioanal. Nucl. Chem., Articles* **125** (1988) 373
7. H. F. Aly, S. M. Khalifa, M. M. El–Dessouky, F. A. Shehata, J. D. Navratil, *Proceedings of International Solvent Extraction Conference (ISEC86)*, Munchen, 1986, Prepr. Vol. 2, Frankfurt/M., Dechama, 1986, p. II-539
8. J. N. Mathur, P. K. Khopkar, *Solvent Extr. Ion Exch.* **6** (1988) 111
9. J. N. Mathur, *Solvent Extr. Ion Exch.* **8** (1990) 629
10. I. L. Dukov, *Solvent Extr. Ion Exch.* **10** (1992) 637
11. I. L. Dukov, *Monatsh. Chem.* **124** (1993) 689
12. Y. Kitatsuji, Y. Meguro, Z. Yoshida, *Solvent Extr. Ion Exch.* **13** (1995) 289
13. Y. Meguro, Z. Yoshida, *Radiochim. Acta* **65** (1994) 19
14. N. Yamamoto, N. Hirayama, T. Honjo, *Solvent Extr. Res. Dev., Jpn.* **6** (1999) 182

15. P. Takur, K. C. Dash, M. L. P. Reddy, R. Luxmi Varma, T. R. Ramanohan, A. D. Damodaran, *Radiochim. Acta* **75** (1996) 11
16. M. L. P. Reddy, R. Luxmi Varma, T. R. Ramamohan, *Radiochim. Acta* **80** (1998) 151
17. R. Pavitran, R. Luxmi Varma, M. L. P. Reddy, *Solvent Extr. Ion Exch.* **21** (2003) 797
18. S. Banerjee, S. Bhattacharya, S. Basu, *Spectrochim. Acta A* **61** (2005) 1039
19. M. Atanassova, I. L. Dukov, *Sep. Sci. Technol.* **40** (2005) 1103
20. M. L. P. Reddy, R. Luxmi Varma, T. R. Ramamohan, A. D. Damodaran, *Solvent Extr. Ion Exch.* **15** (1997) 49.
21. R. Pavitran, M. L. P. Reddy, *Radiochim. Acta* **91** (2003) 163
22. R. Pavitran, M. L. P. Reddy, *Radiochim. Acta* **92** (2004) 31
23. A. H. Bond, M. L. Dietz, R. Chiarizia, *Ind. Eng. Chem. Res.* **39** (2000) 3442
24. S. I. El Dessouky, J. A. Daoud, H. F. Aly, *Radiochim. Acta* **85** (1999) 79
25. F. A. Shehata, S. I. El Dessouky, H. F. Aly, *J. Radioanal. Nucl. Chem.* **240** (1999) 209
26. S. B. Savvin, *Arsenazo III*, Atomizdat, Moscow, 1966, p. 177
27. D. Czakis–Sulikowska, N. Pustelnik, *Solvent Extr. Ion Exch.* **21** (2003) 751
28. D. Czakis–Sulikowska, B. Kuznik, *Chem. Anal. (Warsaw)* **44** (1999) 925
29. D. Czakis–Sulikowska, B. Kuznik, *Chem. Anal. (Warsaw)* **38** (1993) 53
30. D. Czakis–Sulikowska, N. Pustelnik, *Chem. Anal. (Warsaw)* **42** (1997) 23
31. D. Czakis–Sulikowska, B. Kuznik, *Chem. Anal. (Warsaw)* **46** (2001) 93
32. E. A. Mazurenko, *Spravochnik po ekstrakchii*, Technika, Kiev, 1972, p. 169
33. D. D. Ensor, A. A. Shah, *J. Radioanal. Nucl. Chem. Lett.* **127** (1988) 235
34. J. P. Brunette, *4. Extraktionsseminar des Zentralinstitut fur Festkorperphysik und Werksstofforschung*, Holzlan, G. D. R., 1989, *Chemische Technik* **41** (1989) 494
35. A. K. De, M. Khopkar, *J. Sci. Ind. Res.* **21A** (1962) 131
36. K. Torkestani, G. J. Goetz–Grandmont, J. P. Brunette, *Analysis* **28** (2000) 324
37. T. Sekine, T. Saitou, H. Iga, *Bull. Chem. Soc. Jpn.* **56** (1983) 700
38. J. N. Mathur, *Sep. Sci. Technol.* **1** (1983) 349.

Journal of the Serbian Chemical Society
JSCS@tmf.bg.ac.yu • www.shd.org.yu/JSCS

*J. Serb. Chem. Soc.* *73* (1) 41–53 (2008)
*JSCS–3686*

UDC 531.3+54.02:539.193:536.7
*Original scientific paper*

# On the dynamics of some small structural motifs in rRNA upon ligand binding

ALEKSANDRA RAKIĆ[1#] and PETAR M. MITRAŠINOVIĆ[2*#]

[1]*Faculty of Physical Chemistry, University of Belgrade, Studentski trg 12–16, 11000 Belgrade and* [2]*Center for Multidisciplinary Studies, University of Belgrade, Kneza Višeslava 1, 11030 Belgrade, Serbia*

(Received 18 January 2007)

*Abstract*: The present study characterizes using molecular dynamics simulations the behavior of the GAA (1186–1188) hairpin triloops with their closing c–g base pairs in large ribonucleoligand complexes (PDB IDs: 1njn, 1nwy, 1jzx). The relative energies of the motifs in the complexes with respect to that in the reference structure (unbound form of rRNA; PDB ID: 1njp) display the trends that agree with those of the conformational parameters reported in a previous study[1] utilizing the *de novo* pseudotorsional ($\eta$,$\theta$) approach. The RNA regions around the actual RNA–ligand contacts, which experience the most substantial conformational changes upon formation of the complexes were identified. The thermodynamic parameters, based on a two-state conformational model of RNA sequences containing 15, 21 and 27 nucleotides in the immediate vicinity of the particular binding sites, were evaluated. From a more structural standpoint, the strain of a triloop, being far from the specific contacts and interacting primarily with other parts of the ribosome, was established as a structural feature which conforms to the trend of the average values of the thermodynamic variables corresponding to the three motifs defined by the 15-, 21- and 27-nucleotide sequences. From a more functional standpoint, RNA–ligand recognition is suggested to be presumably dictated by the types of ligands in the complexes.

*Keywords*: rRNA; ligand binding; small motifs; molecular dynamics; thermodynamics.

## INTRODUCTION

Tertiary structures are of vital importance in providing a structural basis for and support of biological hypotheses. Folded RNA molecules are constructed from extensive networks of interactions between various molecular building blocks, RNA motifs. Hence, knowledge of the structural and functional features of RNA

# Serbian Chemical Society member.
* Corresponding author. E-mail: petar.mitrasinovic@cms.bg.ac.yu
doi: 10.2298/JSC0801041R

motifs is indispensable for understanding the form and stability of the tertiary structure of RNA. In a previous study[1] the conformational differences between hairpin triloops in large ribonucleoligand complexes, induced by ligand binding to an unbound form of rRNA, were extensively explored using a pseudotorsional ($\eta,\theta$) approach.[2] Even though the differences between the compared structures were detectable using various representations of the RNA structure, such as Cartesian coordinates,[3] standard backbone torsion angles[4] and root-mean-square deviation (RMSD),[5] a reduced representation of RNA conformational space based on pseudotorsions ($\eta,\theta$) of two virtual bonds of individual nucleotides is more likely to register conformational peculiarities with a higher sensitivity.[6] Two pseudotorsions around these virtual bonds, extending from P to C4' and from C4' to P of the adjacent nucleotide,[7] are $\eta$ (C4'$_{i-1}$ − P$_i$ − C4'$_i$ − P$_{i+1}$) and $\theta$ (P$_i$ − C4'$_i$ − − P$_{i+1}$ − C4'$_{i+1}$).[2] The ($\eta,\theta$) strategy has been shown to be a useful means of classifying small structural motifs, such as triloops.[1] A more general attempt to correlate the measured $\eta$–$\theta$ parameters to a single-point, AMBER force-field conformational energies of all the nucleotides in the database was undertaken, but no meaningful relationship was found.[8] Herein, the question of how our previous conformational study[1] of some hairpin triloops (Fig. 1) is lined up with their molecular dynamics (MD) is addressed.

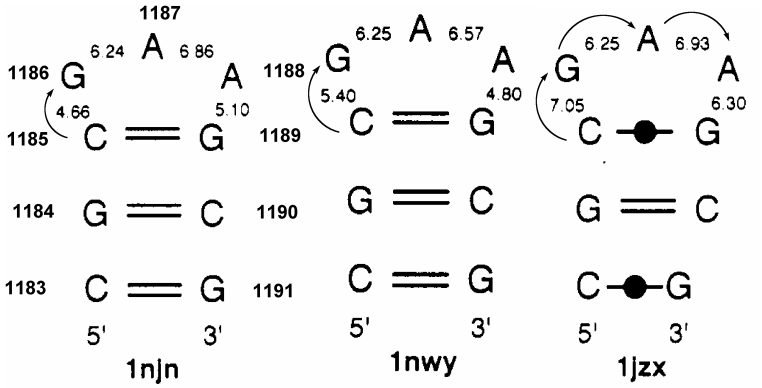


Fig. 1. Two-dimensional representations of the triloop tertiary structures in accordance with the geometric nomenclature of Leontis and Westhof.[9] The symbols are: = – GC *cis* canonical Watson–Crick base pair, –●– – *cis* Watson–Crick/Watson–Crick edge-to-edge basepair, and → – change in strand orientation. The numbers denote the phosphate···phosphate distances in angstroms (Å).

## RESULTS AND DISCUSSION

To investigate the conformational differences between the cGAAg (1185– –1189) motifs in the large ribonucleoligand complexes 1njn, 1nwy and 1jzx, with respect to that in the reference structure 1njp, the difference in nucleotide morphologies based on the values of the pseudotorsion angles, $\eta$ and $\theta$, for two RNA

worms of the same length was previously observed.[1] For a single nucleotide with sequence position *i*, the difference is given by

$$\Delta(\eta,\theta) \equiv \sqrt{(\eta_i^{\mathrm{A}} - \eta_i^{\mathrm{B}})^2 + (\theta_i^{\mathrm{A}} - \theta_i^{\mathrm{B}})^2} \quad (1)$$

where A and B are the two structures being compared. Nucleotides with $\Delta(\eta,\theta) < 25°$ are considered to be structurally similar to each other, while those with $\Delta(\eta,\theta) > 25°$ are not.[6] For the particular motifs in 1njn, 1nwy and 1jzx, the average (av) values of $\Delta(\eta,\theta)$ were 1, 15 and 110°, while the average RMSDs involving all atoms were 0.05, 0.85 and 5.36 Å, respectively. Notably, a near linear relationship between the average RMSD and the average difference in the pseudotorsion angles $\Delta(\eta,\theta)$ was found.[1] In the present work, the trends associated with the structural features are complemented with the dynamics of these motifs.

All the optimization procedures and MD simulations were performed by the Hyperchem molecular modeling system for Windows.[10] As the starting geometries were far from minimum, steepest descent optimizations of the motif structures with an RMS gradient of 0.01 kcal $Å^{-1}$ $mol^{-1}$ were performed before the MD computations. Each optimized structure was subsequently placed in a periodic box of 30×30×30 $Å^3$ containing 892 water molecules associated with a minimum distance of 2.3 Å between solvent and solute atoms. The AMBER force field was chosen with the following options: dielectric (epsilon) = constant, scale factor = 1, 1−4 scale factors – electrostatic = 0.9, van der Waals = 0.9 and cutoffs = none. The MD procedure with several options was specified to simulate molecular movement so that it was possible to observe equilibrium properties and kinetic behavior. 50 picoseconds (1 ps = $1\times10^{-12}$ s) without changing the simulation temperature were chosen as a run time. A time interval of 0.002 ps between evaluations of the total energy and temperature of the system was chosen as the step size. At the start of the run time, atomic velocities are adjusted to give a simulation temperature of 300 K. To stabilize the temperature during the run time, constant temperature simulations with a bath relaxation time of 0.5 ps were performed. In this context, the average kinetic, potential and total energies of the motifs in both the complexes and the free form of RNA (reference structure) were observed. The plots showing the relative, total and potential energies of the motifs in the complexes with respect to that in the reference structure are depicted in Fig. 2. The relative potential energies indicate that the stability order, from the highest to the lowest, of the motifs is: 1njn, 1nwy and 1 jzx. By adding the kinetic energies, the same trend displayed by the "relative total energy *vs.* time" plot is quite clear.

Since sugar puckers and torsion angles are unknown in the 2.5–3 Å resolution range, which is typical for large nucleic acids, it was therefore difficult to study most of the recurrent motifs, such as sharp turns, U-turn, *etc.*[11] A conformational strategy rooted in the pseudotorsion $(\eta,\theta)$ approach was proposed to be

a possible way to bypass the difficulties for small constitutive parts of large RNAs.[1] The agreement between the trends of conformational parameters recently reported[1] and the trends of the MD energies reported herein speaks in favor of the previous proposal.

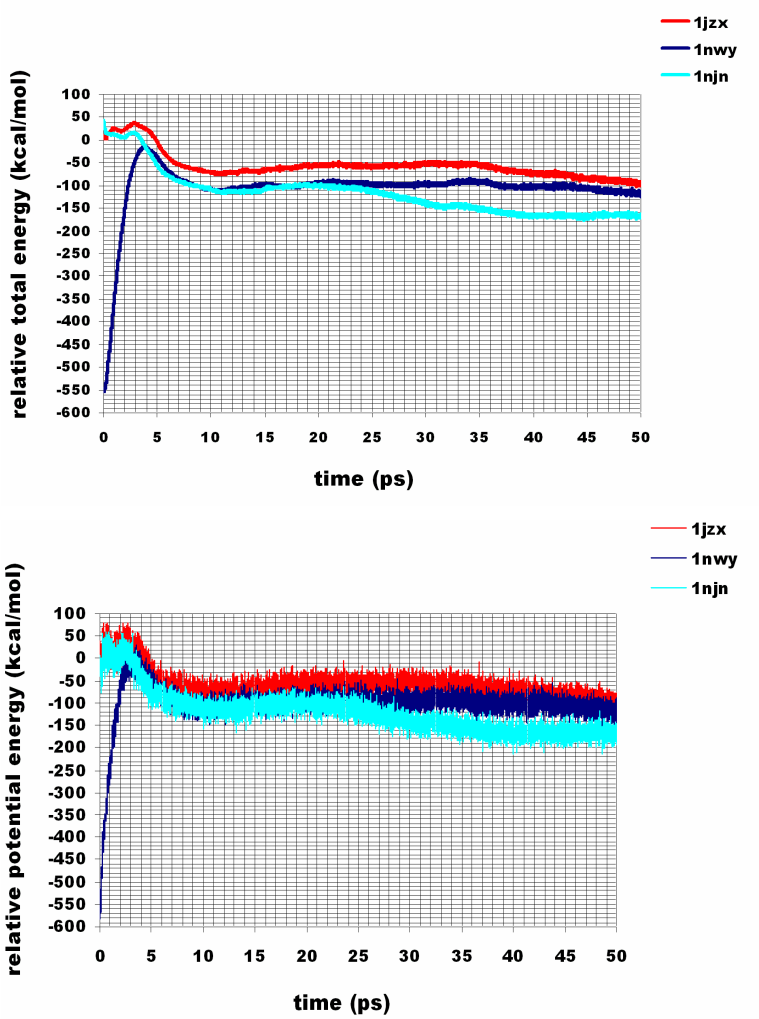


Fig. 2. Relative total and potential energies of the cGAAg (1185–1189) motifs in the complexes (PDB IDs: 1njn, 1nwy, 1jzx ) with respect to that in the unbound form of rRNA (PDB ID: 1njp).

The interaction motifs of various hairpin loops were hypothesized as possible targets for the binding of proteins.[12] The indications were primarily related to the extent of loop flexibility. Consequently, the investigations were presumably true for loops having a larger number of nucleotides, such as 4, 5, *etc*. As the local behavior of hairpin triloops was not quite clear, the structural features

induced by the binding of ligands of a number of triloops in rRNA were investigated.[1] In this context, all RNA residues in contact with the ligands and all RNA regions experiencing considerable conformational changes upon ligand binding were identified. As the bound complexes are conceivable as ribosomal states at various stages of translation, the ligands were found to be far (in the range of 20 Å) away from the triloops, interacting primarily with other parts of the ribosome.[1] For the complexes under study, 1njn, 1nwy and 1jzx, the RNA residues with the highest values of $\Delta(\eta,\theta)$ in contact with the ligands are A2581, A1354 and A764 respectively.[1] The "$\Delta(\eta,\theta)$ *vs.* sequence position" plot, taken in the immediate vicinity of the A2581, A1354 and A764 residues in the complexes, shows their corresponding $\Delta(\eta,\theta)$ values to be 232.1, 45.8 and 47.1°, respectively (Figs. 3–5). The particular binding sites can be viewed as the maximum-entropy sites involved in bonding. There is a more intuitive understanding that conformational changes within various localized regions along a large biological macromolecule are a direct consequence of the overall response of the macromolecular structure to the binding of a ligand. Thus, it is quite interesting to gain more insight into what is the impact of the binding of ligands, manifested by the maximum-$\Delta(\eta,\theta)$ sites A2581, A1354 and A764 in the large ribonucleoligand complexes 1njn, 1nwy and 1 jzx, on the localized behavior of the cGAAg (1185––1189) motifs.

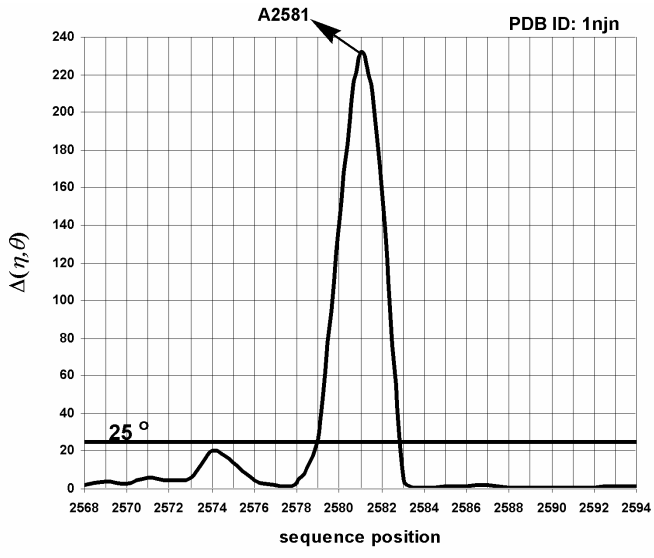


Fig. 3. $\Delta(\eta,\theta)$ *vs.* sequence position in the immediate vicinity of the ligand binding site A2581 having a maximum value of 232.1° among all of the RNA residues in contact with the ligand. The line at 25° indicates a threshold above which nucleotides in the complexes are considered to have different conformations relative to those in the reference structure (PDB ID:1njp).

There is some controversy in the literature on key factors dictating RNA–ligand recognition. The first major aspect is that the nature of RNA–ligand interactions is considered as a determinative factor influencing ligand specificity. Thus, the structural variability of RNA, as well as the ability of the RNA mole-

cule to distort upon ligand binding may play a crucial role in RNA–ligand interactions.[13] The second major aspect is related to the sequence-specific binding of RNA.[14] The previously raised question is hereafter addressed in light of these two main standpoints.

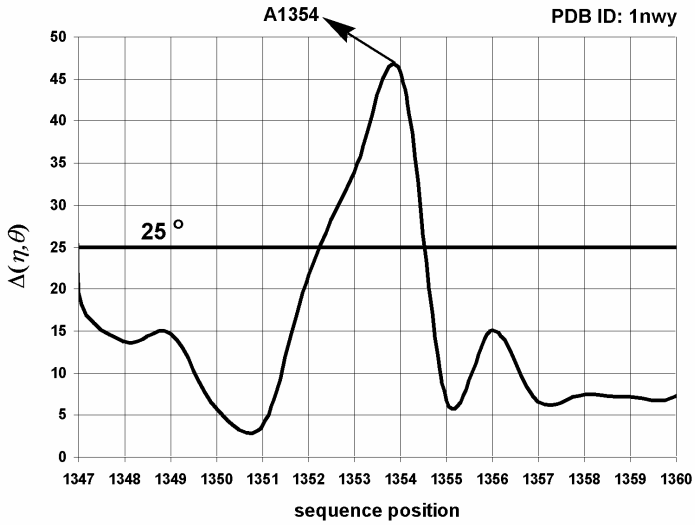


Fig. 4. $\Delta(\eta,\theta)$ *vs.* sequence position in the immediate vicinity of the ligand binding site A1354 having a maximum value of 45.8° among all of the RNA residues in contact with the ligand.

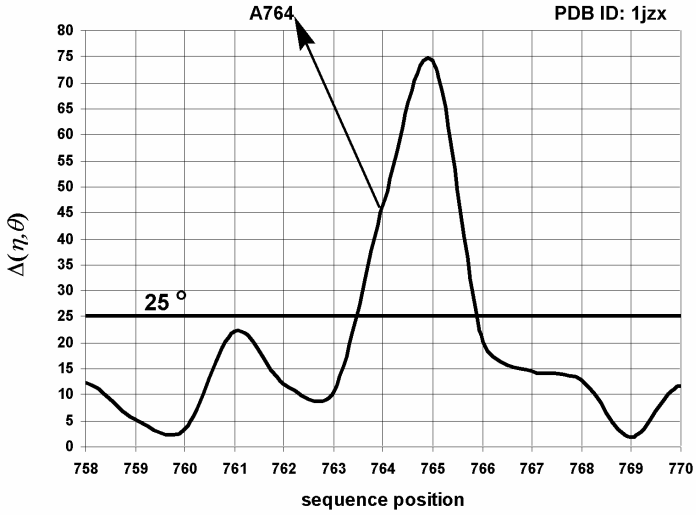


Fig. 5. $\Delta(\eta,\theta)$ *vs.* sequence position in the immediate vicinity of the ligand binding site A764 having a maximum value of 47.1° among all of the RNA residues in contact with the ligand.

In the context of the first aspect, the RNA–ligand binding sites and the nature of particular contacts in the complexes 1njn, 1nwy and 1jzx were identified

by the ENTANGLE program.[15] In general, no hydrogen bonds, or electrostatic and stacking interactions were detected. In 1njn, 4 hydrophobic contacts, having an average bond length of 4.70 Å, were found between atoms of the A2581 residue and atoms of the ligand. In 1nwy, atoms of the A1354 residue make 5 hydrophobic contacts with atoms of the ligand, having an average bond length of 4.51 Å. In 1jzx, atoms of the A764 residue participate in 6 hydrophobic contacts with atoms of the ligand, having an average bond length of 4.17 Å. Hence, 4, 5 and 6 hydrophobic contacts in the complexes are associated with average bond lengths of 4.70, 4.51 and 4.17 Å, respectively. To our chemical perception, the larger the number of contacts is, the smaller an average bond length of the contacts is, and the larger $\Delta(\eta,\theta)$ for a particular ligand binding site is. If the ability of RNA to deform upon ligand binding is, quantitatively, conceivable through the values of $\Delta(\eta,\theta)$ of 232.1, 45.8 and 47.1° for A2581, A1354 and A764, respectively, we note that the trends both of the number of hydrophobic contacts and of their average bond lengths do not agree with the trend of $\Delta(\eta,\theta)$ values. Note also the average values of $\Delta(\eta,\theta)$ for 15- and 21- and 27-nucleotide sequences around the A2581, A1354 and A764 sites, which are placed right in the middle of the sequences. For 15-nucleotide sequences, the average values of $\Delta(\eta,\theta)$ are 40.6, 14.9 and 17.7°, respectively. For 21-nucleotide sequences, the average values of $\Delta(\eta,\theta)$ are 29.8, 29.4 and 16.2°, respectively. For 27-nucleotide sequences, the average values of $\Delta(\eta,\theta)$ are 23.6, 24.1 and 34.7°, respectively. Therefore, a common chemical intuition based upon the nature of contacts of the A2581, A1354 and A764 residues only conforms to the case of 27-nucleotide sequences. Moving away from the particular binding sites, noteworthy are the average values of $\Delta(\eta,\theta)$ of 1, 15 and 110° for the cGAAg (1185–1189) motifs in the complexes 1njn, 1nwy and 1jzx, respectively. Clearly, the nature of contacts of the A2581, A1354 and A764 residues is in agreement with the trends both of $\Delta(\eta,\theta)$ values and of MD energies for small cGAAg (1185–1189) motifs being both about 20 Å away from the specific ligand binding sites and involved in interactions with other parts of the ribosome.

A simple measure for the determination of the strain of a triloop (Å), such as:

$$\frac{1}{4}\sum_{k=1}^{i+3}\left|P_kP_{k+1}-5.9\right| \qquad (2)$$

was previously introduced.[1] While $P_kP_{k+1}$ is the phosphate···phosphate distance between two consecutive nucleotides, $k$ and $k$+1, 5.9 Å stands for the phosphate···phosphate distance of the C3'-*endo* conformation.[16] Interestingly, the trend of the strains, 0.82, 0.66 and 0.73 Å, of the cGAAg (1185–1189) motifs in the 1njn, 1nwy and 1jzx complexes, respectively, does not agree with the chemical elucidation of the binding of ligands, which is primarily manifested through the trend of the average bond lengths, 4.70, 4.51 and 4.17 Å, of the A2581, A1354 and A764 contacts, respectively.

In the context of the second aspect, to probe the sequence-specific binding of RNA, nucleotide sequences containing 15, 21 and 27 nucleotides in the immediate vicinity of the maximum-$\Delta(\eta,\theta)$ ligand binding sites, A2581, A1354 and A764, were chosen as the input required to generate the corresponding secondary structures. The particular binding sites were initially placed right in the middle of the sequences, so that 7, 10 and 13 nucleotides were on each side of A2581, A1354 and A764, giving total sequence lengths of 15, 21 and 27 nucleotides. No restrictions were imposed on the process of generating the secondary structures by means of the Vienna RNA package V1.1.[17] The G–U pairing, based on the base pair (BP) probability algorithm of McCaskill,[18] was allowed in terms of the G–U wobble BPs.[9,19] Energy parameters were taken from the literature.[20–22] The secondary structure coordinates were calculated with Naview[23] within the Vienna RNA package,[17] while the employed dynamic programming algorithm was that of Zuker and Stiegler.[24] The calculated secondary structures for 15-nucleotide sequences are shown schematically in Fig. 6, while those corresponding to the 21- and 27-nucleotide sequences are given in the Supplementary Material, due to insufficient space in the present article. Note that the positions of A2581, A1354 and A764 are within various loops in Fig. 6, as generally expected for RNA residues in contact with ligands.

Base pairing defined by the secondary structures, consequently, was essential information for the determination of the thermodynamic parameters using the two-state conformational model of RNA sequences, as implemented within the framework of the Mfold V3.2 web server.[25,26] The very basic idea of a two-state model is that hairpin formation and more complex secondary structures of nucleic acids can be described in terms of rate of formation, stability, and control of secondary structure. The two states, ordered and disordered structures, are connected by a melting curve having a characteristic sigmoid shape. At low temperatures, all base pairs are formed, while at high temperatures no base pairs are formed. At any intermediate temperature, both the free energy of base pair formation and the nature of not fully paired intermediates influence the fraction of unpaired bases. At the melting temperature, $T_m$, depending solely on the free energy of base pair formation and not on the intermediates, paired and unpaired bases are present equally. Since enthalpy ($\Delta H$) and entropy ($\Delta S$) can be computed from the melting curve, it is straightforward to calculate $\Delta H$ and $\Delta S$ if no presence of the intermediates is assumed.[27] The core algorithm of the Mfold software package predicts a minimum free energy, as well as free energies for foldings containing desired base pairs. The minimum folding energy of a sequence was calculated by the zipfold server. The '$T_m$' server was employed to estimate two-state melting temperature. Only available RNA folding parameters, version 2.3, were used to calculate the enthalpy of this folding using the appropriate nearest neighbor parameters. The enthalpy calculations were followed by the estimation of $\Delta S$ and $T_m$ using a 2-state model as discussed above.[25]

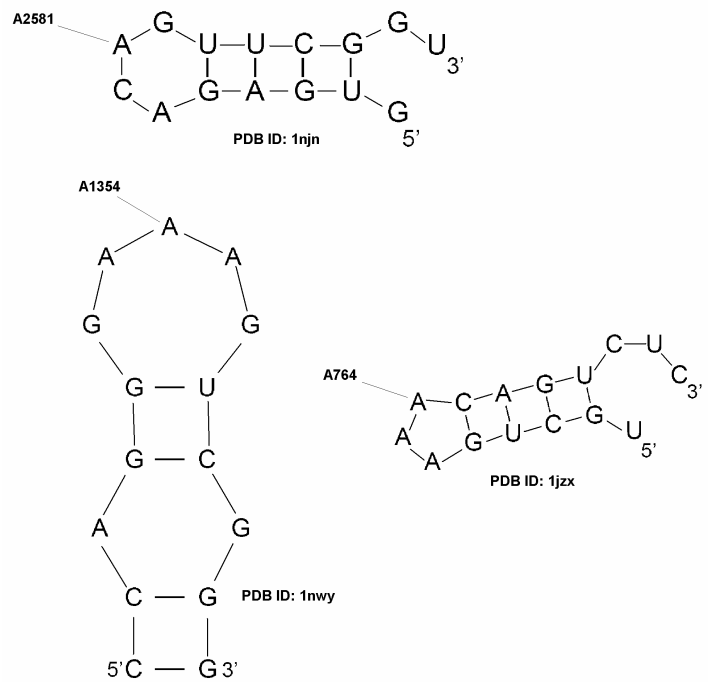


Fig. 6. Secondary structures generated by the RNAdraw program[17] for 15-nucleotide sequences in the immediate vicinity of the maximum-$\Delta(\eta,\theta)$ ligand binding sites, denoted by A2581, A1354, and A764. Secondary structures for sequences having 21 and 27 nucleotides around the same ligand binding sites in the complexes are given in the Supplementary Material due to insufficient space in the present paper.

The calculated values of these parameters for the sequences of various lengths are given in Table I. The trend of the $\Delta G$ values, −2.9, −1.1 and −3.2 kcal mol$^{-1}$, for the 15-nucleotide sequences does not agree with that of the average values of $\Delta(\eta,\theta)$ of 1, 15 and 110° for the cGAAg (1185–1189) motifs in the complexes 1njn, 1nwy and 1jzx, respectively. However the trends of the $\Delta G$ values for both the 21- and 27-nucleotide sequences, −7.7, −5.1 and −4.8 kcal mol$^{-1}$ and −9.2, −5.5 and −5.1 kcal mol$^{-1}$ are in agreement with that of $\Delta(\eta,\theta)_{av}$ for the cGAAg (1185–1189) motifs in the complexes 1njn, 1nwy and 1jzx, respectively. Note that the trends of the $\Delta G$ values are in accordance with those of the $E_{ss}$ values for all of the sequences with the same number of nucleotides in the series of complexes. It is indicative that, by moving away from the ligand binding sites with the maximum value of $\Delta(\eta,\theta)$, the trends displayed by $\Delta G$ and $E_{ss}$ tend to be lined up with both those of the $\Delta(\eta,\theta)_{av}$ values for very distant cGAAg motifs and of the energies of the motif MD. To further probe this indication, the average energies of the secondary structures and the average $\Delta(\eta,\theta)$ for the sequences of various lengths are given in Table II. Clearly, only for the sequences of 27 nu-

cleotides do the $E_{\text{ss-av27}}$ and $\Delta(\eta,\theta)_{\text{av27}}$ values display trends that agree with those of the $\Delta(\eta,\theta)_{\text{av}}$ values and MD energies associated with the cGAAg (1185––1189) motifs.

TABLE I. Values of the thermodynamic variables, based on a 2 state model, for sequences of various lengths in the immediate vicinity of the maximum-$\Delta(\eta,\theta)$ ligand binding sites, A2581, A1354 and A764, in the complexes 1njn, 1nwy and 1jzx

| PDB ID (Sequence Range), Sequence Length<br>Sequence | $\Delta G$<br>kcal mol$^{-1}$ | $\Delta H$<br>kcal mol$^{-1}$ | $\Delta S$<br>cal kmol$^{-1}$ | $T_{\text{m}}$<br>°C | $E_{\text{ss}}$[a]<br>kcal |
|---|---|---|---|---|---|
| 1njn (2574–2588), 15<br>GUGAGAC(A2581)GUUCGGU | –2.9 | –30.2 | –91.5 | 56.6 | –1.3 |
| 1nwy (1347–1361), 15<br>CCAGGGA(A1354)AGUCGGG | –1.1 | –24.4 | –78.3 | 38.2 | –1.1 |
| 1jzx (757–771), 15<br>UGCUGAA(A764)CAGUCUC | –3.2 | –30.2 | –90.6 | 59.8 | –2.8 |
| 1njn (2571–2591), 21<br>GUCGUGAGAC(A2581)GUUCGGUCUC | –7.7 | –55.1 | –158.9 | 73.5 | –6.7 |
| 1nwy (1344–1364), 21<br>CGCCCAGGGA(A1354)AGUCGGGACC | –5.1 | –52.0 | –157.4 | 57.0 | –4.3 |
| 1jzx (754–774), 21<br>GCCUGCUGAA(A764)CAGUCUCGGA | –4.8 | –59.6 | –183.5 | 51.5 | –3.5 |
| 1njn (2568–2594), 27<br>AACGUCGUGAGAC(A2581)GUUCGGUCUCUAU | –9.2 | –62.6 | –179.2 | 76.1 | –7.9 |
| 1nwy (1341–1367), 27<br>GUCCGCCCAGGGA(A1354)AGUCGGGACCUAA | –5.5 | –49.2 | –146.7 | 62.2 | –5.1 |
| 1jzx (751–777), 27<br>GGUGCCUGCUGAA(A764)CAGUCUCGGAUGA | –5.1 | –76.7 | –240.2 | 46.1 | –3.7 |

[a]Energy of the secondary structure (ss) calculated by the Vienna RNA package V1.1.[17]

TABLE II. Values of both the average (av) energies of the secondary structures ($E_{\text{ss-av}}$) and of the average $\Delta(\eta,\theta)$ for sequences of various lengths in the immediate vicinity of the maximum-$\Delta(\eta,\theta)$ ligand binding sites, A2581, A1354 and A764, in the complexes 1njn, 1nwy and 1jzx

| $E_{\text{ss-av}_{\text{sequence length}}}$ / kcal<br>$\Delta(\eta,\theta)_{\text{av}_{\text{sequence length}}}$ / ° | PDB ID: 1njn | PDB ID: 1nwy | PDB ID: 1jzx |
|---|---|---|---|
| $E_{\text{ss-av}_{15}}$ | –0.08 | –0.07 | –0.19 |
| $\Delta(\eta,\theta)_{\text{av}_{15}}$ | 40.57 | 14.90 | 17.74 |
| $E_{\text{ss-av}_{21}}$ | –0.32 | –0.21 | –0.17 |
| $\Delta(\eta,\theta)_{\text{av}_{21}}$ | 29.87 | 29.38 | 16.21 |
| $E_{\text{ss-av}_{27}}$ | –0.29 | –0.19 | –0.14 |
| $\Delta(\eta,\theta)_{\text{av}_{27}}$ | 23.66 | 24.11 | 34.73 |

The three nucleotide sequences of various lengths centered on the maximum-$\Delta(\eta,\theta)$ ligand binding sites, A2581, A1354 and A764, are essentially three distinct structural motifs in each of the complexes, if observed from a structure––function standpoint. Consequently, their thermodynamic variables and energies

change in different ways, as previously discussed. In every single complex, it is useful to find an average measure as a representative characteristic for the three motifs of 15, 21 and 27 nucleotides. Based upon the values of $\Delta G$ and $E_{SS}$ in Table I for three sequences in each complex, the calculated average $\Delta G$ values are −6.6, −3.9 and −4.4 kcal mol$^{-1}$, while the average $E_{SS}$ values are −0.23, −0.15 and −0.17 kcal in the 1njn, 1nwy and 1jzx complexes, respectively. Interestingly, the trends of $\Delta G$ and $E_{SS}$ are in line with that of the cGAAg (1185–1189) motif strain, 0.82, 0.66 and 0.73 Å in 1njn, 1nwy and 1jzx, respectively. This is in contrast to the finding that the values of the strains of triloops do not follow the trend of the average bond lengths, 4.70, 4.51 and 4.17 Å, of the A2581, A1354 and A764 contacts, respectively, as previously discussed in the context of the first aspect of RNA–ligand recognition. Therefore, the nature of RNA–ligand contacts is presumably determined by the types of ligands involved in bonding, which are the antibiotics, sparsomycin, azithromycin and clindamycin in the 1njn, 1nwy and 1jzx complexes, respectively.

## CONCLUSIONS

The considerations are well-correlated with the understanding that conformational changes, induced within localized regions of an rRNA structure, are associated with the overall response of the rRNA structure to the binding of a ligand at sites which are quite far (in the range of 20 Å) away from the localized regions. Due to the structural variability of RNA, the overall response is conceivable as the RNA capability of distorting upon ligand binding.

## SUPPLEMENTARY MATERIAL

Secondary structures generated by the RNAdraw program[17] for 21- and 27-nucleotide sequences in the immediate vicinity of the maximum-$\Delta(\eta,\theta)$ ligand binding sites, denoted by A2581, A1354, and A764, in the 1njn, 1nwy and 1jzx complexes, respectively, are available electronically from http://www.shd.org.yu/JSCS/ or from the corresponding author on request.

*Acknowledgments.* This work was supported by the Projects 142025 (Aleksandra Rakić) and 143016B (Petar M. Mitrašinović) financed by the Ministry of Science of the Republic of Serbia.

## ИЗВОД

## ДИНАМИКА МАЛИХ СТРУКТУРНИХ МОТИВА У рРНК УСЛЕД ВЕЗИВАЊА ЛИГАНДА

АЛЕКСАНДРА РАКИЋ[1] и ПЕТАР М. МИТРАШИНОВИЋ[2]

*[1]Факултет за физичку хемију, Универзитет у Београду, Студентски трг 12–16, 11000 Београд и [2]Центар за мултидисциплинарне студије, Универзитет у Београду, Кнеза Вишеслава 1, 11030 Београд*

Тронуклеотидне петље GAA (1186–1188) затворене са спареним c–g базама у великим рибонуклеотидним комплексима (PDB кодови: 1njn, 1nwy, 1jzx) су анализиране у овом раду помоћу молекуларно-динамичких симулација. Трендови релативних енергија ових мотива у комплексима у односу на мотив у слободној (без лиганда) структури рРНК (PDB код: 1njp)

се поклапају са трендовима конформационих параметара базираних на псеудоторзионом ($\eta,\theta$) прилазу из претходног рада.[1] Идентификоване су области структуре рРНК које се налазе у непосредној близини контаката са нејизраженијим конформационим променама при везивању лиганда. Одређени су термодинамички параметри базирани на конформацијском моделу "два стања" секвенци рРНК са 15, 21 и 27 нуклеотида око ових везивних места лиганада. Са више структурног становишта, деформација тронуклеотидне петље, која је далеко од ових везивних места и укључена у интеракције са осталим деловима рибозома, установљена је као структурна особина која одговара трендовима просечних термодинмичких параметара за три мотива дефинисана секвенцијама од 15, 21 и 27 нуклеотида. Са више функционалног становишта, типови лиганада у комплексима су предложени као важан фактор који детерминише рРНК–лиганд препознавање.

(Примљено 18. јануара 2007)

## REFERENCES


1. A. Rakić, P. M. Mitrašinović, in *Proceedings of the 8th International Conference on Fundamental and Applied Aspects of Physical Chemistry*. A. Antić–Jovanović, S. Anić, Eds., Society of Physical Chemists of Serbia, Belgrade, 2006, p. 362
2. C. M. Duarte, A. M. Pyle, *J. Mol. Biol.* **284** (1998) 1465
3. T. H. Reijmers, R. Wehrens, L. M. Buydens, *J. Chem. Inf. Comput. Sci.* **41** (2001) 1388
4. E. Hershkovitz, E. Tannenbaum, S. B. Howerton, A. Sheth, A. Tannenbaum, L. D. Williams, *Nucleic Acids Res.* **31** (2003) 6249
5. P. Gendron, S. Lemieux, F. Major, *J. Mol. Biol.* **308** (2001) 919
6. C. M. Duarte, L. M. Wadley, A. M. Pyle, *Nucleic Acids Res.* **31** (2003) 4755
7. W. K. Olson, *Biopolymers* **15** (1976) 859
8. S. J. Weiner, P. A. Kollman, D. T. Nguyen, D. A. Case, *J. Comput. Chem.* **7** (1986) 230
9. N. B. Leontis, E. Westhof, *RNA* **7** (2001) 499
10. Hypercube, Inc., *Hyperchem Molecular Modeling System*, release 5.02 for Windows 95/NT, http://www.hyper.com, Gainesville, FL, 1997
11. I. W. Davis, L. W. Murray, J. S. Richardson, D. C. Richardson, *Nucleic Acids Res.* **32** (2004) W615
12. J. C. Darnell, C. E. Fraser, O. Mostovetsky, G. Stefani, T. A. Jones, S. R. Eddy, R. B. Darnell, *Genes & Dev.* **19** (2005) 903
13. K. Nagai, *Mol. Biol. Rep.* **18** (1993) 105
14. H. E. Johansson, D. Dertinger, K. A. LeCuyer, L. S. Behlen, C. H. Greef, O. C. Uhlenbeck, *Proc. Natl. Acad. Sci. USA* **95** (1998) 9244
15. J. Allers, Y. Shamoo, *J. Mol. Biol.* **311** (2001) 75
16. W. Saenger, *Principles of Nucleic Acid Structure*, 1st Ed., Springer Verlag, New York, 1984, p. 221
17. I. L. Hofacker, W. Fontana, P. F. Stadler, L. S. Bonhoeffer, M. Tacker, P. Schuster, *Monats. Chem.* **125** (1994) 167
18. J. S. McCaskill, *Biopolymers* **29** (1990) 1105
19. N. B. Leontis, E. Westhof, *Curr. Opin. Struc. Biol.* **13** (2003) 300
20. D. H. Turner, N. Sugimoto, S. M. Freier, *Annu. Rev. Biophys. Chem.* **17** (1988) 167
21. S. M. Freier, R. Kiezerk, J. A. Jaeger, N. Sugimoto, M. H. Caruthers, T. Nelson, D. H. Turner, *Proc. Nat. Acad. Sci. USA* **83** (1986) 9373
22. J. A. Jaeger, D. H. Turner, M. Zuker, *Proc. Natl. Acad. Sci. USA* **86** (1989) 7706
23. R. Bruccoleri, G. Heinrich, *CABIOS* **4** (1988) 167

24. M. Zuker, P. Stiegler, *Nucleic Acids Res.* **9** (1981) 133
25. M. Zuker, *Nucleic Acids Res.* **31** (2003) 3406
26. D. H. Mathews, J. Sabina, M. Zuker, D. H. Turner, *J. Mol. Biol.* **288** (1999) 911
27. M. Levitt, in *Polymerization in Biological Systems, Ciba Foundation Symposium 7 (new series)*, ASP (Elsevier Excerpta Medica North-Holland), Amsterdam, 1972, p. 147.

Journal of the Serbian Chemical Society
JSCS@tmf.bg.ac.yu • www.shd.org.yu/JSCS
*J. Serb. Chem. Soc.* *73* (1) 55–64 (2008)
*JSCS–3687*
UDC 546.881–31+546.77–31+547.214:544.4
*Original scientific paper*

# Selective oxidation of isobutane on V–Mo–O mixed oxide catalysts

GHEORGHITA MITRAN[1]*, IOAN–CEZAR MARCU[1], TATIANA YUZHAKOVA[2] and IOAN SANDULESCU[1]

[1]*Department of Chemical Technology and Catalysis, University of Bucharest, 4-12, Blv. Regina Elisabeta, 030018, Bucharest, Romania and* [2]*Department of Environmental Engineering and Chemical Technology, Faculty of Engineering, Pannon University, 10 Egyetem St., H-8201, Veszprém, Hungary*

(Received 30 November 2006, revised 4 September 2007)

*Abstract*: Four V–Mo–O mixed metal oxides were prepared, characterized and tested for the selective oxidation of isobutane in the temperature range 350–550 °C, at atmospheric pressure. Isobutane was mainly oxidized to *iso*-butene and carbon oxides. The systems with low vanadium contents showed low activities but high isobutene selectivities, while the systems with high vanadium contents showed high activities with high carbon oxides selectivities. The effects of temperature, contact time and the molar ratio *iso*-butane to oxygen on the conversion of isobutane and the selectivity of the oxidation were studied.

*Keywords*: vanadium molybdenum oxides; *iso*-butane oxidation; *iso*-butene.

## INTRODUCTION

Selective oxidation of light alkanes is one of the most challenging topics for study because of the difficulty in stopping the oxidation at intermediate stages corresponding to olefin or oxygenates formation.

The development of more active and selective catalysts for the partial oxidation of alkanes has been extensively pursued in both industrial and academic research.[1,2]

In the literature,[3–8] several catalysts with different contents of $V_2O_5$ and $MoO_3$ have been studied for the selective oxidation of isobutane in order to determine the catalytically active phases. Thus, different oxide species were reported to be part of the active phase system in these catalysts. Andrushkevich[3] revealed $MoO_3$ and $V_2O_4$ as the major components of V–Mo–O catalysts and reported that the catalytic activity is related to the content of $V^{4+}$. Tichy *et al.*[4] identified $VMo_3O_{11}$, whereas Werner *et al.*[5] proposed $VMo_4O_{14}$ as the active phase. Both mixed oxides build layered structures, belonging to shear structures.

* Corresponding author. E-mail: mitran.gheorghita@unibuc.ro
doi: 10.2298/JSC0801055M

Werner *et al.*[5] explained that these structures are able to integrate and remove oxygen by a transition from corner-linked octahedra into edge sharing regions.

A key aspect towards the application of this type of catalysts is the exploration of how to control the operating conditions in order to maximize the catalytic performance (temperature, isobutane-to-oxygen molar ratio, hourly space volume velocity). It is commonly accepted that highly specific, local electronic structures of the active metal sites are essential for the catalytic performance.[9] The catalyst composition, as well as the conventional optimization of the microstructure by optimizing the synthesis procedure could result in further improvement of the catalytic performance. Hoang *et al.*[10] showed that alumina-supported vanadia exhibits low (15 %) selectivity to isobutene. An olefin selectivity of about 50 % was achieved at isobutane conversions of 10–15 % over vanadium-containing MCM-41 mesoporous catalysts.[11,12]

Good results for the oxidative dehydrogenation of isobutane were also obtained with heteropoly compounds[13–17] and pyrophosphates.[18,19]

The aim of this work was to study ways of enhancing the catalytic performance of V–Mo–O mixed oxide catalysts in the isobutane oxidation process, by adjusting the operating conditions and the catalyst composition. Thus, the influence of temperature, space velocity and feed composition on the catalytic performance of four V–Mo–O systems were investigated.

## EXPERIMENTAL

### *Preparation and characterization of the catalysts*

Mo–V–O-based catalysts, with the calculated compositions listed in Table I, were prepared from $(NH_4)_6Mo_7O_{24}{\cdot}4H_2O$ (99.8 %) and $NH_4VO_3$ precursors using the same method as reported by Ueda *et al.*[20]

The $(NH_4)_6Mo_7O_{24}{\cdot}4H_2O$ (99.8 %) and $NH_4VO_3$ precursors were dissolved seperately in distilled water and the $(NH_4)_6Mo_7O_{24}{\cdot}4H_2O$ solution was added to the $NH_4VO_3$ solution. For all the samples, the obtained mixture was heated at 90 °C to evaporate the water and then the remaining solid was dried at 120 °C for 15 h and calcined at 200 °C for 2 h, 400 °C for 2 h and 600 °C for 4 h, to obtain the final catalyst. For all the preparations, the same method and the same calcination temperatures were employed knowing that the preparation method and the calcination temperature influence the phase composition of Mo–V-oxides.[21-23]

The symbols used to denote the prepared catalysts are listed in Table I.

TABLE I. The calculated catalyst compositions and the symbols used

| Catalyst | Calculated catalyst composition |
|---|---|
| $C_1$ | 10 % $V_2O_5$–90 % $MoO_3$ |
| $C_2$ | 30 % $V_2O_5$–70 % $MoO_3$ |
| $C_3$ | 50 % $V_2O_5$–50 % $MoO_3$ |
| $C_4$ | 90 % $V_2O_5$–10 % $MoO_3$ |

The surface areas of the catalysts were measured from the adsorption isotherms of $N_2$ at 77 K using the BET method with an ASAP 2000 sorptometer. The crystal structures of the

samples were controlled by X-ray diffraction using a PW 3710 diffractometer with $CuK_\alpha$ radiation for Bragg's angles ($2\theta$) from 4 to 70°.

*Catalytic reactions*

The selective oxidation of isobutane was carried out in a fixed bed, quartz tube, down-flow reactor operating at atmospheric pressure. The internal diameter of the reactor tube was 20 mm. The catalyst was supported by quartz wool. Normally, 2 $cm^3$ (1.7 g) catalyst was used. The axial temperature profile was measured using a chromel–alumel thermocouple placed in a thermowell centered in the catalyst bed. The reactor temperature was controlled using a chromel–alumel thermocouple attached to the exterior of reactor. Quartz chips were used to fill the dead volumes below and above the catalyst bed to minimize potential gas-phase pyrolysis reactions at higher reaction temperatures. The reaction mixture, consisting of isobutane and air, was passed through the catalyst bed at a volume hourly space velocity (*VHSV*) of 1000–2500 $h^{-1}$. The influence of the isobutane to oxygen ratio was studied by varying this ratio in the range 0.5–2.0. The flow rates were controlled by fine needle valves and were measured using capillary flow meters. The catalyst was activated in air at 550 °C for 2 h before the reaction. Each run was carried out over a period of 3 h. In all studies, the reactor effluent passed through a condenser to remove water and liquid oxygenated products. The gas phase reactants and products were analysed as follows: a flame ionization detector and a GC- alumina column for the hydrocarbons and a thermal conductivity detector with a CTR-1 column for air, methane and carbon oxides. The condensate was analyzed with a Thermo Finnigan chromatograph using a DB-5 column and a flame ionization detector. Isobutene, CO, $CO_2$ were the major products formed under the employed reaction conditions; minor amounts of the liquid oxygenated products, acetic acid, methacrolein and unknowns were detected. The carbon balance was within 95–105 % for all of the reactions.

## RESULTS AND DISCUSSION

### *Catalysts characterization*

The XRD patterns of the prepared catalysts are shown in Fig. 1 and the observed phases are listed in Table II.

Examination of the powder diffraction patterns reveals the formation of multi-phase materials. Thus, in the 10 % $V_2O_5$–$MoO_3$ catalyst ($C_1$), three phases were observed, the $MoO_3$ phase being the predominant one. In the 30 % $V_2O_5$–$MoO_3$ catalyst ($C_2$), four phases were observed, the $V_2MoO_8$ phase being the predominant one. It should be noted that a $V_2O_5$ phase was not observed in these catalysts. In the catalyst with 50 % $V_2O_5$–$MoO_3$ ($C_3$), with four phases, the intensities corresponding to the $V_2MoO_8$ phase decreased and a $V_2O_5$ phase appeared. In the 90 % $V_2O_5$–$MoO_3$ ($C_4$) catalyst, with only two phases, the intensities of the $V_2O_5$ were the most dominant, while a $MoO_3$ phase was not observed.

The specific surface areas of the catalysts, obtained using the BET method, are presented in Table II. It can be observed that surface areas of all four catalysts were low, under 3 $m^2\ g^{-1}$.

### *Catalytic properties*

The four catalysts were tested in the selective oxidation of isobutane using an isobutane-to-oxygen ratio of 1. The conversion obtained and the distribution

of the products are listed in Table III. From the results shown in Table III, it can be seen that the $C_1$ and $C_2$ catalysts revealed a similar activity for the conversion of isobutane. The same behavior was observed for the $C_3$ and $C_4$ catalysts. The catalysts containing the $V_2O_5$ phase, namely $C_3$ and $C_4$, were more active but less selective for isobutene. In these cases, higher quantities of $CO_x$ were formed.

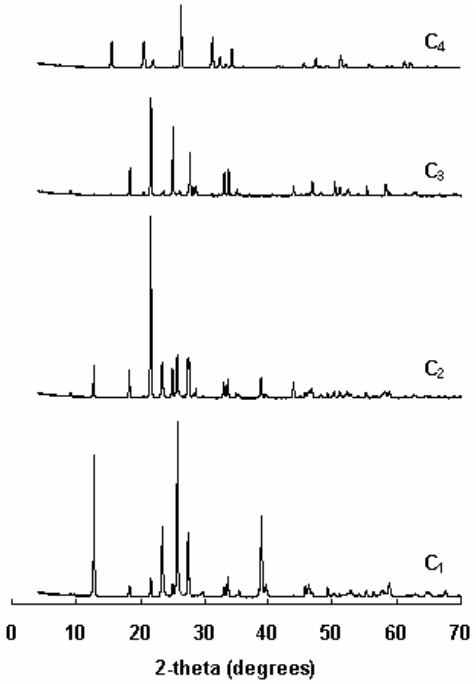


Fig. 1. X-Ray diffraction patterns of V–Mo mixed oxide catalysts.

TABLE II. The main crystalline phases determined by XRD and the specific surface areas of the V–Mo–O catalysts

| Catalyst | *SSA* / $m^2$ $g^{-1}$ | Crystalline phase identified | | | | |
|---|---|---|---|---|---|---|
| $C_1$ | 1.81 | $MoO_3$ | $V_2MoO_8$ | $VO_2$ | – | – |
| $C_2$ | 1.63 | $MoO_3$ | $V_2MoO_8$ | $VO_2$ | – | $Mo_6V_9O_{40}$ |
| $C_3$ | 0.94 | $MoO_3$ | $V_2MoO_8$ | $VO_2$ | $V_2O_5$ | – |
| $C_4$ | 2.66 | – | $V_2MoO_8$ | – | $V_2O_5$ | – |

The selectivity of conversion to *iso*-butene for the $C_1$ and $C_2$ catalysts was appreciably higher than that for the $C_3$ and $C_4$ catalysts and the main over oxidation products were CO and $CO_2$. Oxygenated compounds were detected in a fairly low amount with the $C_3$ and $C_4$ catalysts and only traces at higher temperatures were found with the $C_2$ catayst. These two different ranges observed for *iso*-butene selectivity are probably related to the prevalence of two different catalytic sites on the surface. The most selective catalysts ($C_1$ and $C_2$) have isobutene

selectivities that were about five times higher than the less selective one (the $C_3$ catalyst). Finally, it should be noted that cracking products were observed only with the $C_1$ catalyst and only at temperatures as high as 450 °C for space velocity of 2000 $h^{-1}$, or at temperatures higher than 490 °C with a space velocity of 2500 $h^{-1}$.

TABLE III. Catalytic performance of the V–Mo catalysts in the oxidation of isobutane (molar ratio *i*-$C_4H_{10}$:$O_2$ = 1:1)

| Catalyst | *VHSV*×$10^{-3}$ $h^{-1}$ | *t* / °C | Conversion, % | Selectivity, % | | | Rate[a] mol $kg^{-1}$ $h^{-1}$ |
|---|---|---|---|---|---|---|---|
| | | | *i*-$C_4H_{10}$ | *i*-$C_4H_8$ | Oxigenated compounds | $CO_x$ | |
| $C_1$ | 2.00 | 400 | 2.7 | 84.7 | – | 15.3 | 0.4 |
| | 2.00 | 450 | 5.2[b] | 65.9 | – | 21.1 | 0.9 |
| | 2.50 | 400 | 1.7 | 85.3 | – | 14.7 | 0.3 |
| | 2.50 | 450 | 3.2 | 85.4 | – | 14.6 | 0.6 |
| $C_2$ | 2.00 | 400 | 2.6 | 80.8 | – | 19.2 | 0.4 |
| | 2.00 | 450 | 3.2 | 62.9 | 11.6 | 25.5 | 0.5 |
| | 2.50 | 400 | 2.4 | 78.4 | – | 21.6 | 0.5 |
| | 2.50 | 450 | 2.9 | 57.0 | 2.4 | 40.6 | 0.6 |
| $C_3$ | 2.00 | 400 | 9.2 | 18.3 | 6.2 | 75.5 | 1.5 |
| | 2.00 | 450 | 13.9 | 21.4 | 4.2 | 74.4 | 2.3 |
| | 2.50 | 400 | 8.1 | 14.1 | 2.3 | 83.6 | 1.6 |
| | 2.50 | 450 | 11.3 | 16.2 | 2.1 | 81.7 | 2.3 |
| $C_4$ | 2.00 | 400 | 7.2 | 22.2 | 3.1 | 74.7 | 1.2 |
| | 2.00 | 450 | 9.6 | 25.4 | 2.1 | 72.5 | 1.6 |
| | 2.50 | 400 | 6.8 | 16.0 | 4.0 | 80.0 | 1.4 |
| | 2.50 | 450 | 8.5 | 38.2 | 2.6 | 59.2 | 1.7 |

[a]Reaction rate of isobutane; [b]selectivity to cracking products 13.1 %

The conversion of isobutane for the four catalysts as a function of reaction temperature is shown in Fig. 2. The conversion of *iso*-butane increased with increasing reaction temperature for all catalysts. The systems with a higher vanadium content ($C_3$ and $C_4$) were more active than the other two, over all the considered temperature range. Moreover, the $V_2O_5$ phase appeared only in these two catalytic systems and it is considered that this phase is responsible for the enhanced catalytic activity. No correlation was observed between the activity and the specific surface area of these catalysts.

The effect of the reaction temperature on the selectivities for *iso*-butene, $CO_x$ and oxygenated products is shown in Fig. 3. Isobutene selectivity decreased with the temperature on the $C_1$ and $C_2$ catalysts, while, interesting, it increased for the $C_3$ and $C_4$ catalysts with increasing temperature. The latter phenomenon was also observed by Pless *et al.*[24] in the oxidative dehydrogenation of propane at tempe-

ratures higher than 400 °C and was related to the complete depletion of $O_2$ from the reactant stream, *i.e.*, when depletion of $O_2$ in the reactant stream occurs and as the temperature increases, a more efficient utilization of oxygen is realized, leading to an increase in selectivity. In the present case, the oxygen is far from completely depleted (Table III) which means that other factors must also be considered for explaining this phenomenon. The oxidative dehydrogenation of *iso*-butane to isobutene is more important over the $C_1$ and $C_2$ catalysts which contain mainly $MoO_3$ and $V_2MoO_8$ phases and do not contain a $V_2O_5$ phase. The selectivity for $CO_x$ increased with increasing temperature on the $C_1$ and $C_2$ catalysts, while for the $C_3$ and $C_4$, the $CO_x$ selectivity decreased with increasing temperature. The oxygenate compounds were detected in a fairly low amounts with the $C_3$ and $C_4$ catalysts and only traces were evidenced at higher temperature with the $C_2$ catalyst.

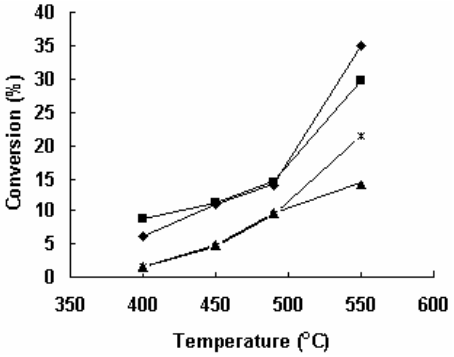


Fig. 2. Variation of the isobutane conversion with the reaction temperature over V–Mo–O catalysts (*VHSV* = 1500 $h^{-1}$, molar ratio *i*-$C_4H_{10}$:$O_2$ = 1:1); ✳ − $C_1$; ▲ − $C_2$;■ − $C_3$; ◆ − $C_4$.

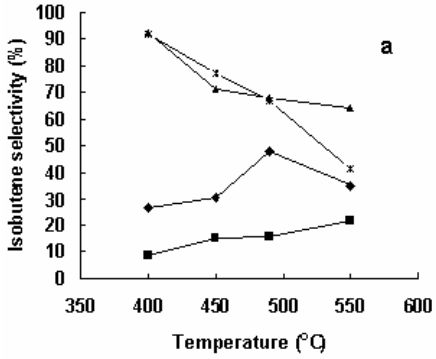


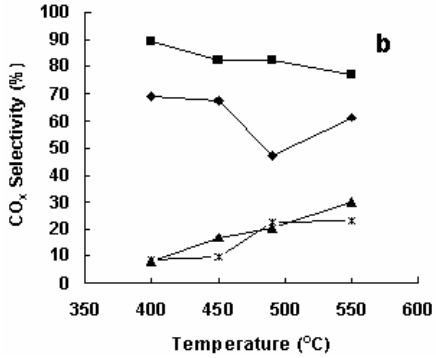


Fig. 3. Selectivity to: a) isobutene, b) $CO_x$ and c) oxygenated products as function of temperature (*VHSV* = 1500 $h^{-1}$, molar ratio *i*-$C_4H_{10}$:$O_2$ = 1:1); ✳ − $C_1$; ▲ − $C_2$; ■ −$C_3$; ◆ − $C_4$.

The variations of isobutane conversion and product selectivities as a function of the $i$-$C_4H_{10}$:$O_2$ molar ratio on the $C_1$ and $C_3$ catalysts at 400 °C are shown in Fig. 4. On the $C_1$ catalyst, the isobutane conversion was only slightly influenced by the $i$-$C_4H_{10}$:$O_2$ molar ratio and the isobutene selectivity passed through a maximum for the molar ratio 1:1. This maximum corresponds to a minimum of $CO_x$ selectivity. For the $C_3$ catalyst, the isobutane conversion decreased clearly with the $i$-$C_4H_{10}$:$O_2$ molar ratio and the isobutene selectivity increased reaching a plateau at a ratio of around one. The $CO_x$ selectivity decreased while the selectivity of oxygenates increased when the $i$-$C_4H_{10}$:$O_2$ molar ratio was increased. These results indicate that, with the $C_3$ catalyst, as the amount of oxygen was higher, the excess oxygen could oxidize a specific hydrocarbon species (adsorbed on the catalyst surface) to overoxidation products, such as CO and $CO_2$.

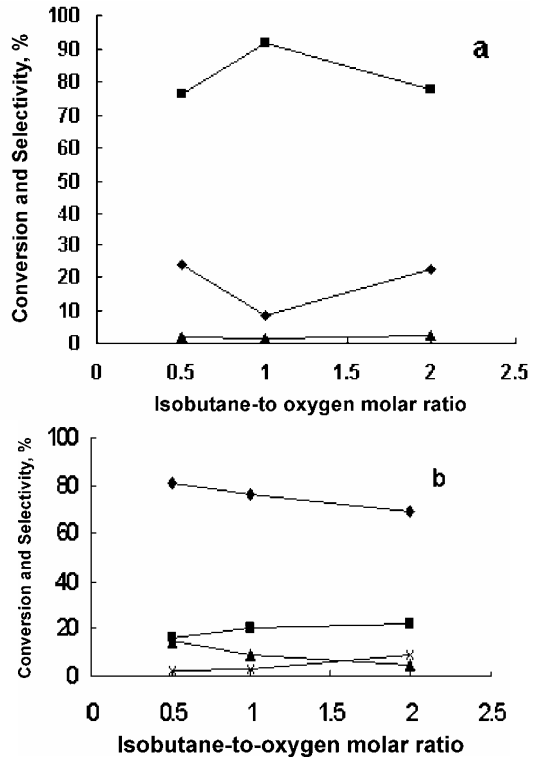


Fig. 4. Conversion of isobutane (▲) and selectivity to *iso*-butene (■), oxygenates (✳) and carbon oxides (◆) as function of $i$-$C_4H_{10}$:$O_2$ molar ratio over (a) $C_1$ catalyst and (b) $C_3$ catalyst at 400 °C, $VHSV$ = 1500 $h^{-1}$.

The influence of the contact time on the conversion of isobutane and the isobutene and $CO_x$ selectivities is shown in Fig. 5 for the $C_1$ catalyst at 450 °C. The conversion increased with increasing contact time, while the isobutene selectivity decreased. As expected, the operation at shorter contact time decreased the selectivity for overoxidation products and thus increased the selectivity to isobutene.

Finally, the apparent activation energies corresponding to the conversion of isobutane on the different catalysts under the same conditions (*VHSV* = 1500 $h^{-1}$; isobutane/oxygen = 1, $t$ = 350–550 °C) were calculated and Arrhenius plots obtained, presented in Fig. 6. The activation energies on the $C_1$ and $C_2$ catalysts were 79 and 67 kJ $mol^{-1}$, respectively. The activation energies on the $C_3$ and $C_4$ catalysts were 38 and 50 kJ $mol^{-1}$, respectively. It can be observed that the activation energies on the catalysts containing a $V_2O_5$ phase were lower than those measured on the catalysts without a $V_2O_5$. The lowest apparent activation energy was observed on the $C_3$ system, which contained both $V_2O_5$ and $MoO_3$ phases. All these values are comparable with those presented in the literature for the same reaction over vanadia based catalysts[25] and other oxide-based catalysts.[26]

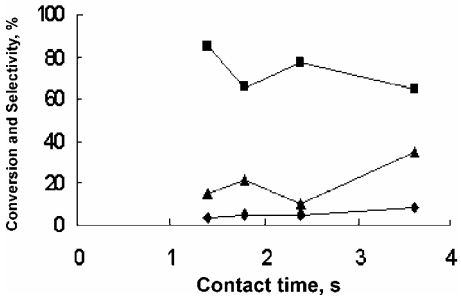


Fig. 5. Conversion of isobutane (◆) and selectivity to *iso*-butene (■) and $CO_x$ (▲) as function of contact time over $C_1$ catalyst at 450 °C (molar ratio *i*-$C_4H_{10}$:$O_2$ = 1:1).

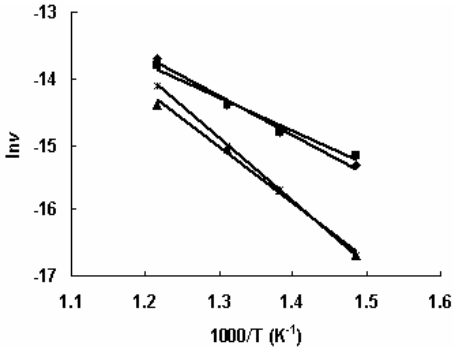


Fig. 6. Arrhenius plots for the conversion of isobutane on different catalysts: ✳ – $C_1$; ▲ – $C_2$; ■ – $C_3$; ◆ – $C_4$.

## CONCLUSIONS

Four Mo–V–O based catalysts were examined for the selective oxidation of isobutane. A relationship between the phase composition of the catalysts and their oxidation of isobutane activity was evidenced. No correlation was observed between the activity and the specific surface area of these catalysts. The activity of the four studied catalysts increased with increasing content of vanadium. The $C_3$ and $C_4$ catalysts, containing a $V_2O_5$ phase, were more active but less selective, while the $C_1$ and $C_2$ catalysts were less active but more selective to *iso*-butene. On the $C_3$ and $C_4$ catalysts, total oxidation products ($CO_x$) were predominately obtained.

The oxygenates (acetic acid and methacrolein) were detected in a fairly low amount with the $C_3$ and $C_4$ catalysts and for the $C_2$ catalyst, only at high temperatures.

The conversion of isobutane increased with increasing reaction temperature for all catalysts and the isobutene selectivity decreased with the temperature on the $C_1$ and $C_2$ catalysts, while, interesting, for the $C_3$ and $C_4$ catalysts, it increased

with increasing temperature. The *i*-$C_4H_{10}$-to-$O_2$ molar ratio was found to be optimum around a value of one. Operation at shorter contact time decreased the selectivity for the overoxidation products and thus increases the selectivity to isobutene.

The apparent activation energies for the transformation of isobutane were in the range 38−79 kJ mol$^{-1}$.

*Acknowledgements*. The authors are grateful to Dr. Éva Makó and Dr. Jozsef Kovacs for their expert technical assistance with the recording of the XRD spectra and the BET measurements, respectively. This research was supported by the National University Research Council (CNCSIS) under project No. 1064 A / 2006.

И З В О Д

## СЕЛЕКТИВНА ОКСИДАЦИЈА ИЗОБУТАНА НА V–Mo–O МЕШАНИМ ОКСИДНИМ КАТАЛИЗАТОРИМА

GHEORGHITA MITRAN[1], IOAN–CEZAR MARCU[1], TATIANA YUZHAKOVA[2] и IOAN SANDULESCU[1]

*[1]Department of Chemical Technology and Catalysis, University of Bucharest, 4-12, Blv. Regina Elisabeta, 030018, Bucharest, Romania и [2]Department of Environmental Engineering and Chemical Technology, Faculty of Engineering, Pannon University, 10 Egyetem St., H-8201, Veszprém, Hungary*

У реакцији селективне оксидације изобутана припремљена су и тестирана у интервалу температуре 350–550 °C на атмосферском притиску четири металоксидна катализатора V–Mo–O. Изобутан се претежно оксидује до изобутена и $CO_x$. Системи са малим садржајем ванадијума показују малу активност али високу селективност у настајању изобутена, док системи са високим садржајем ванадијума показују високу активност и високу селективност у добијању $CO_x$. Испитиван је такође утицај температуре, времена контакта и моларног односа изобутана према кисеонику на конверзију изобутана и оксидативну селективност.

(Примљено 30. новембра 2006, ревидирано 4. септембра 2007)

## REFERENCES

1. T. Ressler, O. Timpe, F. Girgsdies, J. Wienold, T. Neisius, *J. Catal.* **231** (2005) 279
2. Y. Takita, K. Kikutani, C. Xia, H. Takami, K. Nagaoka, *Appl. Catal. A* **283** (2005) 209
3. T. V. Andrushkevich, *Catal. Rev. Sci. Eng.* **35** (1993) 213
4. J. Tichy, J. Svachula, J. Farbotko, J. Goralski, T. Paryjcak, *Czech. Nauk. Politech. Lodz. Chem.* **616** (1991) 95
5. H. Werner, O. Timpe, D. Herein, Y. Uchid, N. Pfänder, U. Wild, R. Schlögl, *Catal. Lett.* **44** (1997) 153
6. J. S. Paul, P. A. Jacobs, P.-A. W. Weiss, W. F. Maier, *Appl. Catal. A* **265** (2004) 185
7. G. P. Schindler, C. Knapp, T. Ui, K. Nagai, *Top. Catal.* **22** (2003) 117
8. T. Shishido, A. Inoue, T. Konishi, I. Matsuura, K. Takehira, *Catal. Lett.* **68** (2000) 215
9. S. B. Abd Hamid, D. Othman, N. Abdullah, O. Timpe, S. Knobl, D. Niemeyer, J. Wagner, D. Su, R. Schlögl, *Top. Catal.* **24** (2003) 87
10. M. Hoang, J. F. Mathews, K. C. Pratt, *React. Kinet. Catal. Lett.* **61** (1997) 21
11. H. Jablonska, E. Wloch, Z. Olejniczak, B. Sulikowski, *Mol. Phys. Rep.* **29** (2000) 19
12. Q. Zang. Y. Wang, Y. Ohishi, T. Shishido, K. Takehira, *J. Catal.* **202** (2001) 308
13. J.S. Min, N. Mizuno, *Catal. Today* **66** (2001) 47
14. C. Knapp, T. Ui, K. Nagai, N. Mizuno, *Catal. Today* **71** (2001) 111
15. L. J. Duhamel, A. Monnier, Y. Barbaux, G. Hecquet, *Catal. Today* **32** (1996) 237

16. Q. Deng, S. Jiang, T. Cai, Z. Peng, Z. Fang, *J. Mol. Catal. A* **229** (2005) 165
17. F. Cavani, R. Mezzogori, A. Pigamo, F. Trifirò, *Chem. Eng. J.* **82** (2001) 33
18. I. C. Marcu, J. M. Millet, I. Sandulescu, *J. Serb. Chem. Soc*. **70** (2005) 791
19. I. C. Marcu, J. M. Millet, J. M. Herrmann, *Catal. Lett.* **78** (2002) 273
20. W. Ueda, D. Vitry, T. Katou, *Catal. Today* **99** (2005) 43
21. G. E. Selyutin, N. G. Maksimov, G. A. Zenkovets, D. V. Tarasova, V. F. Anufrienko, *React. Kinet. Catal. Lett.* **10** (1979) 25
22. T. P. Gorshkova, D. V. Tarasova, I. P. Olen'kova, G. N. Kustova, E. N. Yurchenko, T. A. Nikoro, *Kinet. Katal.* **25** (1984) 201
23. Z. Liu, Y. Li, S. Qi, K. Xie, N. Wu, Q.X. Bao, *Appl. Catal.* **56** (1989) 207
24. J. D. Pless, B. B. Bardin, H. S. Kim, D. Ko, M. T. Smith, R. R. Hammond, P. C. Stair, K. R. Poeppelmeier, *J. Catal.* **223** (2004) 419
25. V. Iannazzo, G. Neri, S. Galvagno, M. Di Serio, R. Tesser, E. Santacesaria, *Appl. Catal. A* **246** (2003) 49
26. R. Grabowski, B. Grzybowska, J. Sloczynski, K. Wcislo, Appl. *Catal. A* **144** (1996) 335.

Journal of the Serbian Chemical Society
JSCS@tmf.bg.ac.yu • www.shd.org.yu/JSCS
*J. Serb. Chem. Soc.* *73* (1) 65–71 (2008) UDC 541.182.45:544.112+519.233.2:546.86–31+546.86'18
*JSCS–3688* *Original scientific paper*

# Molecular parameters for the gas phase molecules SbO and SbP

P. SRI RAMACHANDRAN[1], V. RAJA[2] and N. RAJAMANICKAM[1]*

[1]*Physics Research Centre, V.H.N.S.N College, Virudhunagar – 626 001 and* [2]*Department of Physical Chemistry, Kalasalingam University, Krishnankoil – 626 190, India*

(Received 10 November 2006)

*Abstract*: Franck–Condon factors and *r*-centroids, which are very closely related to relative vibrational transition probabilities, were evaluated by the numerical integration procedure for the bands of the $A^2\Pi_{3/2} - X^2\Pi_{3/2}$, $C^2\Sigma - X^2\Pi_{3/2}$ and $D^2\Pi - X^2\Pi$ systems of the isotopic SbO molecule and for the $B^1\Pi - X^1\Sigma^+$ system of the isotopic SbP molecule, using a suitable potential.

*Keywords*: Franck–Condon factors; *r*-centroids and isotopic molecule SbO and SbP molecules.

## INTRODUCTION

Franck–Condon (F–C) factors are important parameters for every molecular band system, since they enter into the calculation of the relative band intensity, which is a significant source of information in quantitative spectroscopy, high-temperature chemistry, astrochemistry and cometary spectra. They are also important for the determination of the molecular structure, population of the vibrational levels in the upper electronic state involved in a transition, radiative lifetime, vibrational temperature and kinetics of energy transfer in stellar and other astrophysical atmospheres containing molecular species. On the other hand, knowledge of *r*-centroids has been found to be very useful in the discussion of the variation of the electronic transition moment with internuclear separation and in other molecular properties. Variation of *r*-centroids with band wavelengths (or wavenumbers) provides a useful bridge between experimental measurements, which are often expressed as a function of wavelength, and theoretical studies, which are often made in terms of internuclear separation.[1]

Suresh Kumar *et al.*[2] reported that the SbO molecule is likely to be present in the atmosphere of K-type stars and in interstellar space. Spectra of the radiation from astronomical sources show many bands which are attributed to diatomic molecules. A number of lighter as well as heavier diatomic molecules have been detected in stellar spectra, the Earth's atmosphere, planets and in interstellar

* Corresponding author. E-mail: nrmanickam@rediffmail.com
doi: 10.2298/JSC0801065R

sources. Dealing with 300 diatomic molecules of known or of possible astrophysical interest, Sauval and Tatum[3] also reported polynomial expressions of partition functions and equilibrium constants of the SbH, SbO, SbF and SbP molecules. Based on estimates of the abundances of Sb, the phosphate of antimony is expected to be present in stars. Estimates of the relative abundances of these metallic species are of importance for the understanding of the evolutionary phases of the observed stars and are also essential inputs in the modeling of the stellar atmospheres of late type stars. Their relative abundances in the interstellar medium give estimates of stellar activity, such as supernovae, in the observed region.

To the best of our knowledge, there has been no reports on Franck–Condon factors and r-centroids for the $A^2\Pi_{3/2} - X^2\Pi_{3/2}$ system of $^{123}$SbO, the $C^2\Sigma - X^2\Pi_{3/2}$ and $D^2\Pi - X^2\Pi$ systems of $^{121}$SbO and the $B^1\Pi - X^1\Sigma^+$ system of $^{123}$SbO and $^{121}$SbP molecules in the literature. Therefore, reliable values of the Franck–Condon factors and *r*-centroids for the above band systems of isotopic SbO and SbP molecules have been computed by a numerical integration procedure, using the suitable potential.

## FRANCK–CONDON FACTORS AND *r*-CENTROIDS

Mathematically, one can write for the intensity $I_{\nu'\nu''}$ of a molecular band for an electronic transition in emission ($\nu' \rightarrow \nu''$) as (Straughan and Walker[4]):

$$I_{\nu'\nu''} = DN_{\nu'}E^4_{\nu'\nu''}R^2_e(\bar{r}_{\nu'\nu''})q_{\nu'\nu''} \tag{1}$$

where $D$ is a constant, partly depending on the geometry of the apparatus; $N_{\nu'}$ denotes the number of molecules in the vibrational level $\nu'$ of the upper electronic state, determined by the Boltzmann law; $E_{\nu'\nu''}$ the energy quantum; $q_{\nu'\nu''}$ the Franck–Condon factor; $\bar{r}_{\nu'\nu''}$ the *r*-centroid and $R_e$ the electronic transition moment.

The intensities of bands in emission of diatomic molecular are controlled by the value of the Franck–Condon factor, which is the square of the overlap integral between the excited state wave function and the ground state wave function.

$$q_{\nu'\nu''} = \left|\langle \Psi_{\nu'} \mid \Psi_{\nu''} \rangle\right|^2 \tag{2}$$

where $\Psi_{\nu'}$ and $\Psi_{\nu''}$ are the vibrational wave functions for the upper and lower states, respectively, between which the transition occurs. The *r*-centroid is a unique value of the internuclear separation, which may be associated with the $\nu' - \nu''$ band and defined as:

$$\bar{r}_{\nu'\nu''} = \frac{\langle \Psi_{\nu'} \mid r \mid \Psi_{\nu''} \rangle}{\langle \Psi_{\nu'} \mid \Psi_{\nu''} \rangle} \tag{3}$$

For a proper understanding of the intensity distribution in the band systems of molecules, it is necessary to choose a suitable potential. The potential energy

curves for the appropriate electronic states of SbO, $^{123}$SbP and $^{121}$SbP have been constructed using the Morse[5] function and also by the Rydberg–Klein–Rees (RKR) procedure as modified by Vanderslice *et al.*[6,7] It was found that the Morse function represents the potential for the states of SbO, $^{123}$SbP and $^{121}$SbP quite adequately, since the experimental (RKR) curves are coincident with the Morse ones. The Morse wave functions were calculated at intervals of 0.01 Å for the range of $r$, respectively, from 1.66 to 2.22 Å, from 1.67 to 2.47 Å, from 1.70 to 2.27 Å, from 2.00 to 2.54 Å and from 2.00 to 2.54 Å for every observed vibrational level of the $A^2\Pi_{3/2} - X^2\Pi_{3/2}$ system of $^{123}$SbO, the $C^2\Sigma - X^2\Pi_{3/2}$ and $D^2\Pi - X^2\Pi$ systems of the $^{121}$SbO molecule and the $B^1\Pi - X^1\Sigma^+$ systems of the isotopic $^{123}$SbP and $^{123}$SbP molecules. The computation of the Franck–Condon factor was made by the Bates[8] method of numerical integration as per the detailed procedure provided by Partal Urena *et al.*[9] Integrals in the Eqs. (2) and (3) for the F–C factors ($q_{v'v''}$) and $r$-centroids ($\bar{r}_{v'v''}$) were computed numerically and the results are presented, respectively, in Tables I, II and III for the $A^2\Pi_{3/2}$ — $X^2\Pi_{3/2}$, $C^2\Sigma - X^2\Pi_{3/2}$ and $D^2\Pi - X^2\Pi$ systems of SbO and in Tables IV and V for the $B^1\Pi - X^1\Sigma^+$ system of the $^{123}$SbP and $^{121}$SbP molecules. The wavelengths ($\lambda_{v'v''}$) data[10–13] for the band systems of SbO, $^{123}$SbP and $^{121}$SbP molecules are also included in Tables I–V. The molecular constants used in the present study were collected from the compilation of Huber and Herzberg[14] and they are entered in Table VI.

TABLE I. Franck–Condon factors, $r$-centroids and wavelengths of the $A^2\Pi_{3/2} - X^2\Pi_{3/2}$ system of $^{123}$SbO

| | | $v''=0$ | $v''=1$ | $v''=2$ | $v''=3$ | $v''=4$ |
|---|---|---|---|---|---|---|
| $v'=0$ | $q_{v'v''}$ | 0.002 | 0.014 | 0.050 | 0.112 | 0.176 |
| | $\bar{r}_{v'v''}$ / Å | 1.923 | 1.943 | 1.964 | 1.985 | 2.007 |
| | $\lambda_{v'v''}$ / Å | – | – | 5952.52 | 6245.33 | 6564.71 |
| $v'=1$ | $q_{v'v''}$ | 0.010 | 0.053 | 0.119 | 0.142 | 0.081 |
| | $\bar{r}_{v'v''}$ / Å | 1.909 | 1.929 | 1.949 | 1.969 | 1.989 |
| | $\lambda_{v'v''}$ / Å | – | 5506.45 | 5758.92 | 6032.54 | – |
| $v'=2$ | $q_{v'v''}$ | 0.028 | 0.099 | 0.124 | 0.049 | 0 |
| | $\bar{r}_{v'v''}$ / Å | 1.895 | 1.914 | 1.934 | 1.952 | – |
| | $\lambda_{v'v''}$ / Å | – | 5341.82 | 5579.10 | – | – |

## RESULTS AND DISCUSSION

In the case of the $A^2\Pi_{3/2} - X^2\Pi_{3/2}$ system of the $^{123}$SbO and $C^2\Sigma - X^2\Pi_{3/2}$ systems of the $^{121}$SbO molecule, the F–C factors indicate that (0,3), (0,4), (1,2), (1,3) and (2,2), and (0,2), (0,3), (0,4), (1,1), (1,2), (2,0), (2,1), (3,0), (4,0), (5,0) and (6,0) bands are intense (F–C factor > 0.1). For the $D^2\Pi - X^2\Pi$ system, the F–C factors indicate that all the bands are less intense. Since $r_e' > r_e''$, the $r$-centroids values increase with increasing wavelength, which is expected in the red degraded band system.

TABLE II. Franck–Condon factors, *r*-centroids and wavelengths of the $C^2\Sigma - X^2\Pi_{3/2}$ system of 121SbO

| | | $v'' = 0$ | $v'' = 1$ | $v'' = 2$ | $v'' = 3$ | $v'' = 4$ |
|---|---|---|---|---|---|---|
| $v' = 0$ | $q_{v'v''}$ | 0.015 | 0.070 | 0.157 | 0.221 | 0.220 |
| | $\bar{r}_{v'v''}$ / Å | 1.907 | 1.931 | 1.956 | 1.981 | 2.007 |
| | $\lambda_{v'v''}$ / Å | 3581.71 | 3688.30 | – | – | – |
| $v' = 1$ | $q_{v'v''}$ | 0.053 | 0.149 | 0.152 | 0.051 | 0 |
| | $\bar{r}_{v'v''}$ / Å | 1.890 | 1.914 | 1.937 | 1.961 | |
| | $\lambda_{v'v''}$ / Å | 3511.56 | 3613.89 | – | – | |
| $v' = 2$ | $q_{v'v''}$ | 0.104 | 0.148 | 0.033 | 0.016 | 0.102 |
| | $\bar{r}_{v'v''}$ / Å | 1.874 | 1.897 | 1.918 | 1.949 | 1.971 |
| | $\lambda_{v'v''}$ / Å | 3444.64 | – | – | – | – |
| $v' = 3$ | $q_{v'v''}$ | 0.143 | 0.079 | 0.004 | 0.089 | 0.045 |
| | $\bar{r}_{v'v''}$ / Å | 1.858 | 1.880 | 1.911 | 1.928 | 1.950 |
| $v' = 4$ | $q_{v'v''}$ | 0.158 | 0.016 | 0.056 | 0.059 | 0.003 |
| | $\bar{r}_{v'v''}$ / Å | 1.843 | 1.863 | 1.889 | 1.910 | 1.946 |
| $v' = 5$ | $q_{v'v''}$ | 0.148 | 0 | 0.084 | 0.004 | 0.056 |
| | $\bar{r}_{v'v''}$ / Å | 1.828 | – | 1.873 | 1.888 | 1.920 |
| | $\lambda_{v'v''}$ / Å | 3261.37 | – | – | – | – |
| $v' = 6$ | $q_{v'v''}$ | 0.123 | 0.025 | 0.057 | 0.014 | 0.059 |
| | $\bar{r}_{v'v''}$ / Å | 1.813 | 1.837 | 1.857 | 1.884 | 1.902 |
| | $\lambda_{v'v''}$ / Å | 3206.08 | – | – | – | – |
| $v' = 7$ | $q_{v'v''}$ | 0.092 | 0.060 | 0.017 | 0.053 | 0.014 |
| | $\bar{r}_{v'v''}$ / Å | 1.799 | 1.822 | 1.841 | 1.866 | 1.884 |
| | $\lambda_{v'v''}$ / Å | 3153.58 | – | 3322.59 | – | – |
| $v' = 8$ | $q_{v'v''}$ | 0.064 | 0.084 | 0 | 0.061 | 0.002 |
| | $\bar{r}_{v'v''}$ / Å | 1.785 | 1.807 | – | 1.851 | 1.883 |
| | $\lambda_{v'v''}$ / Å | 3103.01 | 3183.00 | – | 3352.64 | – |
| $v' = 9$ | $q_{v'v''}$ | 0.042 | 0.090 | 0.013 | 0.036 | 0.029 |
| | $\bar{r}_{v'v''}$ / Å | 1.772 | 1.794 | 1.817 | 1.836 | 1.860 |
| | $\lambda_{v'v''}$ / Å | 3054.71 | – | – | – | – |
| $v' = 10$ | $q_{v'v''}$ | 0.026 | 0.081 | 0.038 | 0.009 | 0.051 |
| | $\bar{r}_{v'v''}$ / Å | 1.759 | 1.780 | 1.802 | 1.820 | 1.845 |
| $v' = 11$ | $q_{v'v''}$ | 0.015 | 0.065 | 0.060 | 0 | 0.044 |
| | $\bar{r}_{v'v''}$ / Å | 1.746 | 1.767 | 1.789 | – | 1.830 |
| | $\lambda_{v'v''}$ / Å | – | – | 3113.22 | – | – |
| $v' = 12$ | $q_{v'v''}$ | 0.009 | 0.048 | 0.069 | 0.012 | 0.020 |
| | $\bar{r}_{v'v''}$ / Å | 1.733 | 1.754 | 1.776 | 1.798 | 1.816 |

The Franck–Condon factors of the band $B^1\Pi - X^1\Sigma^+$ system of $^{123}$SbP and $^{121}$SbP species indicate that the following bands (0,0), (0,1), (0,2), (0,3), (1,0), (1,1), (1,3), (1,4), (15), (2,0), (2,2), (2,5), (2,6), (2,7), (3,0), (3,4), (3,7), (3,8), (4,1) and (4,3) are intense (F–C factors > 0.1), while all other bands are weak.

Since $r_e' > r_e''$, the *r*-centroid values increase with increasing wavelength, which is expected in the red degraded band system.

TABLE III. Franck–Condon factors, *r*-centroids and wavelengths of the $D^2\Pi - X^2\Pi$ system of $^{121}SbP$

| | | $v'' = 0$ | $v'' = 1$ | $v'' = 2$ |
|---|---|---|---|---|
| $v' = 0$ | $q_{v'v''}$ | 0 | 0.003 | 0.012 |
| | $\bar{r}_{v'v''}$ / Å | – | 1.956 | 1.976 |
| | $\lambda_{v'v''}$ / Å | – | 3004.81 | 3077.90 |
| $v' = 1$ | $q_{v'v''}$ | 0.002 | 0.013 | 0.046 |
| | $\bar{r}_{v'v''}$ / Å | 1.926 | 1.944 | 1.963 |
| | $\lambda_{v'v''}$ / Å | 2892.01 | 2960.83 | 3031.78 |
| $v' = 2$ | $q_{v'v''}$ | 0.006 | 0.036 | 0.086 |
| | $\bar{r}_{v'v''}$ / Å | 1.914 | 1.933 | 1.951 |

TABLE IV. Franck–Condon factors, *r*-centroids and wavelengths of the $B^1\Pi - X^1\Sigma^+$ system of $^{123}SbP$

| | | $v'' = 0$ | $v'' = 1$ | $v'' = 2$ | $v'' = 3$ | $v'' = 4$ | $v'' = 5$ | $v'' = 6$ | $v'' = 7$ | $v'' = 8$ |
|---|---|---|---|---|---|---|---|---|---|---|
| $v' = 0$ | $q_{v'v''}$ | 0.139 | 0.285 | 0.282 | 0.178 | 0.080 | 0.028 | 0.007 | 0.002 | 0 |
| | $\bar{r}_{v'v''}$ Å | 2.258 | 2.290 | 2.321 | 2.353 | 2.385 | 2.417 | 2.450 | 2.583 | – |
| | $\lambda_{v'v''}$ Å | 3560.68 | 3624.68 | 3690.59 | 3758.49 | 3827.17 | – | – | – | – |
| $v' = 1$ | $q_{v'v''}$ | 0.257 | 0.132 | 0 | 0.113 | 0.205 | 0.166 | 0.085 | 0.031 | 0.009 |
| | $\bar{r}_{v'v''}$ Å | 2.234 | 2.265 | – | 2.328 | 2.359 | 2.391 | 2.423 | 2.456 | 2.489 |
| | $\lambda_{v'v''}$ Å | – | – | | – | 3771.68 | 3841.67 | 3913.83 | – | – |
| $v' = 2$ | $q_{v'v''}$ | 0.254 | 0 | 0.132 | 0.087 | 0 | 0.102 | 0.179 | 0.142 | 0.070 |
| | $\bar{r}_{v'v''}$ Å | 2.209 | – | 2.272 | 2.302 | – | 2.366 | 2.398 | 2.430 | 2.462 |
| | $\lambda_{v'v''}$ Å | 3463.38 | – | 3591.32 | – | – | 3784.17 | 3854.16 | 3926.31 | – |
| $v' = 3$ | $q_{v'v''}$ | 0.177 | 0.067 | 0.095 | 0.012 | 0.122 | 0.041 | 0.013 | 0.121 | 0.165 |
| | $\bar{r}_{v'v''}$ Å | 2.186 | 2.217 | 2.247 | 2.280 | 2.309 | 2.339 | 2.376 | 2.405 | 2.436 |
| | $\lambda_{v'v''}$ Å | 3417.38 | – | – | – | 3663.33 | – | 3797.30 | – | – |
| $v' = 4$ | $q_{v'v''}$ | 0.098 | 0.149 | 0.003 | 0.108 | 0.020 | 0.053 | 0.100 | 0.007 | 0.044 |
| | $\bar{r}_{v'v''}$ Å | 2.162 | 2.193 | 2.222 | 2.254 | 2.283 | 2.317 | 2.347 | 2.373 | 2.412 |
| | $\lambda_{v'v''}$ Å | – | 3429.40 | – | – | – | – | – | – | – |

If the sequence difference $\Delta\bar{r}_{v'v''} = \bar{r}_{v'+1,v''+1} - \bar{r}_{v',v''}$ was found to be constant (≈ 0.01 Å) for a given sequence, then it can be interpreted that the potential curves are not wide. In the present study, the sequence differences of all the considered band systems were found to be constant and are about 0.01 Å, which suggests that the potentials are not wide.

TABLE V. Franck–Condon factors, *r*-centroids and wavelengths of the $B^1\Pi - X^1\Sigma^+$ system of $^{121}$SbP

| | | $v''=0$ | $v''=1$ | $v''=2$ | $v''=3$ | $v''=4$ | $v''=5$ | $v''=6$ | $v''=7$ | $v''=8$ |
|---|---|---|---|---|---|---|---|---|---|---|
| $v'=0$ | $q_{v'v''}$ | 0.154 | 0.298 | 0.279 | 0.167 | 0.072 | 0.023 | 0.006 | 0.001 | 0 |
| | $\bar{r}_{v'v''}$ Å | 2.259 | 2.291 | 2.323 | 2.355 | 2.388 | 2.421 | 2.454 | 2.488 | – |
| | $\lambda_{v'v''}$ Å | 3559.28 | 3623.65 | 3689.68 | 3757.68 | 3827.79 | – | – | – | – |
| $v'=1$ | $q_{v'v''}$ | 0.271 | 0.117 | 0.003 | 0.132 | 0.210 | 0.157 | 0.075 | 0.026 | 0.007 |
| | $\bar{r}_{v'v''}$ Å | 2.234 | 2.265 | 2.301 | 2.330 | 2.362 | 2.394 | 2.427 | 2.460 | 2.494 |
| | $\lambda_{v'v''}$ Å | 3510.44 | 3572.74 | – | 3702.98 | 3771.02 | 3841.12 | 3913.41 | – | – |
| $v'=2$ | $q_{v'v''}$ | 0.255 | 0 | 0.145 | 0.072 | 0.006 | 0.121 | 0.182 | 0.132 | 0.061 |
| | $\bar{r}_{v'v''}$ Å | 2.209 | – | 2.273 | 2.304 | 2.340 | 2.369 | 2.401 | 2.434 | 2.467 |
| | $\lambda_{v'v''}$ Å | 3462.25 | – | 3585.16 | – | – | 3783.49 | 3853.59 | 3925.83 | – |
| $v'=3$ | $q_{v'v''}$ | 0.169 | 0.085 | 0.082 | 0.023 | 0.126 | 0.028 | 0.025 | 0.137 | 0.163 |
| | $\bar{r}_{v'v''}$ Å | 2.184 | 2.216 | 2.248 | 2.280 | 2.311 | 2.341 | 2.377 | 2.408 | 2.440 |
| | $\lambda_{v'v''}$ Å | 3416.16 | 3475.15 | 3535.83 | 3598.14 | 3662.44 | – | 3796.60 | 3866.70 | 3938.95 |
| $v'=4$ | $q_{v'v''}$ | 0.089 | 0.161 | 0 | 0.116 | 0.010 | 0.071 | 0.090 | 0 | 0.063 |
| | $\bar{r}_{v'v''}$ Å | 2.160 | 2.191 | – | 2.255 | 2.284 | 2.319 | 2.349 | – | 2.415 |
| | $\lambda_{v'v''}$ Å | – | 3428.13 | – | – | – | – | – | – | – |

The intensity ratio of the corresponding bands of isotopic molecules gives the abundance ratio of the molecules.[4] As the intensity is proportional to the Franck–Condon factor, Franck–Condon factor ratios also reflect the same.

From the present calculations, a Franck–Condon factor ratio of the isotopic species $^{123}$SbP and $^{121}$SbP of 1:0.9996 for the (0,0) band of the $B^1\Pi - X^1\Sigma^+$ system was obtained. The Franck–Condon factors ratio shows that the probability of transition and occurrence of isotopic molecules $^{123}$SbP and $^{121}$SbP are more or less the same in the same environment and allied sources.

TABLE IV. Molecular constants

| Molecule | State | $\omega_e$ | $\omega_e x_e$ / cm$^{-1}$ | $r_e$ / Å | $\alpha_e$ | $\beta_e$ |
|---|---|---|---|---|---|---|
| $^{123}$SbO | $A^2\Pi_{3/2}$ | 569.79 | 2.55 | 2.0336 | 0.001818 | 0.288028 |
| | $X^2\Pi_{3/2}$ | 813.34 | 4.29 | 1.8227 | 0.0023781 | 0.358524 |
| $^{121}$SbO | $C^2\Sigma$ | 570.00 | 3.52 | 1.997 | 0.002184 | 0.2991 |
| | $D^2\Pi$ | 505.90 | 3.00 | 2.073 | 0.002092 | 0.2777 |
| | $X^2\Pi_{3/2}$ | 814.07 | 4.3 | 1.8227 | 0.00238 | 0.358 |
| | $X^2\Pi_{1/2}$ | 816.00 | 4.2 | 1.825 | 0.0022 | 0.358 |
| $^{123}$SbP | $B^1\Pi$ | 393.10 | 1.624 | 2.314 | 0.0001 | 0.1273 |
| | $X^1\Sigma^+$ | 499.24 | 1.624 | 2.204 | 0.0005 | 0.1402 |
| $^{121}$SbP | $B^1\Pi$ | 394.00 | 1.632 | 2.313 | 0.0002 | 0.1278 |
| | $X^1\Sigma^+$ | 500.07 | 1.632 | 2.206 | 0.0005 | 0.1406 |

*Acknowledgements*: The authors thank the referee for the critical comments and valuable suggestions.

И З В О Д

## ПАРАМЕТРИ МОЛЕКУЛА SbO И SbP У ГАСОВИТОЈ ФАЗИ

P. SRI RAMACHANDRAN[1], V. RAJA[2] и N. RAJAMANICKAM[1]

*[1]Physics Research Centre, V.H.N.S.N College, Virudhunagar – 626 001 и [2]Department of Physical Chemistry, Kalasalingam University, Krishnankoil – 626 190, India*

Franck–Condon фактори и *r*-центроиди, који су уско повезани са вероватноћом релативних вибрационих прелаза, одређени су нумеричком интеграцијом за траке $A^2\Pi_{3/2} - X^2\Pi_{3/2}$, $C^2\Sigma - X^2\Pi_{3/2}$ и $D^2\Pi - X^2\Pi$ система изотопског молекула SbO и за $B^1\Pi - X^1\Sigma^+$ систем изотопског молекула SbP, помоћу погодног потенцијала.

(Примљено 10. новембра 2006)

## REFERENCES

1. M. Kuzmanović, A. Antić–Jovanović, D. Pešić, V. Bojović, *J. Serb. Chem. Soc.* **70** (2005) 727
2. M. B. Suresh Kumar, N. R. Shah, Ashish Jaituni, *Pramana* **60** (2003) 95
3. A. J. Sauval. J. B. Tatum, *Astrophys. J. Suppl. Ser*. **56** (1984) 193
4. B. P. Straughan, S. Walker, *Spectroscopy*, Vol. 3, Chapmann and Hall, London, 1976
5. P. M. Morse, *Phys. Rev*. **34** (1929) 57
6. J. T. Vanderslice, E. A. Mason, W. G. Maisch, E. R. Lippincott, *J. Mol. Spectrosc*. **3** (1959) 17
7. J. T. Vanderslice, E. A. Mason, W. G. Maisch, E. R. Lippincott, *J. Mol. Spectrosc*. **5** (1960) 83
8. D. R. Bates, *Proc. Roy. Soc*. **A196** (1949) 217
9. F. Partal Urena, M. Fernandez Gomez, J. J. Lopez Gonzalez, N. Rajamanickam, *Astrophys. Space Sci*. **272** (2000) 345
10. W. J. Balfour, R. S. Ram, *J. Mol. Spectrosc*. **105** (1984) 246
11. W.J. Balfour, R.S. Ram, *J. Mol. Spectrosc*. **130** (1988) 382.
12. S. V. J. Lakshman, *Zeitschrift Phys*. **158** (1960) 367
13. K. K. Yee, W. E. Jones, I. Kopp, *J. Mol. Spectrosc.* **33** (1970) 119
14. K. P. Huber, G. Herzberg, *Molecular Spectra and Molecular Structure*, Vol. IV, Constants of Diatomic Molecules, Van Nostrand Reinhold, New York, 1979.

Journal of the Serbian Chemical Society
JSCS@tmf.bg.ac.yu • www.shd.org.yu/JSCS
*J. Serb. Chem. Soc.* *73* (1) 73–85 (2008) UDC 547.261'122.6+547.534.2:532.11'13'14:539.121.62
*JSCS–3689* *Original scientific paper*

# Vapor pressure, density, viscosity and refractive index of dimethyl sulfoxide + 1,4-dimethylbenzene system

OANA CIOCIRLAN* and OLGA IULIAN

*Department of Applied Physical Chemistry and Electrochemistry, Faculty of Industrial Chemistry, "Politehnica" University of Bucharest, 313 Splaiul Independentei, 060042, Romania*

(Received 25 November 2006, revised 7 September 2007)

*Abstract*: This paper reports the experimental results of isothermal vapor–liquid equilibrium data between 303.15 and 333.15 K, and densities, viscosities, refractive indices from 298.15 to 323.15 K of the dimethyl sulfoxide + 1,4-dimethylbenzene system over the entire range of mixture composition. The obtained PTX data were correlated by the Wilson and NRTL models and estimated by the UNIFAC model. The excess Gibbs energy and activity coefficients were calculated and compared with others excess properties. Excess molar volumes, viscosity deviations and deviations in refractivity were calculated from the experimental data; all the computed quantities were fitted to the Redlich–Kister equation. The resulting excess functions were interpreted in terms of structure and interactions.

*Keywords*: dimethyl sulfoxide; 1,4-dimethylbenzene; VLE data; density; viscosity; excess properties.

## INTRODUCTION

Continuing our work on the thermodynamics of non-electrolyte systems, the present paper is a part of a study of binary systems containing dimethyl sulfoxide (DMSO) and aromatic hydrocarbons, interesting as mixed solvents.[1] Dimethyl sulfoxide is a versatile non-aqueous, aprotic, highly polar self-associated solvent used extensively in kinetic studies, electrochemistry and as a solvent for polymers. Binary mixtures of DMSO with aromatic solvents are interesting in studies of polymer miscibility, polymer phase diagrams and preferential interactions in mixed solvents.[2]

This paper reports experimental isothermal vapor liquid equilibrium (VLE) data at temperatures 303.15, 313.15, 323.15 and 333.15 K and experimental data of density, viscosity and refractive index at temperatures 298.15, 303.15, 313.15 and 323.15 K for the dimethyl sulfoxide + 1,4-dimethylbenzene system.

* Corresponding author. E-mail: ciocirlan_o@yahoo.com
doi: 10.2298/JSC0801073C

The VLE data were correlated by means of the Wilson[3] and NRTL[4] models; this work also served to test the predictive capacity of the group contribution methods: original UNIFAC[5] and UNIFAC–Dortmund.[6,7] Excess molar volumes, viscosity deviations and deviations in refractivity were calculated from the experimental data; all the computed quantities were fitted to the Redlich–Kister equation.

A survey of the literature[8] revealed only one source of VLE data for this binary system, in which the data are presented only as diagrams.[9] A few studies which considered the volumetric properties have been reported;[10–12] no literature data on viscosities and refractive indices are available for this system.

## EXPERIMENTAL

### *Materials*

The employed chemicals were purified by distillation. Dimethyl sulfoxide was distilled under vacuum at 0.8–0.9 kPa and 338.65 K. The analytical-reagent-grade 1,4-dimethylbenzene from Fluka (p.a.) was used without further purification. The pure substances were kept in airtight stoppered glass bottles to avoid air contact. The purity was checked by refractive index, density and gas chromatography. It was better than 99.5 mass %. The physical properties were checked by repeated measurements over an interval of 2–3 days, during which time no changes were observed. The experimental values of density, refractive index and viscosity of the pure components are presented in Table I and compared with literature values.

TABLE I. Experimental and literature values for the density ($\rho$), refractive index ($n_D$) and viscosity ($\eta$) of the pure components

| $T$ / K | $\rho\times10^{-3}$ / kg·m$^{-3}$ | | $n_D$ | | $\eta$ / mPa s | |
|---|---|---|---|---|---|---|
| | Lit. | Exp. | Lit. | Exp. | Lit. | Exp. |
| Dimethyl sulfoxide | | | | | | |
| 293.15 | 1.10050[13] | 1.10073 | | | | |
| | 1.10053[14] | | | | | |
| 298.15 | 1.0957[12] | 1.09574 | 1.4770[15] | 1.4768 | | 2.0388 |
| | 1.0962[15] | | | | | |
| | 1.0954[16] | | | | | |
| 303.15 | 1.0900[12] | 1.09074 | 1.4752[14] | 1.4733 | 1.830[14] | 1.8405 |
| | 1.09050[17] | | | | | |
| 313.15 | 1.0812[12] | 1.08075 | 1.4700[14] | 1.4694 | 1.534[14] | 1.5373 |
| | 1.08046[18] | | | | | |
| 1,4-Dimethylbenzene | | | | | | |
| 293.15 | 0.8611[19] | 0.86144 | | | | |
| 298.15 | 0.8568[12] | 0.85712 | 1.49320[10] | 1.4930 | 0.603[19] | 0.6282 |
| | 0.85670[21] | | 1.49286[20] | | | |
| | | | 1.4930[22] | | | |

### *Procedure*

The binary mixtures were prepared by mixing the appropriate volumes of liquids in airtight stoppered glass bottles and weighed using an HR-120 (A & D Japan) electronic balance with a precision of 0.0001 g. The experimental uncertainty in the mole fractions was estimated to be less than ±0.0002.

The total vapor pressure of the binary mixtures was measured at temperatures between 303.15 and 333.15 K by a static non analytic (synthetic) method, with a glass isotensioscope of the Smith and Menzies type, which allows the measurements of VLE at subatmospheric pressures at temperatures up to 423.15 K. Experimental apparatus used in this work was the same as that used in a previous study.[23] A schematic diagram of the apparatus is shown in Fig. 1. The apparatus consists of an equilibrium cell placed in a constant-temperature water bath. The experimental procedure was typical for static VLE measurements: a sample of known composition with a volume of about 4−5 $cm^3$ was introduced into the equilibrium cell at the beginning of each experiment, degassed by the freeze-thaw method under vacuum and then the temperature of the entire system was maintained constant by controlling the temperature of the water bath. After the desired temperature was attained, the total pressure was measured for the liquid mixture in the equilibrium cell. The temperature in the water bath was controlled by a U-10 type thermostat and measured with an Hg thermometer with an estimated accuracy of 0.05 K. The vapor pressures were measured by means of an Hg manometer and a cathetometer, with accuracy to within 0.026 kPa. As the vapor phase volume of the cell was relatively small, calculation showed that the error in composition due to vaporization is within this limit.

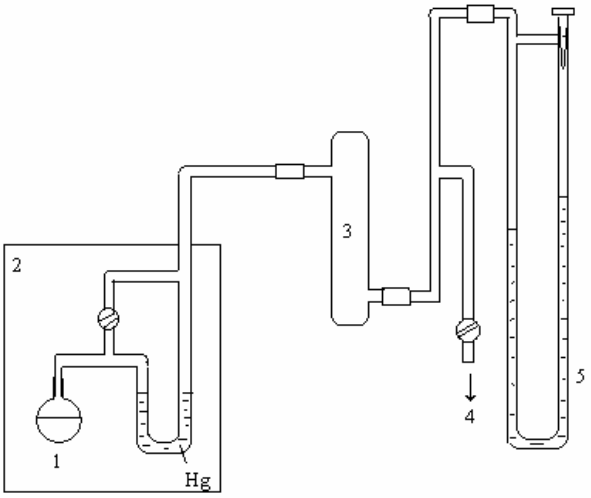


Fig. 1. Schematic diagram of the vapor–liquid equilibrium apparatus: 1, equilibrium cell; 2, constant-temperature water bath; 3, buffer vessel; 4, vacuum pump; 5, Hg manometer.

The densities, $\rho$, of the pure solvents and the mixtures were measured with an Anton Paar DMA 4500 densitometer with a precision of ±0.00005 g $cm^{-3}$, between 298.15 and 323.15 K. The DMA cell was calibrated with dry air and ultra pure water at atmospheric pressure. The sample size was 0.7 $cm^3$ and the sample thermostat was controlled to ±0.01 K. Triplicate measurements of the density were performed for all the mixtures and pure components. The accuracy in the determination of the density is believed to be less than ±0.2 kg $m^{-3}$ and ±$10^{-8}$ $m^3 \cdot mol^{-1}$ for the calculation of $V^E$.

The kinematic viscosity, $v$, of the pure components and their mixtures were determined at the same temperatures as were employed for the density measurements using an Ubbelohde capillary viscometer having a capacity of about 15 ml, a length of about 90 mm and 0.5 mm internal diameter. The viscometer was calibrated using doubly distilled water. At least four time flow measurements were performed for each composition and temperature, and the results were averaged. The viscometer was kept vertically in a transparent-walled bath with a thermal stability of ±0.05 K for about 30 min to attain thermal equilibrium. The uncertainty of

the flow time measurement was ±0.1 s. The corresponding uncertainty in the kinematic viscosity is ±0.001 $10^{-6}$ $m^2$ $s^{-1}$.

Refractive indices values for the D-line, $n_D$, were measured with a thermostated Abbe refractometer with a precision of ±0.0001. All measurements were performed in a thermostat maintained at ±0.05 K.

## RESULTS AND DISCUSSION

The measurements of total pressure were carried out at various compositions in the investigated temperature range. For each binary mixture, the dependencies between the experimental pressure and temperature were established. The functions $p = f(T)$ obtained by polynomial regression were used to calculate the VLE data at 303.15, 313.15, 323.15 and 333.15 K. The smoothed data resulting from the experimental measurements are reported in Table II. The temperature dependence of the vapor pressures of the pure component was calculated using the Antoine equation.[24, 25]

TABLE II. Vapor–liquid equilibrium data for the binary dimethyl sulfoxide (1) + 1,4-dimethyl benzene (2) system from 303.15 to 333.15 K. Smoothed values of the pressure by polynomial regression

| | $T$ / K | | | |
|---|---|---|---|---|
| $x_1$ | 303.15 | 313.15 | 323.15 | 333.15 |
| | $p$ / mm Hg | | | |
| 0 | 11.63 | 19.85 | 32.53 | 51.44 |
| 0.1235 | 12.51 | 18.74 | 32.50 | 54.10 |
| 0.2098 | 11.23 | 18.06 | 32.76 | 54.00 |
| 0.3029 | 8.95 | 16.40 | 30.00 | 52.01 |
| 0.4059 | 9.22 | 15.73 | 28.92 | 49.79 |
| 0.6348 | 8.18 | 14.31 | 27.01 | 46.30 |
| 0.8022 | 8.17 | 12.84 | 22.88 | 38.31 |
| 0.9078 | 5.54 | 10.48 | 17.60 | 26.90 |
| 0.9554 | 4.83 | 6.41 | 11.01 | 18.63 |
| 1 | 0.85 | 1.66 | 3.07 | 5.46 |

Various models are used for the correlation and prediction of binary VLE data: the Equations based on the local composition concept (Wilson and NRTL) and the group contribution methods, UNIFAC.

The results of the correlation with the Wilson and NRTL models are presented in Table III, which includes the values of the model parameters and the statistical parameters: average percentage deviation in pressure, $\Delta p$, and standard deviation, $\sigma$.

Prediction of the VLE data for the binary system at the investigated temperatures was performed using the original UNIFAC method and its modification, UNIFAC–Dortmund. The group interaction parameters were those published by Reid,[26] Hansen[27] and Gmehling.[6,7] The results of the predictions are also presented in Table III.

TABLE III. Results of the correlation and prediction with the Wilson, NRTL and UNIFAC models for the dimethyl sulfoxide (1) + 1,4-dimethylbenzene (2) system

| Model | Parameters J mol$^{-1}$ | Statistical parameters | |
|---|---|---|---|
| | | $\sigma^a$ / mm Hg | $\Delta p^b$ / % |
| | 303.15 K | | |
| Wilson | $\Delta\lambda_{12}$ = 4143.8<br>$\Delta\lambda_{21}$ = 2412.5 | 0.86 | 7.14 |
| NRTL ($\alpha$ = 0.3) | $\Delta g_{12}$ = 4067.7<br>$\Delta g_{21}$ = 1442.6 | 0.91 | 7.54 |
| Original UNIFAC | – | – | 6.25 |
| UNIFAC–Dortmund | | | 9.92 |
| | 313.15 K | | |
| Wilson | $\Delta\lambda_{12}$ = 3764.3<br>$\Delta\lambda_{21}$ = 346.4 | 0.41 | 2.64 |
| NRTL ($\alpha$ = 0.3) | $\Delta g_{12}$ = 4444.2<br>$\Delta g_{21}$ = 969.4 | 0.37 | 2.10 |
| Original UNIFAC | – | – | 7.99 |
| UNIFAC–Dortmund | | | 4.54 |
| | 323.15 K | | |
| Wilson | $\Delta\lambda_{12}$ = 6261.8<br>$\Delta\lambda_{21}$ = 1163.9 | 0.86 | 2.27 |
| NRTL ($\alpha$ = 0.3) | $\Delta g_{12}$ = 2620.0<br>$\Delta g_{21}$ = 3451.0 | 1.15 | 2.93 |
| Original UNIFAC | – | – | 3.79 |
| UNIFAC–Dortmund | | | 10.20 |
| | 333.15 K | | |
| Wilson | $\Delta\lambda_{12}$ = 9770.9<br>$\Delta\lambda_{21}$ = 455.2 | 1.07 | 1.91 |
| NRTL (α=0.3) | $\Delta g_{12}$ = 1649.8<br>$\Delta g_{21}$ = 5777.3 | 2.00 | 3.85 |
| Original UNIFAC | – | – | 3.48 |
| UNIFAC–Dortmund | | | 14.20 |

[a]Standard deviation $\sigma = \{\sum_i^N [p_{calc}(i) - p_{exp}(i)]^2 / (N - M)\}^{0.5}$ ($N$: number of data points and $M$: number of estimated parameters); [b]Average percentage deviation in pressure $\Delta p = (100/N)\{\sum_i^N | p_{calc}(i) - p_{exp}(i) | / p_{exp}(i)$

The Wilson and NRTL method give similar and good representation of the experimental data (except at 303.15 K); the values of $\sigma$ and $\Delta p$ characterize the data as satisfactory. It can be observed that the description of this system by the original UNIFAC method shows good agreement with the experimental data, as do the Wilson and NRTL models; the modified UNIFAC method gave less satisfactory results, especially at higher temperatures.

The experimental and calculated (with the Wilson model) total pressures *vs*. the liquid and vapor compositions for 303.15, 313.15, 323.15 and 333.15 K are presented in Fig. 2. The activity coefficients were calculated using the Wilson equation for the binary systems. The dependence of the activity coefficient on

composition at 313.15 K are presented in Fig. 3, the limiting values at infinite dilution of these coefficients also being given. The variation of the excess Gibbs energy of the system was also computed and represented, which showed positive deviations from ideality. Comparison of maximum obtained value of $G^E$ at 313.15 K with literature is satisfactory.[9]

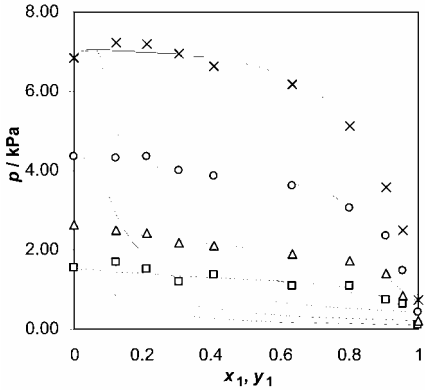


Fig. 2. Experimental vapor pressures of the dimethyl sulfoxide (1) + 1,4-dimethylbenzene (2) system at 303.15 K (□); 313.15 K (Δ); 323.15 K (○); 333.15 K (×); correlation with the Wilson model (—).

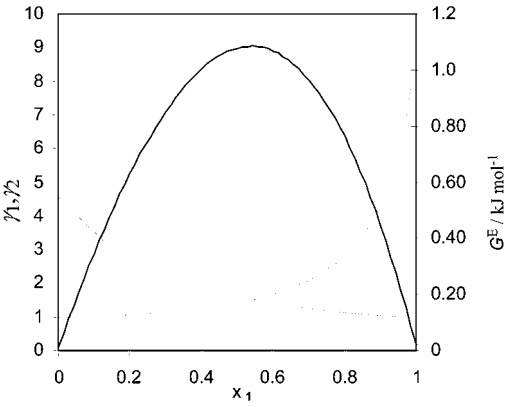


Fig. 3. Activity coefficients and excess Gibbs energy for the dimethyl sulfoxide (1) + 1,4-dimethylbenzene (2) system calculated with the Wilson model at 313.15 K.

The densities, viscosities and refractive indices were measured in the temperature range from 298.15 to 323.15 K and the measured values are listed in Table IV. The experimental densities correspond well with existing literature data.[10–12]

The values of the excess molar volume, $V^E$, viscosity deviation, $\Delta\nu$, and deviation in molar refractivity, $\Delta R$, were calculated from the experimental data according to the following equations:

$$V^E = V_m - \sum_{i=1}^{2} V_i x_i \quad (1)$$

$$\Delta\nu = \nu_m - \sum_{i=1}^{2} \nu_i x_i \quad (2)$$

$$\Delta R = R_m - \sum_{i=1}^{2} R_i \varphi_i \quad (3)$$

where $x_i$ and $\varphi_i$ represent the mole fraction and volume fraction of the pure component $i$, respectively; $V_m$, $\nu_m$, and $R_m$, the properties of the mixtures and $V_i$, $\nu_i$ and $R_i$, the properties of the pure components. The values of $\Delta R$ were calculated from the Lorentz–Lorenz equation.[28] The experimental excess molar volumes and deviations in viscosity are reported in Table IV.

TABLE IV. Experimental density, kinematic viscosity, refractive index, excess molar volume and viscosity deviation for the dimethyl sulfoxide (1) + 1,4-dimethylbenzene (2) system from 298.15 to 323.15 K

| $x_1$ | $\rho\times10^{-3}$ kg m$^{-3}$ | $V^E\times10^6$ m$^3$ mol$^{-1}$ | $x_1$ | $\nu\times10^6$ m$^2$ s$^{-1}$ | $\Delta\nu\times10^6$ m$^2$ s$^{-1}$ | $n_D$ | $x_1$ | $\rho\times10^{-3}$ kg m$^{-3}$ | $V^E\times10^6$ m$^3$ mol$^{-1}$ | $x_1$ | $\nu\times10^6$ m$^2$ s$^{-1}$ | $\Delta\nu\times10^6$ m$^2$ s$^{-1}$ | $n_D$ |
|---|---|---|---|---|---|---|---|---|---|---|---|---|---|
| 298.15 K | | | | | | | | | | | | | |
| 0.0000 | 0.85712 | 0.000 | 0.0000 | 0.733 | 0.000 | 1.4930 | 0.6077 | 0.97178 | –0.206 | 0.5969 | 1.198 | –0.209 | 1.4858 |
| 0.1029 | 0.87253 | –0.086 | 0.1056 | 0.788 | –0.064 | 1.4927 | 0.7048 | 0.99737 | –0.185 | 0.7009 | 1.332 | –0.192 | 1.4836 |
| 0.2033 | 0.88885 | –0.149 | 0.1975 | 0.844 | –0.112 | 1.4920 | 0.8024 | 1.02610 | –0.148 | 0.8022 | 1.485 | –0.153 | 1.4813 |
| 0.3056 | 0.90696 | –0.191 | 0.2988 | 0.915 | –0.155 | 1.4908 | 0.9002 | 1.05842 | –0.088 | 0.8978 | 1.652 | –0.094 | 1.4791 |
| 0.4085 | 0.92691 | –0.211 | 0.4033 | 0.999 | –0.189 | 1.4893 | 1.0000 | 1.09574 | 0.000 | 1.0000 | 1.861 | 0.000 | 1.4768 |
| 0.5042 | 0.94733 | –0.216 | 0.5126 | 1.104 | –0.207 | 1.4875 | – | – | – | – | – | – | – |
| 303.15 K | | | | | | | | | | | | | |
| 0.0000 | 0.85277 | 0.000 | 0.0000 | 0.692 | 0.000 | 1.4907 | 0.6077 | 0.96707 | –0.206 | 0.5969 | 1.110 | –0.176 | 1.4835 |
| 0.1029 | 0.86812 | –0.085 | 0.1056 | 0.745 | –0.052 | 1.4901 | 0.7048 | 0.99258 | –0.184 | 0.7009 | 1.227 | –0.163 | 1.4813 |
| 0.2033 | 0.88439 | –0.149 | 0.1975 | 0.797 | –0.091 | 1.4893 | 0.8024 | 1.02125 | –0.148 | 0.8022 | 1.360 | –0.130 | 1.4790 |
| 0.3056 | 0.90244 | –0.191 | 0.2988 | 0.861 | –0.129 | 1.4882 | 0.9002 | 1.05353 | –0.090 | 0.8978 | 1.506 | –0.080 | 1.4765 |
| 0.4085 | 0.92234 | –0.212 | 0.4033 | 0.936 | –0.158 | 1.4868 | 1.0000 | 1.09074 | 0.000 | 1.0000 | 1.687 | 0.000 | 1.4733 |
| 0.5042 | 0.94269 | –0.216 | 0.5126 | 1.028 | –0.174 | 1.4851 | – | – | – | – | – | – | – |
| 313.15 K | | | | | | | | | | | | | |
| 0.0000 | 0.84405 | 0.000 | 0.0000 | 0.630 | 0.000 | 1.4854 | 0.6077 | 0.95786 | –0.223 | 0.5969 | 0.967 | –0.137 | 1.4792 |
| 0.1029 | 0.85928 | –0.079 | 0.1056 | 0.672 | –0.042 | 1.4847 | 0.7048 | 0.98319 | –0.196 | 0.7009 | 1.060 | –0.125 | 1.4772 |
| 0.2033 | 0.87542 | –0.140 | 0.1975 | 0.714 | –0.073 | 1.4840 | 0.8024 | 1.01164 | –0.152 | 0.8022 | 1.166 | –0.100 | 1.4749 |
| 0.3056 | 0.89345 | –0.194 | 0.2988 | 0.765 | –0.101 | 1.4831 | 0.9002 | 1.04371 | –0.089 | 0.8978 | 1.280 | –0.061 | 1.4723 |
| 0.4085 | 0.91331 | –0.224 | 0.4033 | 0.826 | –0.123 | 1.4820 | 1.0000 | 1.08075 | 0.000 | 1.0000 | 1.423 | 0.000 | 1.4694 |
| 0.5042 | 0.93361 | –0.234 | 0.5126 | 0.901 | –0.136 | 1.4805 | – | – | – | – | – | – | – |
| 323.15 K | | | | | | | | | | | | | |
| 0.0000 | 0.83509 | 0.000 | 0.0000 | 0.578 | 0.000 | – | 0.6077 | 0.94825 | –0.231 | 0.5969 | 0.857 | –0.109 | – |
| 0.1029 | 0.85034 | –0.101 | 0.1056 | 0.612 | –0.034 | – | 0.7048 | 0.97351 | –0.208 | 0.7009 | 0.934 | –0.099 | – |
| 0.2033 | 0.86644 | –0.169 | 0.1975 | 0.647 | –0.060 | – | 0.8024 | 1.00189 | –0.168 | 0.8022 | 1.020 | –0.079 | – |
| 0.3056 | 0.88429 | –0.214 | 0.2988 | 0.690 | –0.082 | – | 0.9002 | 1.03382 | –0.104 | 0.8978 | 1.113 | –0.048 | – |
| 0.4085 | 0.90397 | –0.236 | 0.4033 | 0.740 | –0.099 | – | 1.0000 | 1.07057 | 0.000 | 1.0000 | 1.227 | 0.000 | – |
| 0.5042 | 0.92411 | –0.240 | 0.5126 | 0.802 | –0.108 | – | – | – | – | – | – | – | |

The experimental values of $V^E$, $\Delta v$ and $\Delta R$ were fitted to Redlich–Kister[29] type polynomials:

$$Y = x_1 x_2 \sum_{k=0}^{n} A_k (2x_1 - 1)^k \quad (4)$$

where $Y$ is $V^E$, $\Delta v$ or $\Delta R$ and $A_k$ represents the parameters. A nonlinear least-squares method was used to estimate the adjustable parameters $A_k$. The values of $A_k$ and standard deviation $\sigma$ are given in Table V.

TABLE V. The adjustable parameters and standard deviations of the excess functions of the dimethyl sulfoxide (1) + 1,4-dimethylbenzene (2) system

| Function | $A_0$ | $A_1$ | $A_2$ | $A_3$ | $\sigma$[a] |
|---|---|---|---|---|---|
| | | 298.15 K | | | |
| $V^E \times 10^6$ / m$^3$ mol$^{-1}$ | –0.8664 | –0.0306 | –0.1530 | 0.1023 | 0.0009 |
| $\Delta v \times 10^6$ / m$^2$ s$^{-1}$ | –0.7866 | –0.1422 | –0.0365 | | 0.0004 |
| $\Delta R \times 10^6$ / m$^3$ mol$^{-1}$ | –8.6332 | 2.0491 | –0.5638 | 0.1739 | 0.0022 |
| | | 303.15 K | | | |
| $V^E \times 10^6$ / m$^3$ mol$^{-1}$ | –0.8656 | –0.0465 | –0.1566 | 0.1576 | 0.0003 |
| $\Delta v \times 10^6$ / m$^2$ s$^{-1}$ | –0.6709 | –0.1593 | –0.0216 | | 0.0002 |
| $\Delta R \times 10^6$ / m$^3$ mol$^{-1}$ | –8.6048 | 2.2879 | –0.7394 | | 0.0058 |
| | | 313.15 K | | | |
| $V^E \times 10^6$ / m$^3$ mol$^{-1}$ | –0.9344 | 0.0234 | 0.0460 | 0.1186 | 0.0014 |
| $\Delta v \times 10^6$ / m$^2$ s$^{-1}$ | –0.5201 | –0.1044 | –0.0190 | | 0.0002 |
| $\Delta R \times 10^6$ / m$^3$ mol$^{-1}$ | –8.5246 | 2.1822 | –0.8037 | 0.5005 | 0.0041 |
| | | 323.15 K | | | |
| $V^E \times 10^6$ / m$^3$ mol$^{-1}$ | –0.9598 | –0.0287 | –0.2444 | 0.1199 | 0.0010 |
| $\Delta v \times 10^6$ / m$^2$ s$^{-1}$ | –0.4168 | –0.0705 | –0.0145 | | 0.0001 |

[a]Standard deviation $\sigma = \{\sum_{i}^{N} [Y_{calc}(i) - Y_{exp}(i)]^2 / (N - M)\}^{0.5}$ ($N$: number of data points and $M$: number of estimated parameters)

As can be seen from Figs. 4a, 4b and 4c, the main features of the system are that the excess molar volumes, deviations in viscosity and deviations in molar refractivity are all negative.

The excess volumes are moderately negative over the entire composition range and become slightly more negative as the temperature of the mixtures increases from 303.15 to 323.15 K. The present $V^E$ values at 303.15 K compare well with those reported by Wang *et al.*[11] obtained using the same experimental method (vibrating-tube densitometer), as can be seen in Fig. 5.

The dependence of $V^E$ on both composition and temperature for the present mixture may be explained as a balance between positive contributions (the breaking up of the associates or molecular order present in the pure liquids and dispersive interactions between unlike molecules) and negative contributions (inter-

molecular interactions and geometrical fitting between the components). In the present study, dimethyl sulfoxide is an aprotic, highly polar self-associated solvent, having a dipole moment $\mu$ = 3.96 D;[30] 1,4–dimethylbenzene is a non-polar, stable substance with a large quadrupole moment,[31] which causes molecular order in the pure state. On mixing, the molecular order in the aromatic hydrocarbon will decrease because of the DMSO molecules, whereas the molecular associations in pure DMSO will be disrupted by 1,4–dimethylbenzene. Their binary mixtures are characterized by electron donor–acceptor type interactions in which the aromatic hydrocarbon behaves as an electron donor.[32] The positive heats of mixing[9,10] for this system suggests the dominance of molecular dissociation over molecular association. In this case, the observed negative $V^E$ values may be explained by geometrical fitting of the molecules of different molecular sizes into each others structure (at 298.15 K, the molar volumes of the components are: $71.30\times10^{-6}$ for DMSO and $123.87\times10^{-6}$ m$^3$ mol$^{-1}$ for 1,4-dimethylbenzene).

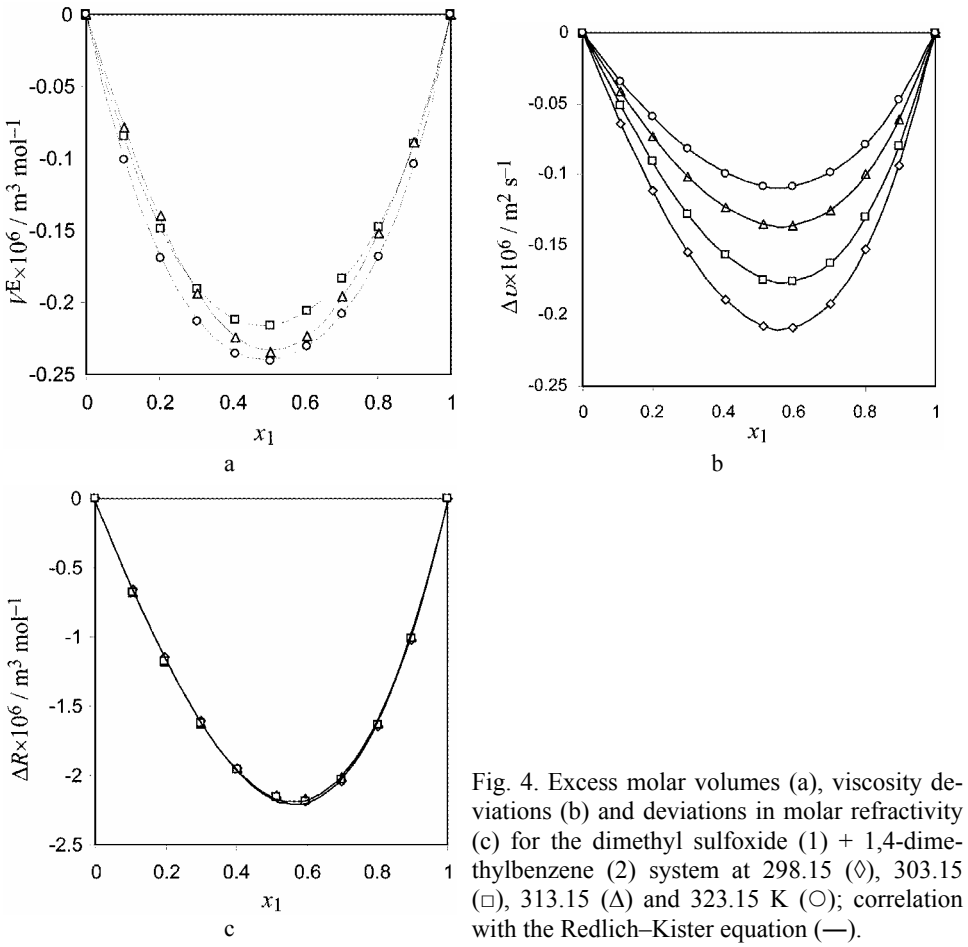


Fig. 4. Excess molar volumes (a), viscosity deviations (b) and deviations in molar refractivity (c) for the dimethyl sulfoxide (1) + 1,4-dimethylbenzene (2) system at 298.15 (◊), 303.15 (□), 313.15 (Δ) and 323.15 K (○); correlation with the Redlich–Kister equation (—).

The $\Delta v$ values are moderately negative over the whole composition range, rising with temperature. The geometrical fitting of the unlike molecules (structural effect) explains, also, the obtained negative $\Delta v$ values. Figs. 4a and 4b clearly indicate that $V^E$ and $\Delta v$ do not obey the general rule according to which they should have opposite signs, specific for systems where intermolecular interactions predominate. Therefore, the geometrical factor is more important for this system.

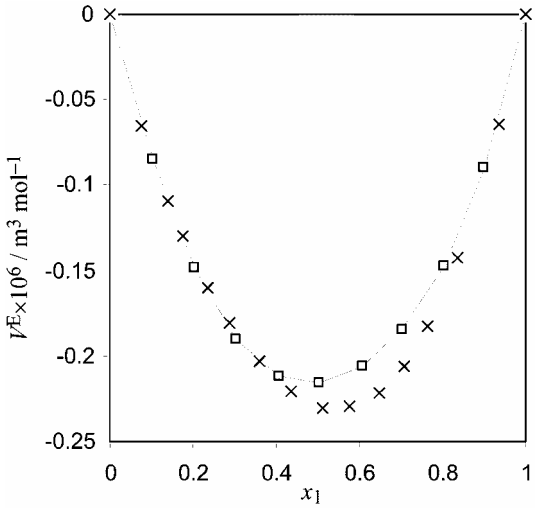


Fig. 5. Comparison of the excess molar volumes for the dimethyl sulfoxide (1) + 1,4-dimethylbenzene (2) system at 303.15 K: our data, (□); Ref. 11, (×); correlation with the Redlich–Kister equation, (—).

Moreover, the DMSO + 1,4–dimethylbenzene system shows positive deviations from the Raoult law, characteristic for systems without strong interactions between unlike molecules,[33] suggesting that the structural effect is predominant in this system. Similar cases are presented in the literature, *i.e.*, negative values of both $V^E$ and $\Delta\eta$ due to structural effects[34,35] and a positive deviation from the Raoult law, correlated with negative viscosity deviation in systems without strong specific interactions.[36]

In the present system, $V^E$ becomes slightly more negative as the temperature of the mixtures increases from 303.15 to 323.15 K. A similar, but more pronounced, trend of $V^E$ was obtained by Ali *et al.*,[12] an opposite trend being observed by Wang *et al.*[11] As a rule, the excess volumes become more positive as the temperatures increases, generally true for systems where the interactional factor is predominant. The opposite behavior, already observed in the literature for different systems,[37] could be attributed to the predominance of structural effects. It is felt that this last behavior is more reliable for the DMSO + 1,4–dimethylbenzene system, where structural effects predominate, as has been proved by this comprehensive study.

The $\Delta R$ values are negative for the whole composition range for all mixtures. The values are independent of temperature, according to theory, the molar refractivity depending only on the wavelength of light used for the measurements.

The results for the excess thermodynamic functions are in agreement with the result of experimental VLE data in this work.

## CONCLUSIONS

Experimental data concerning the isothermal vapor–liquid equilibriums in the binary 1,4-dimethylbenzene + DMSO system have been presented. Eight different mixtures containing 1,4-dimethylbenzene + DMSO were analyzed. Good agreement between the experimental and calculated values of the pressure was observed for the Wilson and NRTL correlative methods and for the original UNIFAC predictive method.

Experimental data for the densities, kinematic viscosities and refractive indices for the binary system DMSO + 1,4–dimethylbenzene are reported. Excess functions were calculated and fitted to the Redlich–Kister equation. All the excess functions are negative over the whole composition range. The trends in the dependence on composition of the excess properties are in agreement with the result of the experimental VLE data and indicate that the contribution from structural effects is predominant over interactional contributions in this system.

## SYMBOLS

$A_i$, $B_i$, $C_i$ – Parameters of the Antoine equation
$A_k$ – Redlich–Kister parameters
$G^E$ – Excess Gibbs energy
$g_{ij}$ – Parameters of the NRTL equation
$M$ – Number of model parameters
$N$ – Number of experimental points
$n_D$ – Refractive index
$\Delta p$ – Average percentage deviation in pressure
$p_{exp}$ – Experimental total pressure
$p_{calc}$ – Computed total pressure
$p_i^0$ – Vapor pressure of the $i$–th pure component
$\Delta R$ – Deviation in molar refractivity
$R_m$ – Molar refractivity of mixture
$R_i$ – Molar refractivity of the $i$–th pure component
$T$ – Absolute temperature
$V^E$ – Excess molar volume
$V_m$ – Molar volume of mixture
$V_i$ – Molar volume of the $i$–th pure component
$x_i$ – Liquid-phase mole fractions

*Greek letters*

$\gamma_k$ – Activity coefficients
$\lambda_{ij}$ – Parameters of Wilson equation
$\mu$ – Dipole moment
$\eta$, $\nu$ – Dynamic and kinematic viscosity, respectively
$\Delta\nu$ – Viscosity deviation
$\nu_m$ – Kinematic viscosity of mixture

$v_i$ – Kinematic viscosity of the *i*–th pure component
$\rho$ – Density
$\sigma$ – Standard deviation
$\varphi_i$ – Volume fraction.

## ИЗВОД

## НАПОН ПАРЕ, ГУСТИНА И ИНДЕКС РЕФРАКЦИЈЕ СИСТЕМА ДИМЕТИЛ СУЛФОКСИД + 1,4-ДИМЕНТИЛБЕНЗЕН

OANA CIOCIRLAN и OLGA IULIAN

*Department of Applied Physical Chemistry and Electrochemistry, Faculty of Industrial Chemistry, "Politehnica" University of Bucharest, 313 Splaiul Independentei, 060042, Romania*

У овом раду дати су експериментални подаци за изотермску равнотежу пара–течност у опсегу температура 303,15–333,15 K, као и густине, вискозности и индекса рефракције смеше диметил сулфоксида и 1,4-диметилбензена на температурама од 298,15 до 323,15 K, у комплетном опсегу састава смеше. Добијени PTX подаци корелисани су моделима Wilson и NRTL и процењени моделом UNIFAC. Израчунате су вредности вишка Гибсове енергије и коефицијенти активности и упоређене са вредностима вишка других величина. Вишак моларне запремине и одступања вискозности и моларне рефракције израчунате су на основу експерименталних података; све израчунате величине фитоване су Redlich–Kister једначином. Добијене функције вишка величина тумачене су на основу структуре и интеракција молекула смеше.

(Примљено 25. новембра 2006, ревидирано 7. септембра 2007)

## REFERENCES

1. O. Ciocirlan, O. Iulian, M. Catrinciuc, *Proceedings of the 13th Romanian International Conference on Chemistry and Chemical Engineering*, Bucuresti, Romania, 2003, p. 114
2. T. M. Aminabhavi, P. Munk, *Macromolecules* **12** (1979) 607
3. G. M. Wilson, *J. Am. Chem. Soc.* **86** (1964) 127
4. H. Renon, J. M. Prausnitz, *AIChE J.* **1** (1968) 135
5. A A. Fredenslund, J. Gmehling, P. Rasmussen, *Vapor–Liquid Equilibria Using UNIFAC*, Elsevier, Amsterdam, 1977
6. U. Weidlich, J. Gmehling, *Ind. Eng. Chem. Res.* **26** (1987) 1372
7. J. Gmehling, J. Li, M. Schiller, *Ind. Eng. Chem. Res.* **32** (1993) 178
8. I. Wichterle, J. Linek, Z. Wagner, H. Kehiaian, *Vapor–Liquid Equilibrium Bibliographic Database*, ELDATA SARL, Montreuil**,** 1993, p. 318
9. M. Karvo, A. Nissema, T. Kaivamo, *Finn. Chem. Lett.* **7**–**8** (1983) 137
10. A. H. Absood, M. S. Tununji, K.–Y. Hsu, H. L. Clever, *J. Chem. Eng. Data* **21** (1976) 304
11. H. Wang, W. Liu, J. Huang, *J. Chem. Thermodyn.* **36** (2004) 743
12. A. Ali, A.K. Nain, D. Chand, R. Ahmad, *Bull. Chem. Soc. Jpn.* **79** (2006) 702
13. G. Korosi, E. Kovats, *J. Chem. Eng. Data* **26** (1981) 323
14. N. G. Tsierkezos, A. E. Kelarakis, M. A. Palaiologou, *J. Chem. Eng. Data* **45** (2000) 395
15. M. I. Aralaguppi, T. M. Aminabhavi, S. B. Harogoppad, R.H. Balundgi, *J. Chem. Eng. Data* **37** (1992) 298
16. J. A. Riddick, W. B. Bunger, T. K. Sakano, *Techniques of Chemistry, Vol. II, Organic Solvents*, *4th Ed.*, Wiley, 1986
17. P. S. Nikam, M. C. Jadvav, M. Hasan, *J. Chem. Eng. Data* **41** (1996) 1028

18. D. J. Pruett, L. K. Felker, *J. Chem. Eng. Data* **30** (1985) 452
19. D. R. Lide, H. P. R. Frederikse, in *Handbook of Chemistry and Physics*, *77th Ed.*, CRC Press Inc., Florida, 1996–1997, Ch. 6, p. 211; Ch. 15, p. 18
20. C. Diaz, A. Dominiguez, J. Tojo, *J. Chem. Eng. Data* **47** (2002) 867
21. *TRC Thermodynamic Tables*, Thermodynamic Research Center, Texas A&M University, College Station, TX, USA, 1996
22. M. T. Lores, J. de la Torre, M. C. Burguet, J. B. Monton, *J. Chem. Eng. Data* **44** (1999) 869
23. O. Iulian, D. Geană, O. Landauer, C. Mateescu, *Rev. Roum. Chim.* **34** (1989) 1209
24. A. Maczynski, Z. Maczynska, *Verified Vapor Liquid Equilibrium Data, Vol. 4*, *Binary Systems of Hydrocarbons and Oxygen Compounds without Alcohols and Acids*, P. W. N, Warszawa, Poland, 1981, p. 28
25. A. Maczynski, A. Bilinski, P. Oracz, T. Treszczanowicz, *Verified Vapor Liquid Equilibrium Data, Vol. 6, Binary Systems of $C_{4+}$ Hydrocarbons and Alcohols*, P. W. N, Warszawa, Poland, 1982, p. 81
26. R. C. Reid, J. M. Prausnitz, B. E. Poling, *Properties of Gases and Liquids,* McGraw Hill Book Co., New York, 1988, p. 314
27. H. K. Hansen, P. Rasmussen, A. A. Fredenslund, M. Schiller, *Ind. Eng. Chem. Res.* **30** (1991) 2352
28. H. A Lorentz, *Theory of Electrons*, Teubner, Leipzig, Germany, 1909
29. O. Redlich, A. T. Kister, *Ind. Eng. Chem.* **40** (1948) 345
30. J. A. Dean, *Lange's Handbook of Chemistry*, McGraw–Hill, New York, 1956
31. D. Patterson, *J. Solution Chem.* **23** (1994) 105
32. D. V. Fenby, G. B. Billing, D. B. Smythe, *J. Chem. Thermodyn.* **5** (1973) 49
33. J. M. Prausnitz, R. N. Lichtenthaler, E. G. Azevedo, *Molecular Thermodynamics of Fluid Phase Equilibria*, *3rd Ed.*, Prentice–Hall Inc., New Jersey, 1999, p. 268
34. P. Nikam, S. J. Kharat, *J. Chem. Eng. Data* **48** (2003) 972
35. A. S. Al–Jimaz, J. A. Al–Kandary, A.–H. A–Latif, *Fluid Phase Equilib.* **218** (2004) 247
36. H. Vogel, A. Weiss, *Ber. Bunsen–Ges*. **86** (1982) 193
37. A. Valtz, M. Teodorescu, I. Wichterle, D. Richon, *Fluid Phase Equilib.* **215** (2004) 129.

Journal of the Serbian Chemical Society
JSCS@tmf.bg.ac.yu • www.shd.org.yu/JSCS
*J. Serb. Chem. Soc.* 73 (1) 87–95 (2008) UDC 543.544:*ibuprofen+*indomethacin+*naproxen:547.288.1
*JSCS–3690* *Original scientific paper*

# Potentiometric determination of ibuprofen, indomethacin and naproxen using an artificial neural network calibration

A. HAKAN AKTAŞ* and GÜZIDE PEKCAN ERTOKUŞ

*Department of Chemistry, Faculty of Science & Art, Süleyman Demirel University, 32260 Isparta, Turkey*

(Received 14 July 2006, revised 26 July 2007)

*Abstract*: In this study, three anti-inflammatory agents, namely ibuprofen, indomethacin and naproxen, were titrated potentiometrically using tetrabutylammonium hydroxide in acetonitrile solvent under a nitrogen atmosphere at 25 °C. MATLAB 7.0 software was applied for data treatment as a multivariate calibration tool in the potentiometric titration procedure. An artificial neural network (ANN) was used as a multivariate calibration tool in the potentiometric titration to model the complex non-linear relationship between ibuprofen, indomethacin and naproxen concentrations and the millivolt (mV) of the solutions measured after the addition of different volumes of the titrant. The optimized network predicted the concentrations of agents in synthetic mixtures. The results showed that the employed ANN can precede the titration data with an average relative error of prediction of less than 2.30 %.

*Keywords*: anti-inflammatory agents; potentiometric titration; artificial neural network (ANN).

## INTRODUCTION

Ibuprofen, indomethacin and naproxen are widely used clinically as non-steroidal anti-inflammatory agents. Their chemical structures are presented in Fig. 1. Several analytical methods have been reported in the literature for the determination of ibuprofen, indomethacin and naproxen in pharmaceutical preparations, including: flow-injection analysis – FTIR,[1] high performance liquid chromatography[2] and a potentiometric titration method for ibuprofen; spectrofluorimetry,[3] titrimetric methods[4,5] and spectrophotometric methods[6,7] for indomethacin; chemiluminescence,[8] capillary electrophoresis,[9,10] spectrofluorometry[11] and high performance liquid chromatography[12,13] for naproxen.

The European Pharmacopoeia describes methods for the routine analysis of these anti-inflammatory agents in pure form or in pharmaceutical formulations. The described volumetric methods, however, have some disadvantages. They are

* Corresponding author. E-mail: ahakan@fef.sdu.edu.tr
doi: 10.2298/JSC0801087A

time consuming with poor precision and sensitivity and chemical indicators[14] are used for the end-point determination in the presence of colored or non-soluble excipients in the drug formulations.

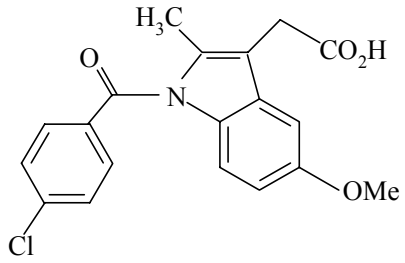


Indomethacin

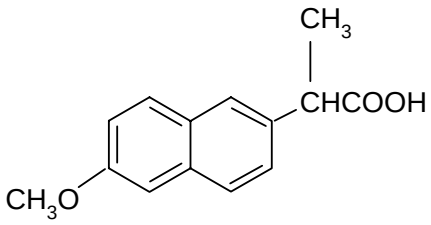


Naproxen

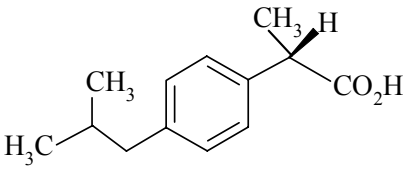


Ibuprofen

Fig. 1. Chemical structure and names of the studied compounds.

Potentiometric titrations are usually accurate but rather time-consuming and not suitable for the determination of very small quantities. A frequently encountered difficulty lies in the end-point determination, which arises from unstable electrode potentials.

Artificial neural networks (ANN) analyses are currently recognized as an effective and advantageous way to handle complex data and solve problems of non-linear calibration, pattern recognition, classification, prediction, and other related fields in analytical chemistry.[15–21] The corresponding non-linear multivariate maps use a non-linear transformation of the input variable to project inputs on to the designated attribute values in the output space. The strength of modeling with layered, feed-forward ANN lies in the flexibility of the distributed soft model defined by the weights of the network. Both linear and non-linear mapping functions can be modeled by suitably configuring the network. Multilayer, feed-forward neural networks trained with a back-propagation learning algorithm have become an increasingly popular technique.[22–24]

The non-linear relationship between mV and analyte concentration can be modeled by an ANN. In this study, a three-layer ANN was used with a back-propagation of error algorithm for modeling the complex relationship between mV and concentration through a multi-component titration. In order to decrease the number of data points, the data were factor analyzed before entering into the ANN. The original data were used as the input of the neural network. The method was applied to the simultaneous determination of ibuprofen, indomethacin and naproxen in their ternary mixtures and satisfactory results were obtained.

There are a number of publications on multivariate analysis, including: PLS and ANN for ibuprofen;[25,26] PLS and ANN for indomethacin[27,28] and PLS for naproxen.[29,30] However, no reports dealing with artificial neural networks of multicomponent analysis for ibuprofen, indomethacin and naproxen together have hitherto appeared.

## EXPERIMENTAL

### *Apparatus*

The electrode potentials were measured using a Hanna 9321 Microprocessor pH meter. A glass–silver chloride electrode system was used and the silver–silver chloride electrode was modified by replacing the saturated aqueous KCl solution with a saturated solution of KCl in methanol. All titrations were performed manually, under a nitrogen atmosphere at 25 °C.

### *Materials*

Ibuprofen, indomethacin and naproxen, obtained from Refik Saydam Hygiene Centre (Ankara, Turkey), were chemically pure laboratory working standards having a purity of 99.6, 99.9 and 99.2 %, respectively.

Ibu-600 (Sifar) was labeled as containing 600 mg ibuprofen per tablet. Endol (Deva) was labeled as containing 25 mg indomethacin per capsule. Approwell Fort (Ali Raif) was labeled as containing 550 mg naproxen per tablet.

### *Potentiometric titration procedure*

In a typical titration, a suitable amount of an individual drug agent or a mixture was placed in a 50 ml vessel and 5 ml 2-propanol was added to the solution. The solution was stirred and titrated with 0.0200 M tetrabutylammonium hydroxide solution using a micro-burette. The mV was recorded after each 0.02 ml addition of the titrant. For each solution, at least 70 data points were recorded.

### *Solutions of the pharmaceutical formulations*

Capsule: Ten Endol capsules were weighed, and their average contents were calculated. The contents were pooled and powdered, and the required amount of this powder was accurately weighed and dissolved in 20 ml of acetonitrile as solvent.

Tablets: Ten or twenty Approwell Fort or Ibu-600 tablets were weighed and their averages were calculated. All the tablets were pooled and powdered, and the required amount of this powder was accurately weighed and dissolved in 20 ml of acetonitrile.

### *Methodology*

A feed-forward ANN model with four layers of nodes was constructed as in Fig. 2.

An artificial neuron is the building component of an ANN designed to simulate the function of a biological neuron. The arriving signals, called inputs, multiplied by the connection weighted (adjusted) are first summed (combined) and then passed through a transfer function to the output of that neuron. The activation function is the weighed sum of the neuron's inputs and the most commonly used transfer function is a sigmoid function (Fig. 2).

A logistic function was used as the activation function in the neural network. The training and testing data sets must be normalized into the range 0.1–0.9. The input and the output data sets were normalized using the following equation:

$$X_{\mathrm{N}} = 0.1 + \frac{0.8(X - X_{\min})}{(X_{\max} - X_{\min})} \quad (1)$$

where $X_{\mathrm{N}}$ is the normalized value of a variable (the network input or the network output), $X$ is the original value of a variable, and $X_{\max}$ and $X_{\min}$ are the maximum and minimum original

values of the variables, respectively. In order to produce sufficient data for training and testing of the model shown in Fig. 2, 9 different standard solutions were prepared using different concentrations of the agent and each standard solution was subjected to potentiometric titration. Randomly chosen 945 data pairs from these 1260 data pairs were used in the training of the neural network and the rest of the data were used in the testing. The root mean square error values were calculated from the following equation to prove quantitatively the accuracy of the testing results of the neural network models:

$$RMS = \sqrt{0.5N^{-1}\sum_{i=1}^{N}(X_1' - X_1)^2} \quad (2)$$

where $N$ is the number of testing data and $X_1'$ is the target value.

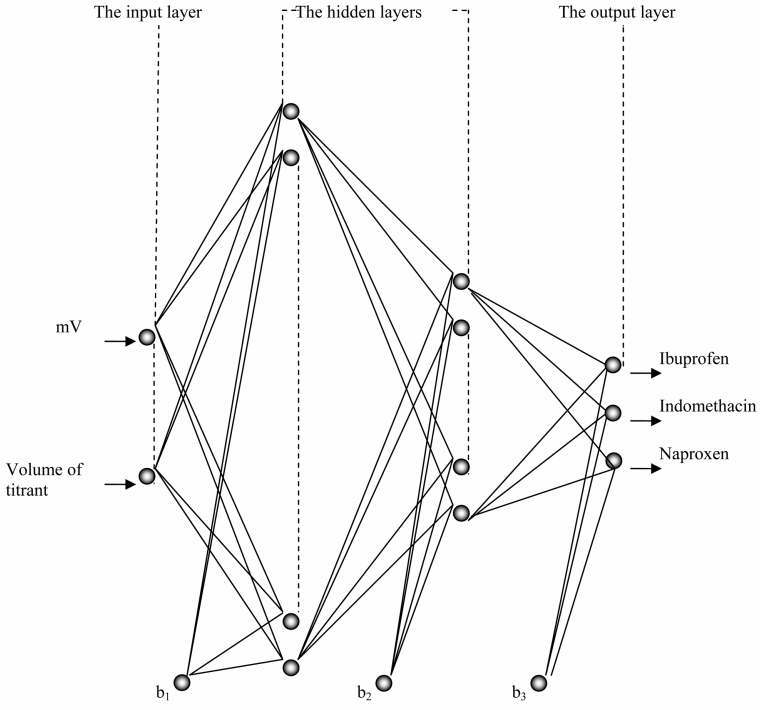


Fig. 2. Network architecture used in the potentiometric titration modeling ($b_1$ and $b_2$ are bias units).

MATLAB 7.0 software was used to construct the ANN models which have a sigmoidal logistic function with a back propagation of error algorithm. For this neural network modeling, an input layer, one or two hidden layers and an output layer were used.

## RESULTS AND DISCUSSION

Ibuprofen, indomethacin and naproxen were directly titrated potentiometrically in acetonitrile with tetrabutylammonium hydroxide as the titrant. The mV titration curves of these agents and their mixtures are shown in Figs. 3 and 4. It is obvious that the titration curves of these three agents seriously overlap.

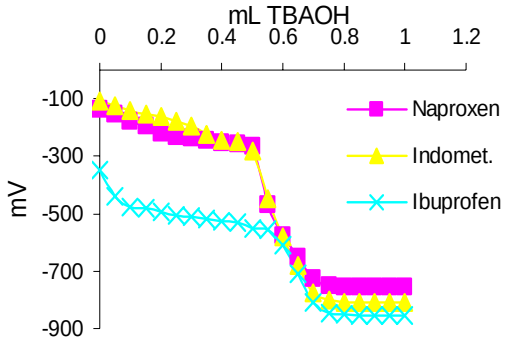


Fig. 3. Potentiometric titration curves for ibuprofen, indomethacin and naproxen titrated with tetrabutylammonium hydroxide in acetonitrile solution.

To obtain the best network performance, the optimal network architecture and parameters must be chosen. Studies of the network structure include the selection of the number of layers and number of nodes in each layer. The number of layers used for this neural network modeling was three, *i.e.*, an input layer, one or two hidden layers and an output layer. As can be seen from Fig. 2, two neurons were used in the input layer, *i.e.*, the mV and volume of the titrant (ml), and those of the hidden layer were optimized for each solution of the agents and mixtures. The titrant volume and mV value of the solution were considered as independent variables of the potentiometric titration method. Therefore, these variables were used as input variables in the network architecture.

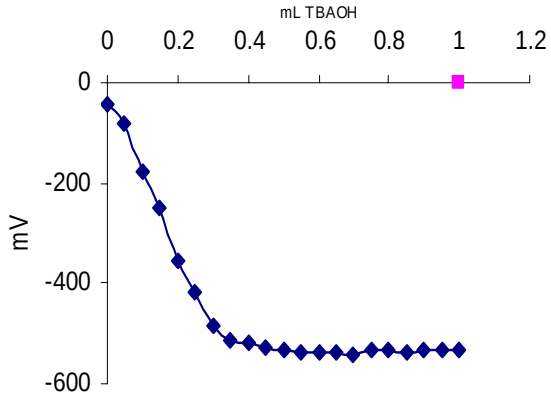


Fig. 4. Titration curves for equimolar ternary mixtures with tetrabutylammonium hydroxide as titrant.

Various neural network models, which have the logistic function, were trained and tested. In this step, the number of the hidden layer units of the network was determined by performance evaluation of the network models, defined in Table I. According to the RMS errors given in Table I, the NN5 2-16-8-3 model which performs best on a testing data set was selected as neural network model to predict the concentrations of the agent.

TABLE I. Comparison of the performances of the neural network models

| Model | RMS error | | | | | |
|---|---|---|---|---|---|---|
| | Ibuprofen | | Indomethacin | | Naproxen | |
| | Training | Testing | Training | Testing | Training | Testing |
| NN1 2-7-3 | 0.000949 | 0.001031 | 0.001035 | 0.00332 | $5.31135\times10^{-5}$ | 0.001021 |
| NN2 2-11-3 | 0.00095 | 0.00107 | 0.000998 | 0.099649 | 0.00077 | 0.001027 |
| NN3 2-13-3 | 0.000904 | 0.001024 | 0.000977 | 0.001474 | 0.000733 | 0.001434 |
| NN4 2-16-5-3 | 0.000795 | 0.045128 | 0.000816 | 0.157202 | 0.000671 | 0.04828 |
| NN5 2-16-8-3 | 0.000624 | 0.00022 | 0.000708 | 0.00017 | 0.000673 | 0.00088 |

Parity plots of the predicted values of the acid concentrations from the NN5 model and those experimentally observed for the training data set are shown in Fig. 5. The correlation between the outputs of the NN5 model and the target values from the actual values for the testing data set are presented in Fig. 6. Predictions with a RMS error of less than 0.001 for all acids indicated that each agent concentration in a given solution was accurately predicted using the NN5 model. In addition, there is a good agreement between experimentally observed results and predicted results from the model structured (see Figs. 5 and 6).

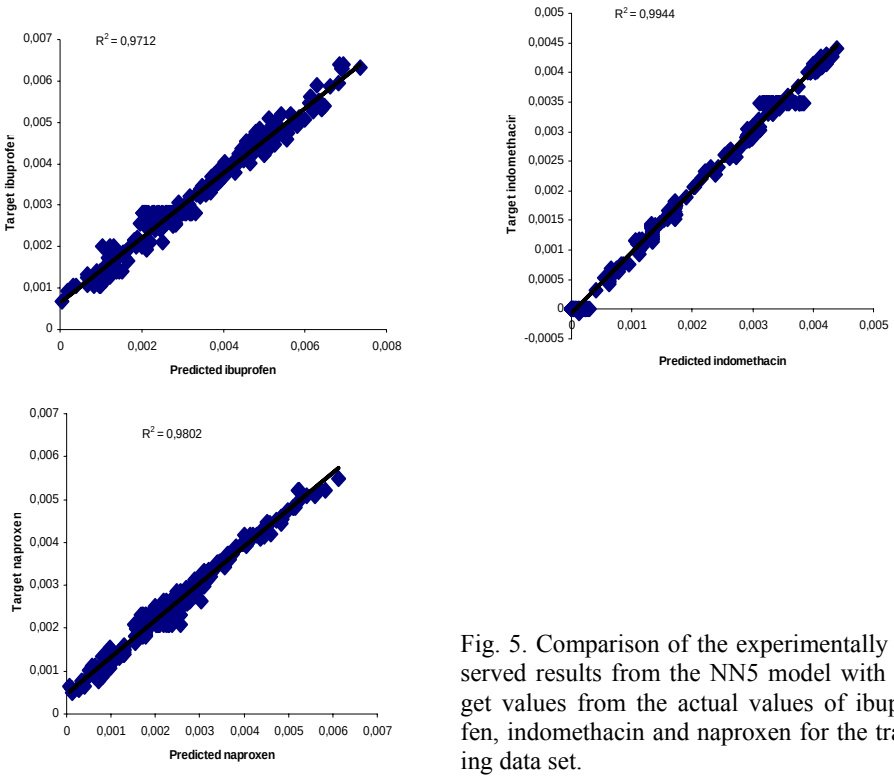


Fig. 5. Comparison of the experimentally observed results from the NN5 model with target values from the actual values of ibuprofen, indomethacin and naproxen for the training data set.

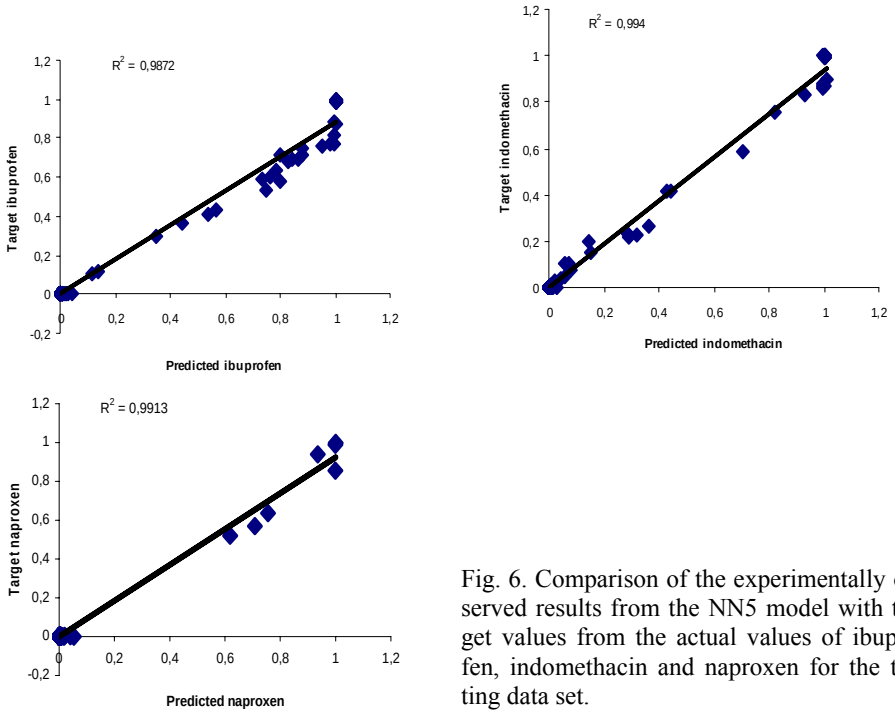


Fig. 6. Comparison of the experimentally observed results from the NN5 model with target values from the actual values of ibuprofen, indomethacin and naproxen for the testing data set.

Furthermore, several additional solutions were prepared and titrated to validate the selected model. Experimental results and estimated results from the model are given in Table II, from which it can be seen that the error in the obtained estimation was at a negligible level. The percent relative standard error of prediction varied between –7.9 and 5.6. The low average relative error of prediction (< 2.30 %) indicates that the employed networks can properly process the titration data and model the complex relationship between the concentration of the agents in the mixture and the mV data at different volumes of the titrant.

TABLE II. Statistical parameters calculated for the prediction set using the optimized neural network models

| | Agent mixture composition | | | | | | | | |
|---|---|---|---|---|---|---|---|---|---|
| | Ibuprofen | | | Indomethacin | | | Naproxen | | |
| | Actual (mM) | Predicted (mM) | RE / % | Actual (mM) | Predicted (mM) | RE / % | Actual (mM) | Predicted (mM) | RE / % |
| 1 | 0.05 | 0.0520 | 4.0 | 0.10 | 0.1011 | 1.1 | 0.15 | 0.1484 | –1.07 |
| 2 | 0.10 | 0.0973 | –2.7 | 0.15 | 0.1508 | 0.53 | 0.20 | 0.2043 | 2.15 |
| 3 | 0.15 | 0.149 | –0.67 | 0.20 | 0.1982 | –0.9 | 0.25 | 0.2567 | 2.68 |
| 4 | 0.20 | 0.2001 | 0.05 | 0.10 | 0.1056 | 5.6 | 0.15 | 0.1501 | 0.07 |
| 5 | 0.20 | 0.2005 | 0.25 | 0.15 | 0.1573 | 4.87 | 0.10 | 0.0921 | –7.9 |

## CONCLUSION

Agent concentrations in these potentiometric titrations could be estimated by the neural network with an error which might easily be negligible. Neural network modeling was able to process the non-linear relationship between the mV of the solutions at a given volume of titrant, and predict the concentrations of the agents in unknown sample solutions. For all agents, low prediction errors (< 2.30 %) and high correlation coefficients (0.9715, 0.9944 and 0.9802 for ibuprofen, indomethacin and naproxen, respectively) emphasize the high linear relationship between the predicted and actual concentrations.

## И З В О Д

## ПОТЕНЦИОМЕТРИЈСКО ОДРЕЂИВАЊЕ ИБУПРОФЕНА, ИНДОМЕТАЦИНА И НАПРОКСЕНА ПОМОЋУ МРЕЖЕ ВЕШТАЧКИХ НЕУРОНА

A. HAKAN AKTAŞ и GÜZIDE PEKCAN ERTOKUŞ

*Department of Chemistry, Faculty of Science & Art, Süleyman Demirel University, 32260 Isparta, Turkey*

Три против-упална чиниоца, ибупрофен, индометацин и напроксен, титрована су у овом раду потенциометријски тетрабутиламонијум-хидроксидом у ацетонитрилу као растварачу, у атмосфери азота на температури од 25 °C. Током процедуре потенциометријске титрације коришћен је за обраду података рачунарски програм MATLAB 7.0, као калибрациони алат са више променљивих. За моделовање комплексних, нелинеарних зависности између концентрације ибупрофена, индометацина и напроксена и миливолта (mV) раствора мерених након додавања различитих запремина титранта, примењена је мрежа вештачких неурона (ANN). Помоћу оптимизоване мреже могу се предвидети концентрације чинилаца у синтентичкој смеши. Резултати показују да се помоћу примењене ANN мреже могу проценити титрациони подаци са просечном релативном грешком процене мањом од 2,30 %.

(Примљено 14. јула 2006, ревидирано 26. јула 2007)

## REFERENCES

1. S. Garrigues, M. Gallignani, N. Delaguardia, *Talanta* **40** (1993) 89
2. S. Ravisankar, M. Vasudevan, M. Gandhimathi, B. Suresh, *Talanta* **46** (1998) 1577
3. C. S. P. Sastry, D. S. Mangola, K. E. Rao, *Analyst* **111** (1986) 323
4. *European Pharmacopoeia, 4th Edition*, HM Stationery Office, 2002, pp. 1032–1033, 1359–1360, 1367–1368 and 1617–1618.
5. A. M. Gerakis, M. A. Koupparis, C. E. Efstathiou, *J. Pharm. Biomed. Anal*. **11** (1993) 33
6. C. S. P. Sastry, A. R. M. Rao, *Analysis* **15** (1987) 569
7. P. Nagaraja, R. A. Vasantha, H. S. Yathirajan, *J. Pharm. Biomed. Anal*. **31** (2003) 563
8. A. Campliglio, *Analyst* **123** (1998) 1571
9. M. Fillet, L. Fotsing, J. Bonnard, J. Crommen, *J. Pharm. Biomed. Anal*. **18** (1998) 799
10. A. Guttman, N. Cooke, *J. Chromatogr. A* **685** (1984) 155
11. P. Damiani, M. Bearzotti, M. A. Cabezon, *J. Pharm. Biomed. Anal*. **29** (2002) 229
12. J. H. Satterwhite, F. D. Bourdinat, *J. Chromatogr. Biomed. Appl*. **431** (1988) 444
13. M. Y. Hyun, M. S. Na, C. S. Min, *J. Chromatogr. A* **732** (1996) 209
14. D. A. Skoog, D. M. West, F. J. Haller, *Analytical Chemistry, Sixth Edition*, Saunders College Publishing, 1994, p. 354

15. A. H. Aktaş, S. Yaşar, *Chim. Acta Slov*. **51** (2004) 273
16. O. Çakırer, E. Kılıç, O. Atakol, A. Kenar, *J. Pharm. Biomed. Anal*. **20** (1999) 19
17. G. Gonzales, R. Ventura, A. K. Smith, R. Torre, J. Segura, *J. Chromatogr. A* **719** (1996) 251
18. M. J. Arcos, M. C. Ortiz, B. Villahoz, L. A. Sarabia, *Anal. Chim. Acta* **339** (1997) 63
19. A. H. Aktaş, G. Pekcan, *Asian J. Chem*. **18** (2006) 2025
20. D. B. Strickmann, G. Blaschke, *J. Pharm. Biomed. Anal.* **25** (2001) 974
21. S. Yılmaz, B. Uslu, S. A. Özkan, *Talanta* **54** (2001) 351
22. N. M. El Kousy, *J. Pharm. Biomed. Anal*. **20** (1999) 185
23. R.T. Sane, M. Francis, A.R. Khatri, *J. Planar Chromatogr.-Mod. TLC* **11** (1998) 211
24. Y. Özkan, N. Doğanay, N. Dikmen, A. Işımer, *Farmaco* **55** (2000) 433
25. X. Y. Wang, F. Cui, Y. Yonezowo, H. Sumado, *Chem. Pharm. Bull.* **51** (2003) 772
26. M. M. Sena, C. B. Freitas, L. C. Silva, C. N. Perez, Y. O. Poulo, *Quim. Nova* **30** (2007) 75
27. T. Okumura, M. Nakazono, M. Otsuko, K. Tokayono, *Colloids Surf., B* **49** (2006) 153
28. T. Okumura, M. Otsuko, *Pharm. Res.* **22** (2005) 1350
29. E. Dinç, A. Özdemir, H. Aksoy, Ö. Üstündağ, D. Balenou, *Chem. Pharm. Bull.* **59** (2006) 415
30. M. Kim, H. Chung, Y. Woo, M. Kemper, *Anal. Chim. Acta* **579** (2006) 209.

Journal of the Serbian Chemical Society
JSCS@tmf.bg.ac.yu • www.shd.org.yu/JSCS
*J. Serb. Chem. Soc.* *73* (1) 97–111 (2008) UDC 546.284–31:539.23:621.928.46+542.9+543.4
*JSCS–3691* *Original scientific paper*

# The charge percolation mechanism and simulation of Ziegler–Natta polymerizations. Part VII. Effects of the distribution of chromium active centers on silica on the polymerization of ethylene

DRAGOSLAV STOILJKOVIĆ[1*#], BRANKA PILIĆ[1], MIŠA BULAJIĆ[2], NEBOJŠA ĐURASOVIĆ[2] and NIKOLAJ OSTROVSKII[3]

[1]*Faculty of Technology, University of Novi Sad, Bul. Cara Lazara 1, 21000 Novi Sad,* [2]*HIP-Petrohemija, 26000 Pančevo and* [3]*HIPOL, 25250 Odžaci, Serbia*

(Received 22 September 2006, revised 13 June 2007)

*Abstract*: The charge percolation mechanism (CPM) of olefin polymerization in the presence of transition metal compounds has been applied to explain the polymerization of ethylene by silica supported chromium oxide. In the previous work of this series, the fundamental issues and mechanism of this polymerization were presented. In this work the compatibility of the CPM with the empirical findings is confirmed. The CPM has been applied to explain: the appearance of an induction period; the deactivation of active centers and the formation of oligomers; the effects of chromium concentration on the silica surface, the silica surface discontinuity and the pore size of silica on polymerization and the formation of the structure of polyethylene. A mathematical model has been derived to explain the effects of the $CrO_x/SiO_2$ ratio on the productivity of Phillips catalysts in the polymerization of ethylene. The empirical findings have also been confirmed by computer simulations.

*Keywords*: ethylene polymerization; Phillips $CrO_x/SiO_2$; charge percolation mechanism.

## INTRODUCTION

Despite the fact that ethylene polymerization by silica supported chromium oxide was discovered some fifty years ago[1] and has attracted a great deal of academic and industrial research, there are still many open questions concerning: (1) the oxidation state of an active center, (2) the mechanisms of initiation, (3) the mechanism of polymerization, (4) the physico–chemical state of Cr species at the silica, (5) the polymerization kinetics, particularly the occasional appearance of an induction period, (6) the origin of the structure and very broad molecular

* Corresponding author. E-mail: dragos@uns.ns.ac.yu
# Serbian Chemical Society member.
doi: 10.2298/JSC0801097S

weight distribution (MWD) of PEHD, (7) the role of silica and the correlation of its properties with the results of polymerization.

Hence, in the previous work of this series,[2] the fundamental issues of ethylene polymerization by silica supported chromium oxide were analyzed and the charge percolation mechanism (CPM), which has recently been applied to explain olefin polymerization by other Ziegler–Natta transition metal complexes, was suggested. It was explained that starting from Cr precursors, after their immobilization on the silica, thermal treatment and the addition of ethylene (or CO), various immobilized Cr(II) and Cr(IV) species are produced, which exist simultaneously at the $SiO_2$ (Scheme 1). These species, Cr(IV) and Cr(II), are unstable. There is a tendency to equalize their oxidation states to Cr(III) by charge transfer from Cr(II) to Cr(IV), but this cannot occur since they are immobilized and highly separated on the support. The immobilized Cr(II) to Cr(IV) species on the support are gradually surrounded by an adsorbed monomer film (Scheme 1, top). A cluster of monomers, with overlapping π-bonds, connects the two immobilized Cr species. Once a bridge is completed (the percolation moment), a charge transfer occurs. The whole π-electron cloud in the monomer cluster will be pulled toward the Cr(IV), since it has a more positive charge than Cr(II). This displacement of π-electrons attracts a proton from an alkyl group of a Cr(IV) to the terminal monomer molecule, leaving an electron pair on the alkyl group. Simultaneously, a partially positive charge is formed on the terminal monomer molecule coordinated to Cr(II), a proton from the terminal monomer molecule is repelled to Cr(II). The electron pair, left on the terminal monomer molecule, enables the simultaneous polymerization of all the monomer molecules forming the bridge between Cr(II) and Cr(IV). Both Cr species equalize their oxidation states simultaneously with the polymerization of monomer (Scheme 1, bottom). The polymer chain is removed from the support making its surface free for subsequent monomer adsorption. The whole process is repeated by the oxidation–reduction of another Cr(II)–Cr(IV) ensembles immobilized on the support.

$$[\mathbf{Cr(II)}\cdots CH_2{=}CH_2\cdots(CH_2{=}CH_2\cdots)_n CH_2{=}CH_2\cdots\mathbf{Cr(IV)}\cdots(CH_2{=}CH_2)]/\mathbf{SiO_2} \rightarrow$$
$$\rightarrow [H{-}\mathbf{Cr(III)}\cdots\cdots\cdots\cdots\mathbf{Cr(III)}{-}CH{=}CH_2]/\mathbf{SiO_2} +$$
$$+ CH_2{=}CH{-}(CH_2{-}CH_2)_n{-}CH_2{-}CH_3$$

Scheme 1.

In the previous work,[2] using this mechanism, the answers to questions (1) to (4) cited above were given. The aim of this article is to show that the CPM is compatible with the empirical findings and to give the answers to the remaining questions (5) to (7) listed above. The origins of the induction period, as well as the effects of the distribution of Cr on the silica support on the productivities of Cr and silica are presented.

## COMPATIBILITY OF THE CPM WITH EMPIRICAL FINDINGS

### *Induction period*

An induction period has been noticed in some cases, *i.e.,* when the ethylene and the activated $CrO_x/SiO_2$ came into contact, the polymerization did not commence immediately or it started very slowly and increased with time.[3] For example, Cr(VI) oxide/silica is not immediately active after being charged into the reaction medium which had previously been saturated by ethylene.[4,5] An induction time up to 80 min has been reported and then the rate of polymerization gradually increased during the run. It was explained that the induction time was probably due to the slow reduction of Cr(VI) by ethylene to an active lower valence species and the increase in rate due to the slow alkylation step. On the contrary, if $Cr(II)/SiO_2$, obtained by the reduction of Cr(VI) by CO, is brought to contact with ethylene, the polymerization commences almost immediately.[6,7] Also, organochromium(II) catalysts come on stream immediately, because they are already reduced and alkylated.

These empirical findings are quite compatible with the CPM which requires Cr(IV)–Cr(II) ensembles to be present on the silica. The transformation Cr(VI) $\rightarrow$ $\rightarrow$ Cr(IV) $\rightarrow$Cr(II) by ethylene is a slow process performed initially by the partially breaking of two C=O bonds and one C=C bond, followed by the complete breaking of the two remaining C−O bonds and one C−C bond (Fig. 1 in Ref. 2).

In the case of CO pre-reduced Cr precursors, the coordination of ethylene molecules with the pre-formed Cr(II) ions, their alkylation and oxidation (ethylene + Cr(II) $\rightarrow$ R−Cr(IV)) are fast processes since only one C=C bond has to be partially broken to a C−C bond (Fig. 2 in Ref. 2). Furthermore, the initial surface concentration of Cr(II) ions is high and the average distance between the residual Cr(II) ions and the just formed R−Cr(IV) ions is low. A small amount of ethylene has to be adsorbed to produce Cr(IV) ions and to build a monomer bridge between the just formed Cr(IV) ions and the surrounding residual Cr(II) ions. Hence, the polymerization commences without an induction period, even if the silica coverage by ethylene is low.

According to the CPM, the sequence of the appearance of the percolation participants on the support has a great effect on the polymerization.[8] In the case of Cr(VI) precursors, almost complete silica coverage by ethylene has to be achieved before the Cr(II)−Cr(IV) ensembles are formed and the polymerization begins. This sequence can be classified as an SMA, *i.e.*, support + monomer monolayer formation + active centers ensemble formation. The sequence in the case of CO reduced precursors can be classified as an SAM, *i.e.*, support + active centers formation + monomer monolayer formation.

The entropy of adsorbed ethylene decreases with increasing coverage, achieving a minimum value at full coverage.[9] It can be concluded that the higher the entropy of adsorbed ethylene, the shorter is the induction time. Exactly the same

effect of ethylene entropy on the induction time has been confirmed in the case of high pressure, free radical polymerization of ethylene.[10] Furthermore, it is a general rule in the theory of organized monomer polymerization, proposed by Kargin and Kabanov,[11] that the induction time increases with increasing monomer organization.

*Deactivation of active centers and formation of oligomers*

According to the CPM, Cr(II) is an electron donor (**D**) and Cr(IV) is an electron acceptor (**A**). They are immobilized and separated on the support (Fig. 1a). Monomer molecules are gradually adsorbed making a bridge between **A** and **D** (Fig. 1b). No polymer is formed until the bridge between some **A** and **D** is completed. A critical moment appears when the last monomer is adsorbed, thus completing the bridge (at site **P,** Fig. 1c). Such processes are analyzed by the theory of critical phenomena, particularly by the percolation theory.[12]

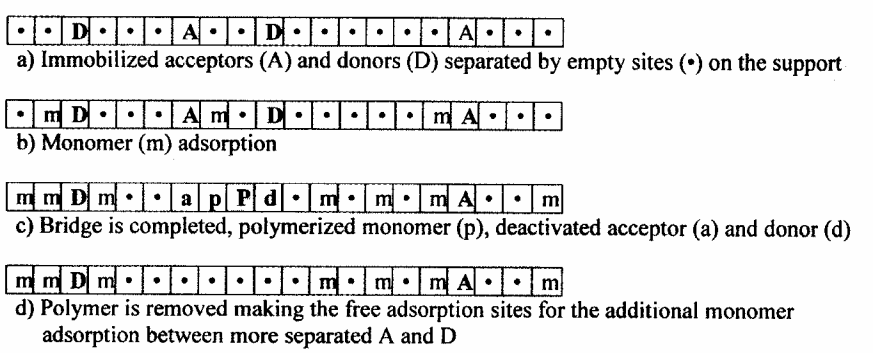


Fig. 1. Phases of an elementary percolation step of an SAM sequence presented on a segment of a support adsorption row.[8,13] (In this case **A** = Cr(IV), **D** = Cr(II) and **a,d** = Cr(III)).

According to the CPM, the very first bridges have to be formed between an **A** and **D** which are situated close to each other on the support surface (Fig. 1a–c). Subsequently, more separated **A** and **D** sites will be included in the process (Fig. 1d). Consequently, oligomers with a low degree of polymerization ($X_n$) will be obtained initially, but $X_n$ should increase with increasing polymerization time.[8,13] Simultaneously, the number of active centers (**A** and **D**) remaining on the support should decrease. Experimental data[14] confirmed such predictions of the CPM (Fig. 2, left).

The described processes were computer simulated using the Monte-Carlo method.[13] Two dimensional percolation processes were simulated. (The computer simulation of ZN polymerization by the CPM is explained elsewhere.[8,15]) In the simulation, the Cr(II) and Cr(IV) ions (160000 each) were initially randomly distributed over a part of the support containing $16\times10^6$ adsorption sites arranged in a hexagonal lattice. Then, ethylene was introduced which gradually

and randomly adsorbed on the empty sites. The Cr(II) and Cr(IV) ions were surrounded by growing monomer clusters at the surface. Occasionally, a monomer bridge connects some Cr(II) ion with some Cr(IV) ion. According to the CPM, both ions are transformed to Cr(III) and deactivated. Simultaneously, the monomer molecules of the bridge polymerize and detach from the support. The simulation enables the effects of the quantity of ethylene molecules added to the silica on the change of degree of polymerization and the number of active centers, *i.e.*, Cr(II) and Cr(IV), remaining on the silica to be observed The results of the computer simulation based on the CPM have the same trends as the experimental data (Fig. 2, right). (The numbers of Cr ions and adsorption sites used in the simulations were high enough for reproducible simulations. They were, however, too low in comparison with the real values, since one gram-atom of Cr has $6.023\times10^{23}$ atoms and one gram of silica has several hundreds of square meters, *i.e.*, $\approx 10^{20}$ adsorption sites for ethylene molecules. Hence, the results of simulation can show only the trends of the various effects but not the real values.)

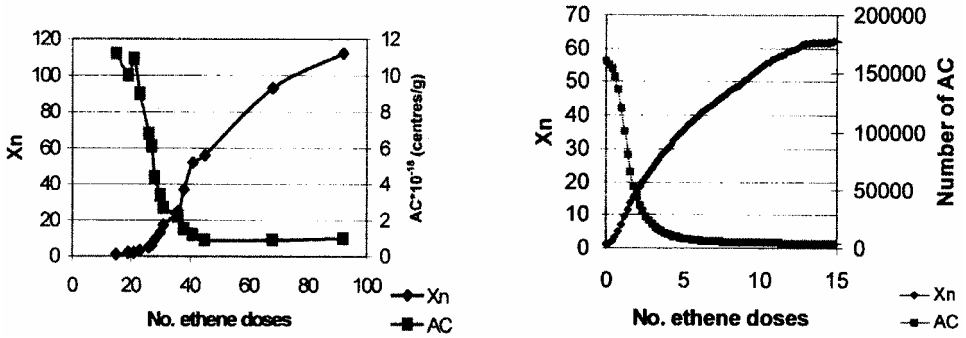


Fig. 2. The mean $X_n$ of ethylene oligomers and the concentration of active centers (AC = Cr(II) + + Cr(IV)) as a function of the quantity of adsorbed ethylene on $CrO_x/SiO_2$. (Left – experimental data;[14] right – simulation based on the CPM).

*Effects of chromium concentration on the silica surface on the polymerization activity*

The distance between Cr atoms on the silica is in relation to its surface concentration (Fig. 3). Hogan calculated that the distance between the Cr ions decreased from 16 to 0.65 nm with increasing Cr loading from 0.01 to 6.0 wt. % on a silica having a surface area of 300 $m^2\ g^{-1}$ (Table 5 in Ref. 16). The surface concentration ($Cr_S$) and the average distance between the Cr atoms ($L$) on a support having a specific surface area ($S$) can be calculated by the simple Equations (1−3), which give the same values as those presented by Hogan:

$$Cr_S = Cr_0N/AS \quad (1)$$

$$S_{Cr} = 1/Cr_S \quad (2)$$

$$L = (1/Cr_S)^{0.5} \quad (3)$$

where $Cr_S$ (Cr atoms per $m^2$ of support) is the number of Cr atom per unit area of support; $Cr_0$ (g Cr per g catalyst) is the initial mass fraction of Cr in the $Cr/SiO_2$ precursor; $N$ is Avogadro's number; $A$ is the atomic mass of Cr; $S$ ($m^2$ of support per g catalyst) is the specific surface area of the support; $S_{Cr}$ ($m^2$ of support per Cr atom) is the support surface area occupied by one Cr atom; $L$ (m per Cr atom) is the average distance between two Cr atoms on the support.

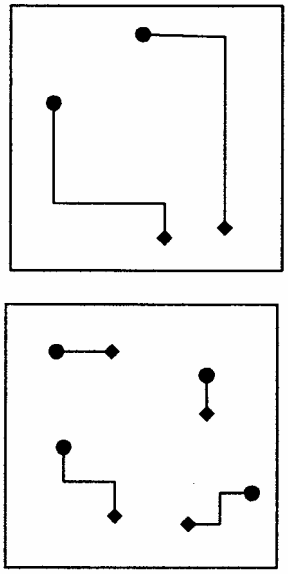

Fig. 3. The percolation path lengths between Cr(II) (•) and Cr(IV) (♦) ions for a low (top) and for a high (bottom) Cr loading.

The productivity of such a catalyst in ethylene polymerization was experimentally determined and presented as chromium productivity ($P_{Cr}$) and support productivity ($P_S$), *i.e.*, the quantity of polyethylene produced per unit of Cr and per unit of support, respectively. It was found experimentally that $P_{Cr}$ decreased but $P_S$ increased with increasing content of Cr in the $SiO_2$ (Fig. 4, top).[16] Hogan explained that $P_{Mt}$ decreased since there was a competition for monomer insertion between two Cr ions if the distance between them was very small.

These experiments, however, can be better explained and predicted by the CPM. It is known[14,18,20] that only a small fraction ($f$) of loaded $Cr_0$ become an active center, *i.e.*, $f = Cr_{activated}/Cr_0 = 0.001 - 0.004$. According to Relations (1–3), the average distance between the active centers ($L_a$), *i.e.*, Cr(II) and Cr(IV), is given by Relation (4):

$$L_a = [AS/(fCr_0N)]^{0.5} \tag{4}$$

The polyethylene yield (g PE per g catalyst) is given by:

$$P = n_p X_n M_{Et}/N \tag{5}$$

where $n_p$ is the number of polyethylene chains per one gram of catalyst; $X_n$ the average degree of polymerization, *i.e.*, the average number of ethylene molecules per one polymer chain; $M_{Et}$ is the molecular mass of ethylene (28 g mol$^{-1}$).

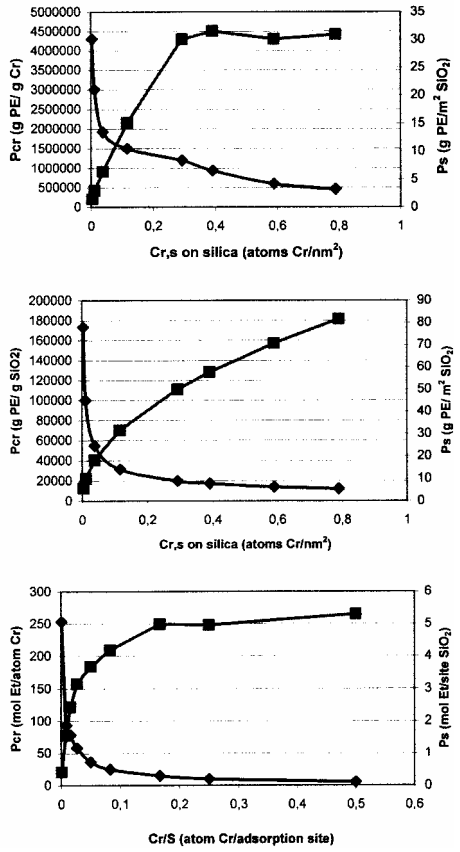


Fig. 4. Chromium (♦) and silica (■) productivities; top – experimental data,[16] middle – calculated by Eqs. (10–11) using $K$ = 10000 (arbitrary value) and bottom – computer simulation (SMA sequence).

According to the CPM, two active centers are deactivated for each polymer chain. Hence the number of polymer chains ($n_p$) is given by Relation (6). $X_n$ is proportional to the distance $L_a$ between the active centers, Relation (7):

$$n_p = fCr_0N/2A \tag{6}$$

$$X_n = kL_a \quad (k \text{ is a coefficient of proportion}) \tag{7}$$

The productivities of chromium, $P_{Cr}$, (g PE per g Cr) and silica, $P_S$, (g PE per m$^2$ $SiO_2$) are:

$$P_{Cr} = P/Cr_0 \tag{8}$$

$$P_S = P/S \tag{9}$$

From Eqs. (4–7), one can derive:

$$P_{Cr} = (kM_{Et}/2)\,(f/AN)^{0.5}(S/Cr_0)^{0.5} = K(S/Cr_0)^{0.5} \tag{10}$$

$$P_S = (kM_{Et}/2)(f/AN)^{0.5}(Cr_0/S)^{0.5} = K(Cr_0/S)^{0.5} \quad (11)$$

where

$$K = (kM_{Et}/2)(f/A\,N)^{0.5} \quad (12)$$

In Eqs. (10–12), only the coefficients $k$ and $f$ are unknown. The plots of the calculated $P_{Cr}$ and $P_S$ (Fig. 4, middle) show the same trends as the experimental ones (Fig. 4, top), using Hogan's[16] experimental values for $Cr_0$ from 0.01 to 6.0 wt. % and $S = 300$ m$^2$ g$^{-1}$ $SiO_2$ and an arbitrary value for $K$ of 10000.

The here derived mathematical formulas are based on the assumptions that all active centers are initially present (SAM sequence) and that the average distances between them do not change during the polymerization. These assumptions are not realistic for the experimental data[16] discussed here. Hence, computer simulations were performed using the SMA sequence of active centers and the monomer appearance on the support. The results of simulations (Fig. 4, bottom) show similar trends as the calculated and as the experimental results.

According to experimental experience, the simplified Formulas ((10) and (11)) and the computer simulation based on the CPM, a high chromium productivity, $P_{Cr}$, is achieved at low concentrations of chromium and high surface areas of silica.

*Effects of silica surface discontinuity on polymerization activity*

The more separated are the Cr active centers on silica, the higher is $P_{Cr}$. There is, however, a maximum distance between the Cr(II)–Cr(IV) ensembles which can be bridged by adsorbed monomer. The huge surface area of any silica particle is divided into smaller regions. These regions are separated by pore walls, dislocations and other types of surface imperfections, which make obstacles producing discontinuities in the adsorbed monomer monolayer. The monomer molecules can make a bridge only between those Cr(II) and Cr(IV) ions belonging to the same region. Such phenomena have been explained by the theory of active center ensembles proposed by Kobozev,[19] as a general theory in catalysis. This theory was modified and applied to explain Z–N polymerizations.[15,20] An outline of this concept and its application to explain ethylene polymerization by $CrO_x/SiO_2$ precursors will be presented here.

According to the concept of Kobozev, a critical factor is the number of active centers per one region. A schematic presentation of the Cr active centers in two regions, *i.e.*, two pores of silica, is presented in Fig. 5. Each region behaves as an individual "micro-reactor" containing a definite number of active centers. In a case of very high concentrations of active centers (Fig. 5a), according to Eqs. (10) and (11) $P_{Cr}$ should be low while $P_S$ should be high. Decreasing the number of active centers number contributes to an increase of $P_{Cr}$ and a decrease of $P_S$. According to Kobozev and the CPM,[15] there is an optimal number of active center ensembles (Fig. 5b), contributing to the maximum of $P_{Cr}$. When the number of Cr active centers is very low (Fig. 5c), some regions become inactive because

they contain only one or no active center. Hence, the CPM and the Kobozev theory predict that the values of $P_{Cr}$ and $P_S$ should decrease at the very low concentrations of chromium. This effect has been investigated by computer simulation[8,13,15] (Fig. 6, top) and predicted by a very simple calculation.[13] A sharp maximum of metal productivity ($P_{Mt,max}$) is obtained[15] if the number of active centers is 3 or 5 per surface region in the SAM sequences of one- and two-dimensional percolation processes, respectively, and if the number of Mt(IV) is equal to that of Mt(II). The value of $P_{Mt,max}$ depends on the size of region, *i.e.*, the number of adsorption sites in it – the more sites, the higher is $P_{Mt,max}$.

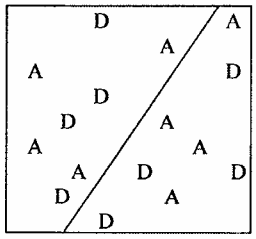


a) Very high concentration of active centers

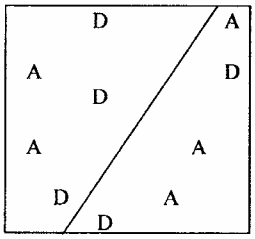


b) Optimal concentration of active centers

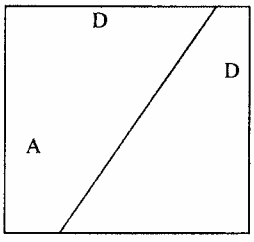


c) Very low concentration of active centers

Fig. 5. Schematic presentation of two regions, *i.e.*, two pores, with different concentrations of active centers (**D** = Cr(II) and **A** = Cr(IV), the solid lines represent the obstacles between the two regions).

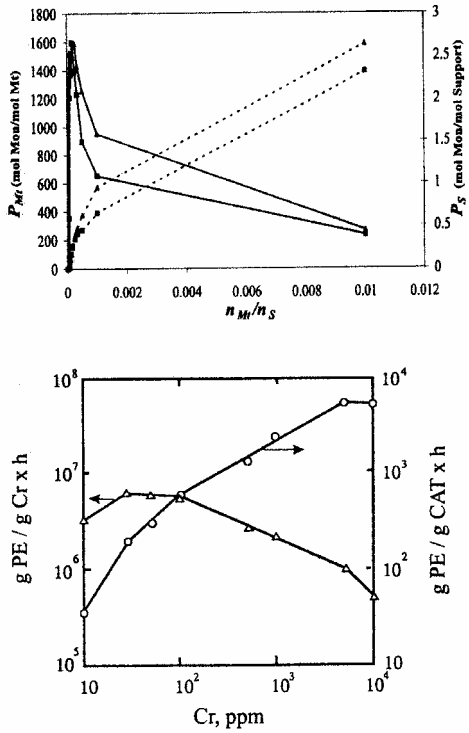


Fig 6. Effects of Mt loading on $P_{Mt}$ and $P_S$. (Top: prediction by computer simulation; $P_{Mt}$ – solid lines, $P_S$ – dotted lines, ■ – SAM and ▲ – SMA sequences; bottom: experimental data.[1] Note: The trends on the top are similar to the trends on the bottom if logarithmmic scales of the abscissa and ordinate are used instead of linear ones.).

Indeed, detailed experiments[1] on ethylene polymerization by the $CrO_x/SiO_2$ system showed that the activity per chromium atom reaches a sharp maximum ($P_{Cr,max}$) near a Cr loading of 0.005 wt % (Fig. 6, bottom), although other values have also been reported, *i.e.*, 0.01 wt %. Sharp $P_{Cr,max}$ values were obtained for Cr loadings of 3 and 5 wt % in the case of propylene polymerization.[21] The same effect was noticed in other Z–N polymerization systems.[8,13,15] Several dozens of experiments have been analyzed and explained by the Kobozev theory and by the CPM. Some examples were presented: the ethylene polymerization by $CrO_x/SiO_2$,[8] propylene polymerization by $TiCl_4/AlEt_3/MgCl_2$, by $TiCl_4/AlEt_2Cl$/graphite and by metallocene/MAO systems.[8,13,15]

*Effects of pore size of silica on the polymerization activity*

Silicas with small pores are always catalytically inferior and therefore the industrial silicas of choice have an average pore size diameter from 5 to above 20 nm.[22] For example, McDaniel[4] prepared the silicas that had a constant value of surface area (375 $m^2\ g^{-1}$) but with different pore volume size and distribution. It was shown that the activity of the finished catalyst increased with the pore volume. Using the data presented in Table II in Ref. 4, Fig. 7a was prepared to illustrate that the activity decreased with increasing volume fraction of small pores.

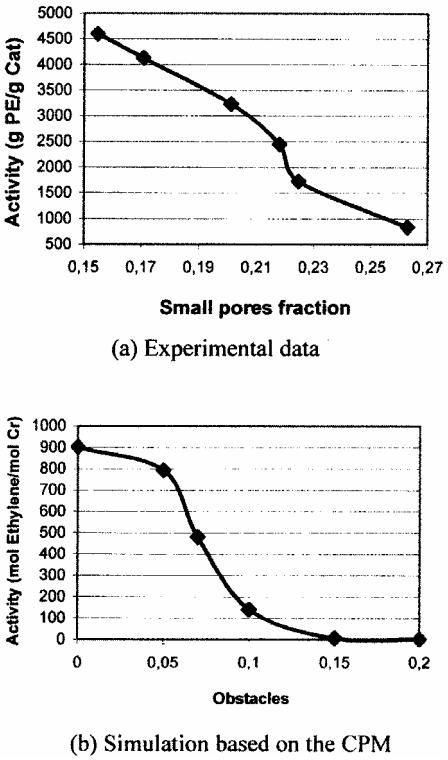


Fig. 7. Effect of a small pore fraction of the silica on the polymerization activity: (a) experimental results[4] and (b) computer simulation based on the CPM.

This phenomenon can not be explained by the insertion mechanism, which is generally accepted in Z–N polymerization. It is easy to explain it, however, by the CPM and the Kobozev theory. In the case of large pores, each of them contains a large number of active centers (Fig. 8a), which contribute to ethylene polymerization. The average number of active centers per one pore, however, decreases with increasing fraction of small pores (Fig. 8b). In the case of very small pores, some of them do not contain an Cr(II)–Cr(IV) ensemble; they are empty or contain only one type of active center, *i.e.*, only Cr(II) or only Cr(IV) (Fig. 8c). These pores and the Cr ions present in them do not contribute to the polymerization of ethylene. The pore walls make the silica surface discontinuous and form obstacles on the silica surface. Computer simulations of ethylene polymerization by the CPM give results (Fig. 7b) exhibiting the same trends as the experimental ones (Fig. 7a). The simulation was performed with 250 Cr(II) ions and 250 Cr(IV) ions randomly distributed over the silica surface with $25\times10^6$ adsorption sites, but randomly divided into regions by an increasing number of obstacles. In real silica, some pores are isolated but some pores are randomly connected and thus unifying their surface into one region. This was also taken into consideration by the computer simulation.

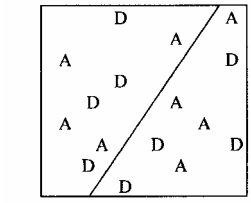

a) Active centers distribution in the very large pores

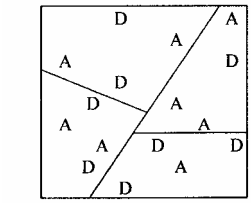

b) Active centers distribution in the medium size pores

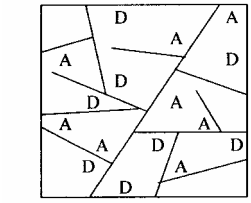

c) Active centers distribution in very small pores

Fig. 8. Schematic presentation of the distribution of active centers in large, medium and small pores (**D** = = Cr(II) and **A** = Cr(IV)).

*Polyethylene structure formation*

The many details of the polymer structure can be predicted by the CPM. The purpose of this article, however, was not to present such details, which were introduced elsewhere.[23] Only some important issues will be discussed.

The most important structural characteristics of any polymer are the number ($X_n$) and mass ($X_w$) average degrees of polymerization and the molecular mass distribution presented as the ratio $X_w/X_n$. According to the CPM, it can be predicted that $X_n$ is proportional to the length of the percolation path $L_a$ between Cr(II) and Cr(IV) sites (Fig. 3 and Eq. (7)). The value of $L_a$ is proportional to the surface area of the support ($S$) and inversely proportional to the square root of surface concentration of chromium active centers, *i.e.*, Cr(II) and Cr(IV), which depends on the chromium loading ($Cr_0$) and the fraction ($f$) of the activated chromium atoms (Eq. (4)). The computer simulations based on the CPM show that the degree of polymerization ($X_n$) has a lower value in the case of high initial concentrations of active centers (Fig. 9).

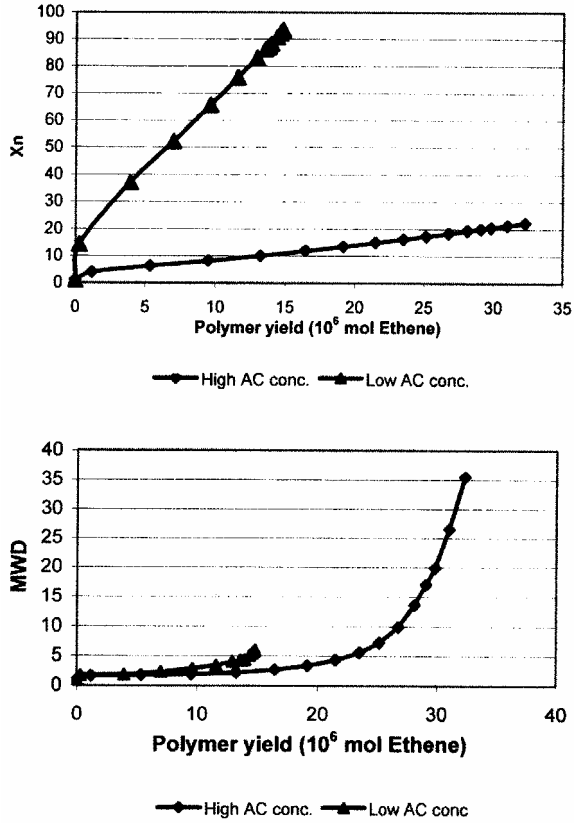


Fig. 9. Computer simulation of the effect of polymer yield on $X_n$ and MWD for high and low concentrations of active centers (AC, *i.e.*, Cr(II) and Cr(IV)).

Furthermore, according to the CPM, it can be predicted that chromium AC are consumed during the polymerization. Hence, the initial distance between the AC centers at the beginning of polymerization is low. Since the concentration of AC decreases during the polymerization, the distances between the remaining ones increase with time. Consequently, according to the CPM, $X_n$ should increase during the polymerization. These predictions have been confirmed experimenttally (Fig. 2, left) and by computer simulation (Figs. 2 and 9).

The computer simulations based on the CPM show that the $X_w/X_n$ ratio, *i.e.*, the MWD, increases with the initial concentration of AC and polymer yield (Fig. 9).

It is known that the concentration of AC increases with increasing Cr loading, the concentration of hydroxyl groups on the silica, the activation temperature, the polymerization temperature, the presence of titanium in silica, *etc*. In all these cases, the CPM predictions that $X_n$ should decrease and the MWD should be broader have been confirmed experimentally.[4]

According to the CPM, it can be predicted that the polymer chains are terminated by an unsaturated bond and a methyl group (Scheme 1). Furthermore, it can be expected that the initially formed $\alpha$-olefin oligomers can be co-adsorbed and copolymerized with ethylene, producing short and the long chain branches. These predictions have been confirmed experimentally.[24]

## CONCLUSIONS

The CPM is in good agreement with the experimental data on the ethylene polymerization by supported $CrO_x$ systems. It gives reasonable answers to all the open questions mentioned in the introduction. In the previous work of this series,[2] the answers to the questions (1) thorough (4) were given. In this work, the answers to the remaining questions, *i.e.*, (5) thorough (7), are presented. Thus, concerning question (5), there is no induction period, or it is very short, if both active centers, *i.e.*, Cr(II) and Cr(IV), are present at the initial stages of polymerization. Otherwise, some induction period is necessary for ethylene adsorption and formation of active centers, *i.e.*, reduction of Cr(VI) to Cr(IV) and to Cr(II). The concerning question (6), the broad MWD distribution of polyethylene is due to the fact that initially the charge percolation occurs between Cr(II) and Cr(IV) sites close to each other on the silica but later, more separated Cr(II) and Cr(IV) sites are included. Hence, short oligomers are formed during the initial stage, but the very long polyethylene chains are formed during the final stages of polymerization. The role of the support (question (7)) is to deform the ethylene molecules, to concentrate them, to orient them correctly and to enable their contact with Cr, thus facilitating the polymerization. Furthermore, the distribution of active chromium species on the silica surface, as well as silica surface discontinuities, has a great influence on the polymerization activity and the polyethylene structure. The predictions by the calculation and Monte-Carlo simulation based on the CPM are in the agreement with the empirical findings.

ИЗВОД

## МЕХАНИЗАМ ПОЛИМЕРИЗАЦИЈЕ ПЕРКОЛАЦИЈОМ НАЕЛЕКТРИСАЊА И СИМУЛАЦИЈА ЦИГЛЕР–НАТА ПОЛИМЕРИЗАЦИЈЕ. ДЕО VII. УТИЦАЈ РАСПОДЕЛЕ АКТИВНИХ ЦЕНТАРА ХРОМА НА СИЛИЦИЈУМ ДИОКСИДУ НА ПОЛИМЕРИЗАЦИЈУ ЕТИЛЕНА

ДРАГОСЛАВ СТОИЉКОВИЋ[1], БРАНКА ПИЛИЋ[1], МИША БУЛАЈИЋ[2], НЕБОЈША ЂУРАСОВИЋ[2] и НИКОЛАЈ ОСТРОВСКИ[3]

[1]*Tehnolo{ki fakul tet, Univerzi tet u Novom Sadu, Bulevar Cara Lazara 1, 21000 Novi Sad,* [2]*HIP–Petrohemija, 26000 Pan~evo i* [3]*HIPOL, 25250 Oxaci*

Механизам перколације наелектрисања (CPM) за полимеризацију олефина у присуству једињења прелазних метала је примењен за тумачење полимеризације етилена помоћу оксида хрома који је нанет на силицијум диоксид. У претходном раду ове серије приказане су основне поставке и механизам полимеризације. У овом раду је потврђена сагласност CPM са емпиријским налазима. Механизам перколације наелектрисања је примењен за објашњење: појаве индукционог периода; деактивације активних центара и образовање олигомера; утицаја концентрације хрома на силицијум диоксиду, дисконтинуитета површине и величине пора силицијум диоксида на полимеризацију и настајање структуре полимера. Изведен је математички модел који објашњава утицаје односа $CrO_x/SiO_2$ на продуктивност Филипсових катализатора за полимеризацију етилена. Емпиријски резултати су, такође, потврђени компјутерским симулацијама.

(Примљено 22. септембра 2006, ревидирано 13. јуна 2007)

## REFERENCES

1. P. Hogan, *J. Polym. Sci. A-1* **8** (1970) 2637
2. D. Stoiljković, B. Pilić, M. Bulajić, N. Đursović, N. Ostrovski, *J. Serb. Chem. Soc*. **72** (2007) 1155
3. E. Groppo, C. Lamberti, S. Bordiga, G. Spoto, A. Zecchina, *Chem. Rev*. **105** (2005) 115
4. M. P. McDaniel, *Adv. Catal*. **33** (1985) 47
5. M. P. McDaniel, D. R. Witt, E. A. Benham, *Ind. Eng. Chem. Res*. **27** (1988) 1559
6. E. Groppo, C. Prestipino, F. Cesano, F. Bonino, S. Bordiga, C. Lamberti, P. C. Rhune, J. W. Niemantsverdriet, A. Zecchina, *J. Catal*. **230** (2005) 98
7. M. Terano, in *Catalytic Olefin Polymerization*, *International Olefin Polymerization Conference*, Russian Academy of Science, Moscow, 2004, Ch. O7
8. D. Stoiljković, B. Pilić, S. Jovanović, D. Panić, in *Current Achievements on Heterogeneous Olefin Polymerization Catalysts*, M. Terano, Ed., Sankeisha Co., Nagoya, 2004, p.135 (Part I of this work)
9. K. L. Mentell in *Ethylene and Its Industrial Derivates*, S. A. Miller, Ed., E. Benn, London, 1969, Ch. 7
10. D. Stoiljković, S. Jovanović, *Angew. Makromol. Chem*. **106** (1982) 195
11. V. A. Kargin, V. A. Kabanov, *Zh. Vses. Khim. Ob*. **9** (1964) 602
12. A. L. Efros, *Physics and Geometry of Disorder – Percolation Theory*, Mir, Moscow, 1986
13. D. Stoiljković, B. Pilić, R. Radičević, I. Bakočević, S. Jovanović, D. Panić, Lj. Korugić–Karasz, *Chem. Ind.* **58** (2004) 479
14. M. Kantcheva, I. G. Dalla Lana, J. Szymura, *J. Catal*. **154** (1995) 329
15. 15. B. Pilić, D. Stoiljković, I. Bakočević, S. Jovanović, D. Panić, Lj. Korugić–Karasz, in *New Polymeric Materials*, Lj. Korugić–Karasz, W. MacKnight and E. Martuscelli, Eds., ACS Symp. Series, New York, 2005, p. 215 (Part II of this work)

16. P. J. Hogan, in *Applied Industrial Catalysis*, Vol. 1, B. E. Leach, Ed., Academic Press, New York, 1983, Ch. 6
17. K. H. Theopold, *Eur. J. Inorg. Chem*. (1998) 15
18. J. Boor, *Ziegler–Natta Catalysts and Polymerizations*, Academic Press, New York, 1979
19. N. I. Kobozev, *Zhourn. Fiz. Khim*. **13** (1939) 1
20. B. Pilić, D. Stoiljković, I. Bakočević, S. Jovanović, D. Panić, Lj. Korugić–Karasz, *J. Serb. Chem. Soc.* **71** (2006) 357 (part III of this work)
21. A. Guyot, R. Spitz, in *History of Polyolefins*, R. B. Seymour, Ed., Riedel Publ., Dordrecht, 1986, Ch. 16
22. B. M. Weckhuysen, R. A. Schoonheydt, *Catal. Today* **51** (1999) 215
23. B. Pilić, D. Stoiljković, I. Bakočević, S. Jovanović, D. Panić, Lj. Korugić–Karasz, *Mat. Sci. Forum.* **518** (2006) 381 (Part IV of this work)
24. P. D. Smith, M.P. McDaniel, *J. Polym. Sci. A* **27** (1989) 2695.

Journal of the Serbian Chemical Society
JSCS@tmf.bg.ac.yu • www.shd.org.yu/JSCS
*J. Serb. Chem. Soc.* *73* (1) 113–119 (2008) UDC 539.42:669.141.24:669.112.227:539.3/.5:669
*JSCS–3692* *Original scientific paper*

# Influence of cooling conditions and amount of retained austenite on the fracture of austempered ductile iron

VYACHESLAV GORYANY*, ECKART HOFMANN and PAUL JOSEF MAUK

*Institute of Applied Materials Technology (IAM), University of Duisburg-Essen, D-47048 Duisburg, Germany*

(Received 27 December 2005)

*Abstract*: SEM Analysis of fracture surfaces from tensile test specimens of thick-walled, austempered ductile irons (diameter 160 mm) shows different fracture behavior depending on the austenite retained in the matrix. The results show ductile fractures only in areas containing retained austenite sections. In section areas without or with a very low content of retained austenite, only brittle fracture without any plastic deformation occurs. The content of retained austenite determines the amount of ductile fracture in the microstructure.

*Keywords*: austempered ductile iron; retained austenite; fracture mechanism.

## INTRODUCTION

The microstructure of as-cast ductile iron has a considerable impact on the transformation process during subsequent heat treatment. The formation of the initial microstructure can be regulated *via* the chemical composition (amounts of ferrite/perlite) and inoculation (size and distribution of the graphite nodules).

Investigations[1–4] have shown that the number of graphite nodules (per mm$^2$) and other graphite-nodule parameters[2] have an important influence on the transformation kinetics and the mechanical properties of austempered ductile iron (ADI). It has become apparent that increasing the number of nodules has a mainly positive influence on the properties of the material because the undesired segregation at the grain boundaries is diminished. Another advantage of a larger number of graphite nodules is that the retention time during austenitizing is reduced. The diffusion paths for carbon are shorter, which means that higher carbon contents in the austenite can be attained in a shorter time and the process window is widened.

The austenitizing time can be shortened without any negative impact on the transformation and the carbon content in the austenite. Another positive effect of a larger number of nodules is that the austenitic–ferritic microstructure (ausfer-

* Corresponding author. E-mail: goryany@ihg.uni-duisburg.de or drgoryany@aol.com
doi: 10.2298/JSC0801113G

rite) becomes finer and more homogeneous. This in turn results in a greater strength and larger elongation after thermal treatment.[3–5]

It was found that austenitic–ferritic cast iron with nodular graphite contains 15 to 40 vol. % of stabilized austenite after thermal treatment[6,7] (sometimes more than 50 %[8]). When the transformation times are too short, the carbon content in the austenite is too low so that the austenite is unstable and may transform into martensite at room temperature and/or when exposed to stress. When subjected to higher temperatures, part of the austenite which had not been evolved in the transformation reaction may transform into martensite and/or into a tempered microstructure. This results in poorer material properties and changes of dimensions. The stability of austenite has been investigated in different ways by many authors[9–27] using different grades of alloyed iron (copper–molybdenum, copper–molybdenum–nickel). In these studies, a partial decomposition of austenite and dimensional changes were observed.[28] In these processes, the decisive influencing factor was not the content of alloying metal, but the thermal treatment.

The results obtained indicate that the content of stabilized austenite in the microstructure has a decisive impact on the mechanical properties.[11,12,16,28–31] Responding to a growing amount of austenite, the ductility, fracture strain and the notch impact energy were found to increase, with the maximum being attained at ≈ 25 % austenite.

The goal and objective of these present investigations was to study the influence of retained austenite on the fracture mechanism of ADI.

## EXPERIMENTAL

The test specimen to measure and record the time–temperature curves was a 170 mm high truncated cone with a center diameter of 160 mm into which thermocouples were integrated.

The chemical compositions of the investigated specimens as well as the associated inoculating agents are summarized in Table I.

TABLE I. Chemical composition of the employed test material and inoculating agents

| Experiment No. | Inoculating agent | Chemical composition, wt. % | | | | | | | | | |
|---|---|---|---|---|---|---|---|---|---|---|---|
| | | C | Si | Mn | P | S | Cr | Ni | Mo | Cu | Ti |
| 1, 2 | Reseed® | 3.62 | 2.38 | 0.28 | 0.024 | 0.006 | 0.036 | 2.01 | 0.39 | 0.99 | 0.01 |
| 3, 4 | Ultraseed® | 3.68 | 2.26 | 0.27 | 0.025 | 0.006 | 0.031 | 1.97 | 0.42 | 0.96 | 0.01 |

Reseed® is a strong inoculant based on a ferrosilicon alloy with 75 wt. % Si (FeSi 75) also containing calcium and rare earths. The use of this inoculating agent allowed a large number of small and uniformly distributed graphite nodules to be achieved.

With regards to its basic composition, the inoculant Ultraseed® is identical with Reseed®. However, small amounts of sulfur and oxygen are additionally added to this alloy. In this way, a good inoculation effect with medium-sized nodules and lower wall-thickness sensitivity are supposed to be obtained, even in melts with a low content of oxygen and sulfur. The tendency of shrinkage is reduced.

All specimens were austenitized for a period of 90 min at 900 °C and then quenched using different cooling media.

The specimens for test 1 and 3 were cooled with water (5 l $min^{-1}$ at a pressure of 3.6 bar) to 350 °C at the reference thermocouple level 2. The cooling rate was 1.85 K $s^{-1}$. In the next step, they were subjected to age-hardening in a furnace for 6 h at 350 °C.

The specimens for tests 2 and 4 were cooled by means of a mixture of water and air (water < 1 l $min^{-1}$ at a pressure of 1 bar; air 150 l $min^{-1}$ at a pressure of 2 bar) to a temperature of 350 °C at thermocouple level 2. The cooling rate during this test series was 1.52 K $s^{-1}$. Subsequently, the specimens underwent age-hardening treatment in a furnace for 6 h at 350 °C.

The samples for the determination of the mechanical properties and the microstructural characteristics were machined out from different levels of these specimens. The measurement of the retained austenite was made by X-ray examination. SEM Analysis of the fracture surfaces was made from the same samples.

## RESULTS AND DISCUSSION

In the samples inoculated with Reseed®, a microstructure with predominantly austenite and acicular ferrite and few parts of perlite existed on level 2 after heat treatment. In the center of sample level 4, with the lower cooling rate, a microstructure with less austenite and acicular ferrite and more perlite existed. There were segregated zones in spite of the inoculation.

In the samples inoculated with Ultraseed®, a microstructure with austenite and acicular ferrite was found level 2 after the heat treatment. In the center of the sample level 4, a microstructure with austenite and acicular ferrite and a small amount of perlite was found. There were no segregated zones. More details concerning the microstructure follow.

Depending on the employed inoculant, and hence the size and distribution of the nodular graphite, clearly different contents of retained austenite were found after comparable thermal treatment (Fig. 1).

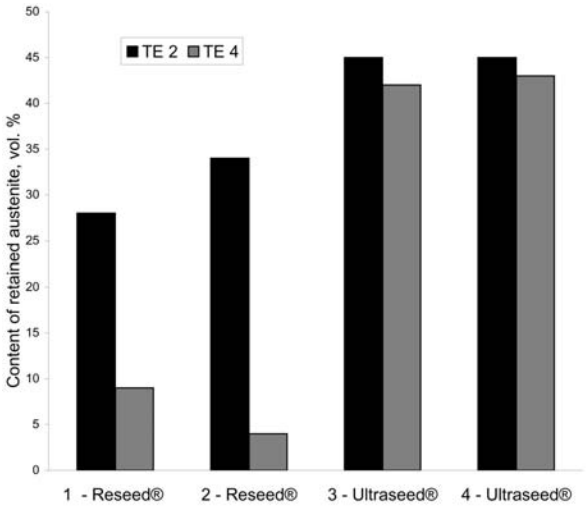


Fig. 1. Content of retained austenite at thermocouple levels 2 (TE 2) and 4 (TE 4) of the specimens subjected to different tests.

In the present case, smaller and more uniform nodules coincide with a smaller amount of retained austenite. Independent of whether water or a water–air

mixture was adopted for cooling, the use of the inoculant Reseed® leads to a smaller amount of retained austenite and a higher content of perlite. The impact of the wall thickness was very pronounced. At the level of the thermocouple TE 2 (which means more rapid cooling than on the level TE 4) the amount of retained austenite amounted to ≈ 28 vol. %, respectively 34 vol. %. Inside of the specimen center at the level of thermocouple TE 4 (a lower cooling rate compared with TE 2) the amounts of retained austenite were only 9 vol. %, respecttively 4 vol. %. The castings inoculated with Ultraseed® feature a comparable amount of retained austenite of ≈ 42 to 45 vol. %, irrespective of the cooling conditions. This result confirms the experience that the use of the sulfur- and oxygen-containing inoculant leads to a reduction of the dependence of the wall-thickness during graphite formation.

As the content of retained austenite increases, the hardness decreases (Fig. 2). All hardness values measured are within the range typical of ADI materials.

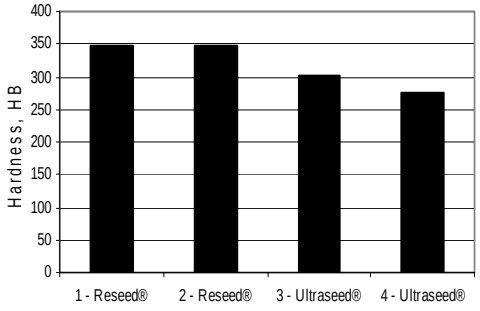


Fig. 2. Hardness values in the center zone of the specimens (TE 4).

The SEM (scanning electron microscope) analysis of the fracture surface of the tensile specimens from the center part of the castings (level 2) revealed a different crack extension as a function of the retained austenite in the basic microstructure.

Specimen 1 (thermocouple level 2) with ≈ 28 % retained austenite exhibited exclusively cleavage fracture without any signs or traces of plastic deformation (Fig. 3). This is demonstrated by the smooth plate-like to rosette-like configuration of the surface (Fig. 3b). The gap that exists between the graphite nodules and the metal matrix is probably caused by the relatively high amount of perlite in the specimen (Fig. 3a).

A further increase of the amount of retained austenite to ≈ 34 % (specimen 2, thermocouple level 2, Fig. 1) along with a corresponding reduction of the perlite content leads to mixed fracture, *i.e.*, mainly cleavage fracture with a few areas of ductile fracture (Fig. 4).

In specimens 3 and 4 (thermocouple, level 2) with an amount of retained austenite of ≈ 42 vol. %, respectively 44 vol. %, and only traces of perlite in the

basic microstructure, a distinct increase of the amount of ductile fracture is recognizable in the fracture surfaces (Fig. 5). The share of cleavage fracture is markedly smaller. These results clearly show that ductile fracture occurs only in the areas of retained austenite. The share of ductile fracture corresponds to the amount of retained austenite.

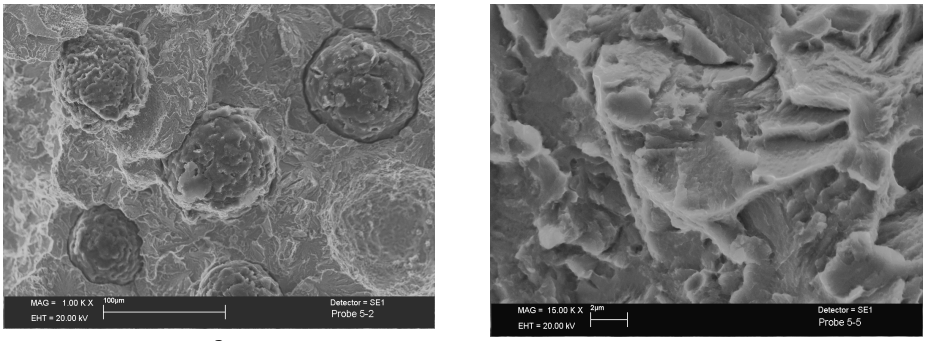


a b

Fig. 3. SEM Micrographs of the fracture surfaces of the specimen 1;
in this present case there is only cleavage fracture.

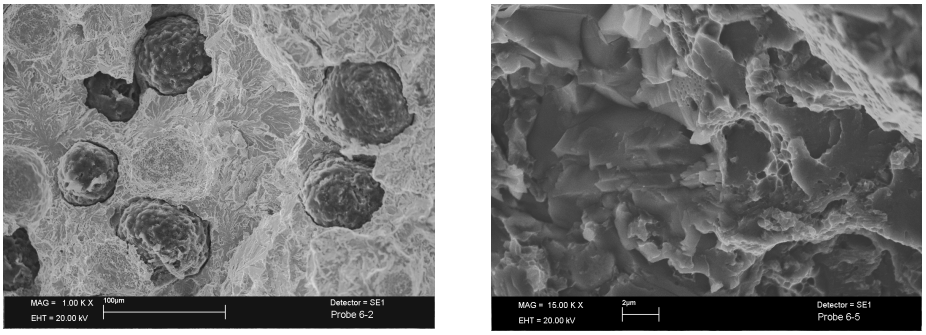


a b

Fig. 4. SEM Micrographs of the fracture surfaces of the specimen 2;
the area of the retained austenite shows ductile fracture.

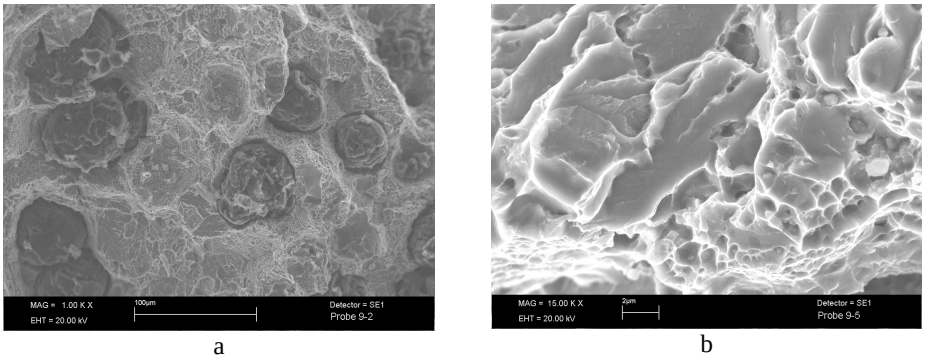


a b

Fig. 5. SEM Micrographs of the fracture surfaces of the specimen.

The existence of perlite in the microstructure seems to be the primary cause of brittle fracture behavior. It is remarkable that, responding to a growing amount of brittle fracture, the separation between the graphite nodules and the metal matrix increases.

## CONCLUSIONS

In the samples inoculated with Reseed® there was a nearly uniform nodular graphite formation over the full wall-thickness range. Under the given experimental conditions, the influence of different cooling rates on the microstructure is small. The microstructure was unfavorable for ADI.

In the samples inoculated with Ultraseed®, there were a lower nodule count and a less homogeneous nodule size over the entire cross section without segregations. This means a better microstructure for the ADI. Depending on the cooling rate, there are only traces of perlite. The influence of the cooling rate on the microstucture was slightly greater than when Reseed was employed.

The SEM analysis of the fracture surfaces from tensile test specimens of thick-walled austempered ductile irons (diameter 160 mm) showed different fracture behavior depending on the amount of austenite retained in the matrix. The results showed ductile fractures only in sections areas with retained austenite. In section areas without or with very low amount of retained austenite, only brittle fracture without any plastic deformation occurred. The content of retained austenite determines the amount of ductile fracture in the microstructure.

## И З В О Д

## УТИЦАЈ УСЛОВА ХЛАЂЕЊА И КОЛИЧИНЕ ЗАОСТАЛОГ АУСТЕНИТА НА ЛОМ АУСТЕМПЕРОВАНОГ ДУКТИЛНОГ ГВОЖЂА

VYACHESLAV GORYANY, ECKART HOFMANN и PAUL JOSEF MAUK

*Institute of Applied Materials Technology (IAM), University of Duisburg-Essen, D-47048 Duisburg, Germany*

SEM анализа површина лома узорака танкозидног, аустемперног дуктилног гвожђа тестираних на изтезање указује на различите карактеристике лома у зависности од количине аустенита заосталог у матрици. Дуктилни ломови су присутни само у областима које сардже заостале аустенитне секције. У областима са веома малим садржајем заосталог аустенита односно онима у којима није заостао аустенит јавља се крт лом без пластичне деформације. Садржај заосталог аустенита одређује удео дуктилног лома у микроструктури.

(Примљено 27. децембра 2005)

## REFERENCES

1. A. Bedolla, B. Hernandez, *Trans. Am. Foundrymens Soc.* **105** (1997) 715
2. J. Hemanth, *Mater. Sci. Technol.* **15** (1999) 878
3. G. Coopert, A. Roebuck, H. Bayati, *Int. J. Cast Metals Res.* **12** (1999) 227
4. S. Hasse, K. Röhrig, *Gießerei-Praxis* **4** (1999) 154

5. J. Liu, R. Elliott, *Int. J. Cast Metals Res.* **12** (1999) 189
6. M. P. Shebatinov, A. A. Zhukov, W. M. Kowalenko, *Vestnik Mashinostroeniya* **3** (1986) 61
7. A. A. Zhukov, *Liteinoe Proizvodstvo* **11** (2000) 28
8. A. A. Zhukov, *Liteinoe Proizvodstvo* **11** (1999) 39
9. M. N. Ahmadabadi, *Metall. Mater. Trans.* **28A** (1997) 2159
10. Th. Hirsch, P. Mayr, *Konstruieren Gießen* **18** (1993) 25
11. R. Böschen, H. Bomas, H. Vetters, P. Mayr, *Konstruieren Gießen* **15** (1990) 34
12. T. J. Marrow, H. Cetinel, C. S. Wang, H. Bayati, *20th ASM Heat Treating Conference Proceedings*, 2000, St. Louis, USA, ASM International, 2000, p. 528
13. H. Vetters, J. M. Schissler, *HTM Härterei-Technische Mitteilungen* **55** (2000) 166
14. R. Kazerooni, A. Nazarboland, R. Elliott, *Mat. Sci. Techn.* **13** (1997) 1107
15. K. Herfurth, *Konstruieren Gießen* **16** (1991) 4
16. K. Röhrig, **11** (1986) 43
17. J. L. Garin, R. L. Mannheim, *Zeitschrift für Metallkunde* **91** (2000) 841
18. P. Mayr, H. Vetters, J. Walla, *Gießereiforschung* **38** (1986) 86
19. J. M. Schissler, J. P. Chobaut, *HTM Härterei-Technische Mitteilungen* **43** (1987) 205
20. M. Johansson, *2nd International ADI Seminar*, 1994, Helsinki University of Technology, Otaniemi, SF, p. 1
21. M. Takita, Y. Ueda, K. Shibayama, H. Hiramitsu, *Physical Metallurgy of Cast Iron IV, Proceedings of the 4. International Symposium*, Tokyo, Japan, 1990, Pittsburgh, PA, USA, p. 211
22. M. Takita, Y. Ueda, K. Shibayama, H. Hiramitsu, *Physical Metallurgy of Cast Iron IV, Proceedings of the 4. International Symposium*, Tokyo, Japan, 1990, Pittsburgh, PA, USA, p. 219
23. M. Takita, *Physical Metallurgy of Cast Iron IV, Proceedings of the 4. International Symposium*, Tokyo, Japan, 1990, Pittsburgh, PA, USA, p. 227
24. K. F. Laneri, J. Desimoni, R. C. Mercader, R. W. Gregorutti, J. L. Sarutti, *Metall. Mat. Trans. A* **32A** (2001) 51
25. I. Schmidt, A. Schuchert. *Konstruieren Gießen* **13** (1988) 18
26. K. Röhrig, *Konstruieren Gießen* **13** (1988) 4
27. C. Chengija, J. J. Vuorinen, M. Johansson, *Casting 1997, International ADI and Casting Simulation Conference*, Otaniemi, Helsinki, SF, 1998, p. 1
28. J. Aranzabal, I. Gutierrez, J.M. Rodriguez–Ibabe, J. J. Urcola, *Metal. Mater. Trans.* **28A** (1997) 1143
29. T. Toshio, A. Toshihiko, T. Shuji, *Metal. Mater. Trans. A* **27A** (1996) 1589
30. S. Yamamoto, H. Yokoyama, K. Yamada, M. Niikura, *ISIJ Int.* **35** (1995) 1020
31. H. Bayati, R. Elliott, *Mater. Sci. Technol.* **13** (1997) 319.

Journal of the Serbian Chemical Society
JSCS@tmf.bg.ac.yu • www.shd.org.yu/JSCS
*J. Serb. Chem. Soc.* 73 (1) 121–126 (2008) UDC 546.284–31:539.23:621.928.46+542.9+543.4
*JSCS–3693* *Original scientific paper*

# Reactive sputtering deposition of $SiO_2$ thin films

IVAN RADOVIĆ[1], YVES SERRUYS[2], YVES LIMOGE[2] and NATAŠA BIBIĆ[1]*

[1]*Vinča Institute of Nuclear Sciences, P.O. Box 522, 11001 Belgrade, Serbia and* [2]*CEA/Saclay, Section de Recherches de Métallurgie Physique, 91191 Gif sur Yvette Cedex, France*

(Received 17 October 2006)

*Abstract*: $SiO_2$ layers were deposited in a UHV chamber by 1 keV $Ar^+$ ion sputtering from a high purity silicon target, using different values of the oxygen partial pressure ($5\times10^{-6}$–$2\times10^{-4}$ mbar) and of the ion beam current on the target (1.67–6.85 mA). The argon partial pressure during operation of the ion gun was $1\times10^{-3}$ mbar. The substrate temperature was held at 550 °C and the films were deposited to a thickness of 12.5–150 nm, at a rate from 0.0018–0.035 nm $s^{-1}$. Structural characterization of the deposited thin films was performed by Rutherford backscattering spectrometry (RBS analysis). Reactive sputtering was proved to be efficient for the deposition of silica at 550 °C, an oxygen partial pressure of $2\times10^{-4}$ mbar (ion beam current on the target of 5 mA) or, at a lower deposition rate, ion beam current of 1.67 mA and an oxygen partial pressure of $6\times10^{-5}$ mbar. One aspect of these investigations was to study the consumption of oxygen from the gas cylinder, which was found to be lower for higher deposition rates.

*Keywords*: $SiO_2$; thin films; reactive sputtering; RBS analysis.

## INTRODUCTION

Silicon dioxide, in its various crystalline and amorphous phases, is a widely employed material in many technological domains. Two important aspects are currently related to $SiO_2$. It is well known that $SiO_2$ is the most important material in the field of microelectronics. On the other hand, $SiO_2$ is the basic material for the understanding of the behaviour of oxide glasses, used for storage of nuclear waste. Diffusion of components is a critical point in both cases. It was observed, for example, that silicon diffuses in an oxide film during thermal growth of $SiO_2$ on silicon substrates.[1–8] Concerning nuclear glasses, they are exposed to irradiation, which can influence many physical processes, one of the most important being self-diffusion.[9] To develop a new generation of materials (nano-electronics, nuclear glasses), a detailed understanding of the diffusion processes is essential.

* Corresponding author. E-mail: natasabi@vin.bg.ac.yu
doi: 10.2298/JSC0801121R

In order to study diffusion mechanisms and determine a general model for the ageing of nuclear glasses, stoichiometric $SiO_2$ thin films are required. Roma *et al.*[10] reported the first theoretical results for oxygen self-diffusion in $SiO_2$. They considered two distinct modes – the *closed mode*, when no exchange is possible with the atmosphere, and the *open mode*, when exchange with the atmosphere is allowed. To verify their results, special techniques are required to prepare the $SiO_2$ samples. Quantitative measurements of oxygen self-diffusion in $SiO_2$ is feasible in $Si(^{18}O)_2/Si(^{16}O)_2$ bilayer structures using secondary ion mass spectrometry (SIMS), which can clearly distinguish between these two isotopes. In this context, reactive ion beam sputtering offers advantages, such as precise control of the oxygen partial pressure during the deposition process.

The aim of this study was to determine the experimental conditions for $SiO_2$ deposition. The reactive ion beam sputtering technique from a pure Si target was applied for two obvious reasons: (*i*) it provides good control of the deposition parameters and of the layer thickness; and (*ii*) the rf sputtering technique would not be possible for the deposition of $Si(^{18}O)_2$ films, as such targets are not available. All experiments in this study were performed with $(^{16}O)_2$, because the use of $(^{18}O)_2$ would be too costly for these purposes. It was found that stoichiometric $SiO_2$ thin films could be produced by suitable adjustment of the deposition parameters.

## EXPERIMENTAL

The $SiO_2$ layers were deposited by reactive ion beam sputtering in a UHV chamber. A schematic presentation of the installation is shown in Fig. 1. The base pressure in the deposition chamber was $4\times10^{-9}$ mbar. A high purity silicon target (diameter 76 mm), which was bombarded with 1 keV $Ar^+$ ions, at a 45° incidence angle was used. The ion source was an ERIS type ion gun (Electrostatic Reflex Ion Source), irradiating an area of about 1 $cm^2$ of the target. The ion beam current on the target, $I_t$, was varied from 1.67 to 6.85 mA, using a constant argon (purity 99.996 %) partial pressure of $1\times10^{-3}$ mbar. Different values of the oxygen $(^{16}O)_2$ (purity 99.995 %) partial pressure $P_O$, from $5\times10^{-6}$ to $2\times10^{-4}$ mbar, were applied for reactive deposition. Substrates of quasi-monocrystalline graphite (10 mm×10 mm) and silicon (15 mm×8 mm) were employed. Before deposition, the substrates were cleaned by standard chemical procedures. The substrates were placed parallel to the target, at a distance of 150 mm. During the deposition, they were maintained at 550 °C. The $SiO_x$ films were deposited at a rate from 0.0018–0.035 nm $s^{-1}$ to a thickness of 12.5–150 nm.

The thickness of the films was determined by a surface profilometer on the optically flat silicon substrates. Structural characterization of the films was performed by Rutherford backscattering spectrometry (RBS analysis) on quasi-monocrystalline graphite substrates, using a 1 MeV $He^+$ ion beam at normal incidence with the detector at 165° backscattering angle. The experimental spectra were analyzed with the program PERM, version 2003.02.[11,12]

## RESULTS AND DISCUSSION

In a previous work,[13] reactive ion beam sputtering was shown to be efficient for the deposition of silica at 550 °C, using 1 keV $Ar^+$ ions with an oxygen partial pressure $P_O$ of $2\times10^{-4}$ mbar and an ion beam current on the target $I_t$ of 5 mA.

The calculated layer thickness, using the bulk density of $SiO_2$, agreed with a value of 125 nm to that measured with a profilometer. This suggests a reasonable purity of the deposited layer.

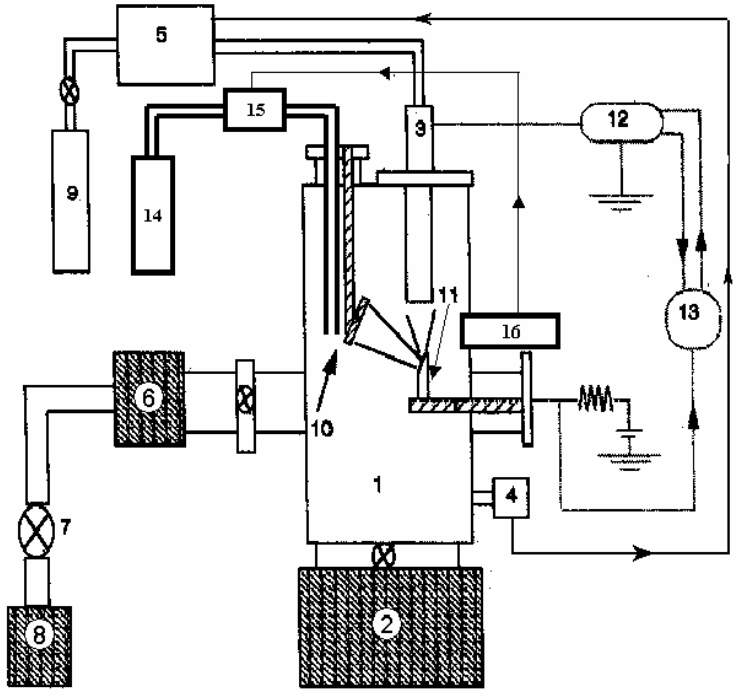


Fig. 1. Schematic presentation of the installation for reactive ion beam sputtering. 1– UHV chamber; 2– ionic pump; 3– ion guns; 4– vacuum gauge; 5– gauge and thermoregulated valve; 6– turbo pump; 7– auxiliary valve; 8– primary pump; 9– argon bottle; 10– sample-holder; 11– target-holder; 12– gun-supply; 13– computer; 14– oxygen bottle; 15– regulation valve; 16– quadrupole gas analyser.

The oxygen consumption during the deposition depended on two parameters for a given thin film thickness: the oxygen partial pressure and the ion beam current on the target. Lowering $P_O$, at a given $I_t$, reduced the gas consumption. Increasing $I_t$, and hence the deposition rate, at a given $P_O$, also reduced the consumption.

One aspect of these investigations was the precise control of the oxygen consumption from the cylinder. In order to reduce the oxygen consumption, a constant $I_t$ of 5 mA at a reduced $P_O$ of $5\times10^{-6}$, $2\times10^{-5}$, $5\times10^{-5}$ and $1\times10^{-4}$ mbar was applied. However, RBS analysis gave an under-stoichiometry of oxygen: $SiO_{0.25}$, $SiO_{0.35}$, $SiO_{0.6}$ and $SiO_{1.25}$, respectively.

Still attempting to reduce the oxygen consumption, an attempt was made to reach the stoichiometry using a higher $I_t$ of 6.85 mA, keeping $P_O$ at $2\times10^{-4}$ mbar, but again an under-stoichiometry resulting in $SiO_{1.85}$ was observed.

The stoichiometry can be attained, under given circumstances, in two ways: increasing $P_O$ and $I_t$ (unrealizable in the present case because at high ion beam currents, the behaviour of the ion gun becomes unstable) and lowering $P_O$ and $I_t$.

The $SiO_2$ stoichiometry of the layers was attained using a $P_O$ of $6\times10^{-5}$ mbar and an $I_t$ of 1.67 mA. RBS Analysis of a sample produced using these parameters is presented in Fig. 2. In Fig. 2a, the experimental spectrum and the fit obtained by introducing Si, O and C in the PERM code can be seen. The extracted depth profiles, Fig. 2b, indicate a very uniform $SiO_2$ stoichiometry of the deposited layer. However, as the applied $Ar^+$ ion beam current on the target was lower, the deposition rate was much lower and, consequently, a layer of small thickness (12.5 nm) was obtained.

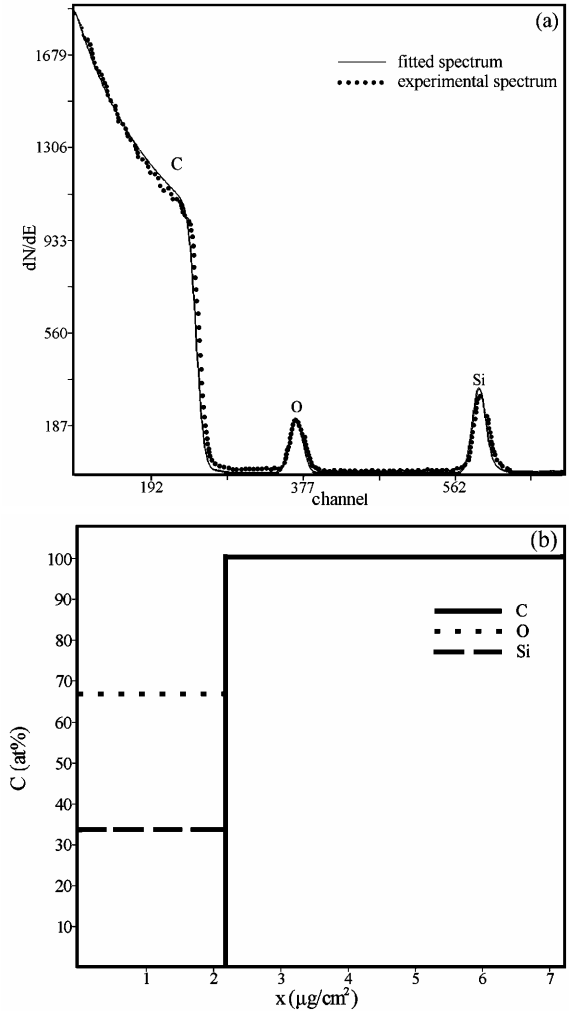


Fig. 2. RBS Analysis of a $SiO_x$/graphite sample deposited at 550 °C, $P_O = 6\times10^{-5}$ mbar and $I_t = 1.67$ mA: (a) experimental and fitted spectra and (b) extracted concentration profiles.

Therefore, stoichiometric $SiO_2$ thin films can be obtained under the conditions: a $P_O$ of $2\times10^{-4}$ mbar with an $I_t$ of 5 mA (deposition rate ≈ 0.029 nm $s^{-1}$), or a $P_O$ of $6\times10^{-5}$ mbar with an $I_t$ of 1.67 mA (deposition rate 0.0018 nm $s^{-1}$). The advantage deposition under the former conditions is a much higher deposition rate, while the stability of the ion beam current is better during deposition under the latter conditions.

To calculate the oxygen consumption in the cases of the high and low deposition rates, the pressure loss in the employed $(^{16}O)_2$ cylinder after one hour of deposition was measured and the maximal thickness of the layers that could be obtained using the total available amount of oxygen was calculated. The results show that, with the available quantity of oxygen, 2100 nm of an $SiO_2$ thin film can be obtained under the conditions: $P_O = 2\times10^{-4}$ mbar and $I_t = 5$ mA, while for $P_O = 6\times10^{-5}$ mbar and $I_t = 1.67$ mA, only 400 nm of $SiO_2$ would be obtain. This infers that working with a higher $I_t$ and a higher $P_O$ results in lower oxygen consumption.

## CONCLUSIONS

It has been shown that the reactive ion beam sputtering technique is efficient for the deposition of silica thin films at 550 °C, using an oxygen partial pressure of $2\times10^{-4}$ mbar and an ion beam current on the target of 5 mA, or at a lower deposition rate, using ion beam current of 1.67 mA and oxygen partial pressure of $6\times10^{-5}$ mbar. The oxygen consumption was calculated to be smaller under a $2\times10^{-4}$ mbar partial pressure. The experimental method enables the oxygen consumption to be controlled precisely during the deposition process. RBS Analysis showed that the obtained $SiO_2$ thin films were stoichiometric.

*Acknowledgments*: This work was supported by the Ministry of Foreign Affairs (in the frame of the COCOP) of the Republic of France, the French Atomic Energy Commission (CEA) and the Ministry of Science of the Republic of Serbia.

## И З В О Д

## ДЕПОНОВАЊЕ ТАНКИХ СЛОЈЕВА $SiO_2$ МЕТОДОМ РЕАКТИВНОГ ЈОНСКОГ РАСПРАШИВАЊА

ИВАН РАДОВИЋ[1], YVES SERRUYS[2], YVES LIMOGE[2] и НАТАША БИБИЋ[1]

[1] *Institut za nuklearne nauke "Vinča", p. pr. 522, 11001 Beograd i* [2]*CEA/Saclay, Section de Recherches de Métallurgie Physique, 91191 Gif sur Yvette Cedex, France*

Танки слојеви $SiO_2$ депоновани су методом реактивног јонског распрашивања, при различитим вредностима парцијалног притиска кисеоника ($5\times10^{-6}$–$2\times10^{-4}$ mbar) и при различитим вредностима струје на мети (1,67–6,85 mA). За распрашивање мете од силицијума коришћен је јонски сноп аргона, енергије 1 keV. Парцијални притисак аргона, при свим депоновањима, износио је $1\times10^{-3}$ mbar. Температура подлоге, при свим депоновањима, износила је 550 °C. Дебљина депонованих слојева кретала се у интервалу од 12,5 до 150 nm, а брзина депоновања у интервалу од 0,0018 до 0,035 nm $s^{-1}$. Структурна карактеризација слојева извршена је спектрометријом Радерфордовог повратног расејања (RBS анализа). Показано је да

се танки слојеви $SiO_2$ могу добити методом реактивног јонског распрашивања при вредности парцијалног притиска кисеоника $2\times10^{-4}$ mbar (струја на мети 5 mA) и $6\times10^{-5}$ mbar (струја на мети 1,67 mA). Један од циљева истраживања био је испитивање потрошње кисеоника при депоновању и нађено је да је она мања при већим брзинама депоновања.

(Примљено 17. октобра 2006)

REFERENCES

1. G. Brébec, R. Seguin, C. Sella, J. Bevenot, J. C. Martin, *Acta Metall.* **28** (1980) 327
2. G. K. Celler, L. E. Trimble, *Appl. Phys. Lett.* **54** (1989) 1427
3. D. Tsoukalas, C. Tsamis, J. Stoemenos, *Appl. Phys. Lett.* **63** (1993) 3167
4. O. Jaoul, F. Béjina, F. Élie, F. Abel, *Phys. Rev. Lett.* **74** (1995) 2038
5. D. Tsoukalas, C. Tsamis, P. Normand, *J. Appl. Phys.* **89** (2001) 7809
6. T. Takahashi, S. Fukatsu, K. M. Itoh, M. Uematsu, A. Fujiwara, H. Kageshima, Y. Takahashi, K. Shiraishi, *J. Appl. Phys.* **93** (2003) 3674
7. D. Mathiot, J. P. Schunck, M. Perego, M. Franciulli, P. Normand, C. Tsamis, D. Tsoukalas, *J. Appl. Phys.* **94** (2003) 2136
8. S. Fukatsu, T. Takahashi, K. M. Itoh, M. Uematsu, A. Fujiwara, H. Kageshima, Y. Takahashi, K. Shiraishi, *Appl. Phys. Lett.* **83** (2003) 3897
9. Y. Serruys, Y. Limoge, G. Brébec, in *Diffusion Processes in Nuclear Materials*, R. P. Agarwala, Ed., Elsevier, Amsterdam, 1992, p. 353
10. G. Roma, Y. Limoge, S. Baroni, *Phys. Rev. Lett.* **86** (2001) 4564, and references therein
11. Y. Serruys, J. Tirira, P. Calmon, *Nucl. Instr. Meth. B* **74** (1993) 565
12. Y. Serruys, *Note technique SRMP 2003-03*, CEA Saclay, 2003
13. I. Radović, Y. Serruys, Y. Limoge, O. Jaoul, N. Bibić, *Proceedings of 22nd SPIG*, Tara, Serbia and Montenegro, 2004, p. 215.

Journal of the Serbian Chemical Society
JSCS@tmf.bg.ac.yu • www.shd.org.yu/JSCS
*J. Serb. Chem. Soc.* 73 (1) 127–129 (2008)
*JSCS–3694*
UDC 547.93:54+542.913.000.57+543+615
*Book review*

BOOK REVIEW

# BILE ACIDS
## Chemistry, biosynthesis, analysis, chemical and metabolic transformations and pharmacology

Editors: M. MIKOV and J. P. FAWCETT

Authors: M. MIKOV, J. P. FAWCETT, K. KUHAJDA, S. KEVREŠAN and J. KANDRAČ

*Published by Mediset Publisher, Geneva, Switzerland, 2007, ISBN 0-12-045783-2*

(Received 22 October 2007)

This book is published on 226 pages with 61 figures, 118 schemes, 10 tables and 689 references. It is divided into the following six chapters: 1. Introduction; 2. Structure and Origin of Bile Acids – An Overview; 3. Biosynthesis of Bile Acids in Mammalian Liver; 4. Isolation and Determination of Bile Acids; 5. Chemical and Metabolic Transformation of Selected Bile Acids; 6. Pharmacology of Bile Acids and Their Derivatives – Absorption Promoters and Therapeutic Agents. Figures, structures, reaction schemes and tables are clearly illustrated throughout the text.

In Chapter 1 (K. Kuhajda, J. Kandrač, S. Kevrešan, M. Mikov and J. P. Fawcett), an overview of the structure and origin of naturally occurring bile acids are given. The most dominant bile acids and their natural sources are summarized with a selection of naturally occurring bile acids with unusual structures, which have mostly been isolated from the bile of reptiles and amphibians.

The biosynthesis of bile acids in mammalian liver and its regulation together with physiological role of bile acids are reviewed in Chapter 2 (S. Kevrešan, K. Kuhajda, J. Kandrač, J. P. Fawcett and M. Mikov). A survey of the steps in the biosynthesis of bile acids from cholesterol in liver cells (hepatocytes) is given. Various mechanisms of the regulation of the biosynthesis of bile acids are presented. In addition to the physiological function of emulsifying lipids in the intestinal tract, the importance of the ability of bile acids to dissolve and transport cholesterol in the bile is emphasized.

In Chapter 3 (J. Kandrač, S. Kevrešan, M. Mikov, J. P. Fawcett and K. Kuhajda) the methods of isolation and determination of bile acids are reviewed. Methods for the separation of bile acids from cattle and pig bile are given in detail.

Isolation of a mixture of cholic and deoxycholic acids, as well as the purification of these acids from cattle bile is described. The isolation and purification of hyodeoxycholic acid and other components of pig bile are also described. Methods for the determination of bile acids in various biological samples are reviewed in several sections concerning enzyme assays, radioimmunoassay, enzyme immunoassay and chromatographic methods. Among the chromatographic methods, the separation and determination of bile acids by thin-layer chromatography, gas chromatography, gas-liquid chromatography and high performance liquid chromatography are reviewed. Particular attention is given to high performance liquid chromatography methods, which have recently been the most often applied methods of the separation and determination of bile acids.

Chapter 4 (K. Kuhajda, S. Kevrešan, J. Kandrač, J. P. Fawcett and M. Mikov) gives a survey of chemical transformations of selected bile acids. The first chemical transformations of bile acids were performed with the aim of determining their structure, and later they were concerned with transformations of particular bile acids to other bile acids, as well as with the syntheses of steroid hormones and some vitamins. To this end, use was mostly made of the reactions of selective acylation, oxidation and reduction of selected bile acids and their derivatives. The papers dealing with the synthesis of potential metabolites in the biosynthesis of bile acids are also herein presented. Steroid hormones, such as pregnenolone, progesterone and testosterone, are synthesized from methyl hyodeoxycholate, and cortisone from methyl deoxycholate. Numerous works and patents devoted to the synthesis of ursodeoxycholic acid from cholic or chenodeoxycholic acid indicate its effectiveness in the treatment of cholelithiasis. Chenodeoxycholic acid appears to be an excellent precursor in the synthesis of a steroid plant growth regulator, as well as in the syntheses of metabolites and vitamin D analogues. Chirality of bile acids can be used in the syntheses of cyclic and acyclic molecular chiral receptors and chiral solvents. Cholic and deoxycholic acids serve in the creation of new macrocyclic structures, which exhibited different capacities in binding and transporting other compounds. Also, one of the trends in the chemistry of bile acids is their application in combinatorial chemistry.

M. Mikov, J. P. Fawcett, K. Kuhajda and S. Kevrešan review the pharmacology of bile acids and their derivatives in Chapter 5. The therapeutic use of bile has been recognized since ancient times. Previously bile acids were the standard treatment for gallstones, chenodeoxycholic acid and ursodeoxycholic acid are effective in causing the dissolution of cholesterol gallstones in humans, but today their therapeutic role looks set to expand enormously. Bile acids as absorption promoters have the potential to aid intestinal, buccal, transdermal, ocular, nasal, rectal and pulmonary absorption of various drugs. Keto derivatives of cholic acid, 3$\alpha$,7$\alpha$-dihydroxy-12-keto-5$\alpha$-cholic acid (sodium salt and methyl ester) are potential modifiers of the blood-brain barrier, and it was found that they pro-

moted quinine uptake, enhanced the analgesic effect of morphine and prolonged the sleeping time induced by pentobarbital. The barriers to the administration of drugs by these routes can be overcome by bile acids at concentrations that are non-toxic. Bile acids as therapeutic agents have the potential to produce beneficial effects in sexually transmitted diseases, primary biliary cirrhosis, primary sclerosing cholangitis, gallstones, digestive tract diseases, cystic fibrosis and cancer.

In conclusion, this is an extremely useful text for anyone involved in bile acids, teaching or research. In my opinion, no better comprehensive treatise of this subject exists. The book may also serve as a good reference source for those contributing to further developments in this field. For those who are looking for a new area of research that can have an impact on the public health, this text offers an excellent place to begin. The editors and their collaborators are to be commended on their efforts in bringing this field to our attention.

Velimir Popsavin*#
Department of Chemistry, Faculty of Science
University of Novi Sad, Serbia

* E-mail: popsavin@ih.ns.ac.yu
# Serbian Chemical Society member.